DISSIPATION OF MAGNETIC FLUCTUATIONS IN THE SOLAR WIND

by

Robert James Leamon

A dissertation submitted to the Faculty of the University of Delaware in partial fulfillment of the requirements for the degree of Doctor of Philosophy in Physics

Fall 1999

DISSIPATION OF MAGNETIC FLUCTUATIONS IN THE SOLAR WIND

by

Robert James Leamon

Approved: _____

Henry R. Glyde, D.Phil.
Chairman of the Department of Physics and Astronomy

Approved: _____

Conrado M. Gempesaw II, Ph.D.
Acting Vice Provost for Academic Programs and Planning

I certify that I have read this dissertation and that in my opinion it meets the academic and professional standard required by the University as a dissertation for the degree of Doctor of Philosophy.

Signed: _____

Norman F. Ness, Ph.D.
Professor in charge of dissertation

I certify that I have read this dissertation and that in my opinion it meets the academic and professional standard required by the University as a dissertation for the degree of Doctor of Philosophy.

Signed: _____

Ronald P. Lepping, Ph.D.
Member of dissertation committee

I certify that I have read this dissertation and that in my opinion it meets the academic and professional standard required by the University as a dissertation for the degree of Doctor of Philosophy.

Signed: _____

James MacDonald, Ph.D.
Member of dissertation committee

I certify that I have read this dissertation and that in my opinion it meets the academic and professional standard required by the University as a dissertation for the degree of Doctor of Philosophy.

Signed: _____

Charles W. Smith, Ph.D.
Member of dissertation committee

I certify that I have read this dissertation and that in my opinion it meets the academic and professional standard required by the University as a dissertation for the degree of Doctor of Philosophy.

Signed: _____

Gary P. Zank, Ph.D.
Member of dissertation committee

EPIGRAPH

Guide me, O Thou great Jehovah,
Pilgrim through this barren land;
I am weak, but Thou art mighty,
Hold me with thy powerful hand.
Bread of Heaven, bread of Heaven,
Feed me till I want no more.

— William Williams (Pantycelyn) 1717–91

ACKNOWLEDGMENTS

Deepest thanks go to Dr. Ness, who was more approachable and avuncular than I would have ever imagined an advisor to be.

Many thanks also to the rest of my committee: Drs. Ron Lepping, Jim MacDonald, Gary Zank and in particular Chuck Smith, who in many ways was a *de facto* second advisor. Ron Lepping is also due thanks for providing the WIND magnetic field data used extensively in this work. Other scientific gratitude is due to Bill Matthaeus, Kit Wong; and to Keith Ogilvie and Dick Fitzenreiter who provided the WIND proton and electron plasma data.

In as much as this Ph.D. dissertation is the culmination of all my years of education, I should also give thanks to my parents, Jean & Geoff, for starting me off on the right foot, and to the school teachers, university researchers and lecturers who guided, encouraged and inspired me: Tanya Dempster, Arwyn Harries, David Williams, Margaret Cainen and the late Glan Harries at Bishopston; Pat Stevens and Huw Thomas at Olchfa; Michéle Dougherty, Vivien Moore, Gareth Jones and David Southwood at Imperial; and Renée Prangé at l'Institut d'Astrophysique Spatiale.

To the many friends have supported me socially (and on occasion, literally) through my academic career, you are also due a huge debt of gratitude (and refreshment, if you so choose). This list is by no means exhaustive: Simon Gibbons, Sarah Lee, Sarah Goodchild, Sarah Welsh, Danièle Steer, Will Stallard, Pete Charters, Flemming Heinø, Martin Heighway, Jim Caron, Eric & Michelle Mas, Dave McKenzie, Greg Avicola, Dan Guerin, Rich Piccola, and Hugh & Lynn Kenney.

And finally to Hillary 'OE' Hertler, whom I love.

TABLE OF CONTENTS

LIST OF FIGURES

LIST OF TABLES

ABSTRACT

The dissipation range for interplanetary magnetic field fluctuations is formed by those fluctuations with spatial scales comparable to the gyroradius of a thermal ion. The dissipation range represents the final fate of magnetic energy that is transferred from the largest spatial scales via nonlinear processes until resonance with the thermal ions removes the energy from the spectrum and heats the background distribution. Typically, the dissipation range at 1 AU sets in at spacecraft frame frequencies of a few tenths of a Hertz. It is characterized by a steepening of the power spectrum and often demonstrates a bias of the polarization or magnetic helicity spectrum. We examine WIND observations of inertial and dissipation range spectra in an attempt to better understand the processes that form the dissipation range and how these processes depend on the ambient solar wind parameters (*e.g.*, IMF intensity, ambient proton density and temperature, etc.). Despite the commonly held belief that parallel-propagating waves such as Alfvén waves form the bulk of inertial range fluctuations, we argue that such waves are inconsistent with spectral break location data. Instead, we show that kinetic Alfvén waves propagating at large angles to the background magnetic field are consistent with the observations, and we describe some possible motivations for this solution. We also show that MHD turbulence consisting of a slab/2-D composite geometry is consistent with the observations and may form the dissipation range, thereby being responsible for heating the background ions. Lastly, we demonstrate that heating of the background electrons is a likely, or possibly necessary, byproduct of magnetic dissipation.

RÉSUMÉ FRANÇAIS

Bien que l'anglais soit la langue du monde scientifique, je pense qu'une thèse de doctorat représente un sommaire de tout ce que l'on a appris au cours de sa vie scolaire. Il me faut donc inclure ce résumé en français, pour montrer que l'année que j'ai passée au sein de l'Institut d'Astrophysique Spatiale à l'Université de Paris-XI compte toujours beaucoup pour moi. Je tiens remercier encore, donc, Renée Prangé, ainsi que Lysette Hall et Bruno Thibault pour leurs cours de français suivis dans le Delaware.

Le vent solaire constitue la couche supérieure de l'atmosphère du soleil. Le champ magnétique interplanétaire qui s'y infiltre peut nous fournir des informations sur le gaz très ténu qui souffle à $\sim$ 400 km s^{-1}, du soleil vers la Terre. Cette thèse traite des fluctuations aux échelles les plus petites du champ magnétique interplanétaire, et de leur atténuation et dissipation.

La gamme spectrale de dissipation est constituée par des fluctuations d'échelle comparables au rayon de gyration d'un ion thermique. Par l'intermédiaire des processus nonlinéaires, l'énergie magnétique y est transférée des échelles plus grandes jusqu'à ce que la résonnance avec les ions thermiques de fond amortisse l'énergie du spectre en les chauffant. Typiquement, à 1 UA, le début de la gamme de dissipation se situe aux fréquences de quelques dixièmes de Hertz dans le repère de la sonde. Elle est caractérisée par une augmentation du spectre de puissance, et montre souvent une polarisation du spectre d'hélicité magnétique. Nous examinerons dans cette thèse les observations de la sonde WIND dans les intervalles inertiel et

dissipatif pour mieux comprendre les processus qui les forment, et comment ces processus dépendent des paramètres ambiants du vent solaire (par exemple, l'intensité du champ magnétique, la densité ou la température des ions).

Nous montrerons aussi que les ondes parallèles au champ magnétique, comme celles d'Alfvén que beaucoup croient former l'intervalle spectrale inertiel, ne sont pas en accord avec les données. Au contraire, nous mouverons que les ondes cinétiques d'Alfvén, se propageant aux grands angles par rapport au champ magnétique ambiant sont bien en accord avec les données. De plus, nous présenterons quelques arguments possibles en faveur de cette solution. Une géometrie composite, comprenant d'une part des ondes parallèles, et d'autre part une turbulence magnétohydrodynamique perpendiculaire au champ magnétique ambiant est peut-être assez compatible avec les observations aussi, et peut former la gamme de dissipation, donc être responsable du chauffage des ions de fond. Finalement, nous verrons que le chauffage des *électrons* de fond est un résultat probable, ou bien nécessaire, de la dissipation des fluctuations magnétiques.

Chapter 1

INTRODUCTION

1.1 The Solar Wind

Our awareness of a direct connection between the sun and the Earth dates back to *Carrington* [1859], who, when at Greenwich Observatory, noticed a white-light flare on the sun that was followed approximately one day later by an intense magnetic storm. He offered no mechanism to explain his observation. From observations of further flares, the link between solar flares and geomagnetic storms was firmly established by the early years of the twentieth century. As early as a century before, researchers had postulated links between the sun and terrestrial activity, most notably *Canton* [1759], who pointed out that in the northern hemisphere, quiet-day geomagnetic fluctuations are stronger in summer than in winter, when that hemisphere is closer to the sun, and *de Mairan* [1754], who thought that aurorae were caused by the entry of solar particles into the upper atmosphere. His (profound) reasoning was that zodiacal light was light scattered from the outer layers of the sun's atmosphere and, therefore, the Earth orbits within them. A fuller and very interesting account of the development of Space Physics before the Space Age may be found in *Parker* [1999].

Biermann [1951] showed that photon radiation pressure alone was unable to explain the "windsock" effect, whereby cometary ion tails point radially away from the sun; from this he inferred a continuous corpuscular outflow from the corona, in all directions, and at all times during the solar activity cycle.

The nature of the outflow from the corona was debated for much of the 1950s: *Parker* [1958] postulated the existence of a supersonic ion flow which he called the "solar wind;" *Chamberlain* [1960, 1961] believed that Parker had chosen the wrong solution of his own equations, and that the correct solution was a subsonic "solar breeze." Initial Russian *in situ* measurements [*e.g.*, *Gringauz et al.*, 1960] were inconclusive, and it was not until the first American measurements of plasma density and velocity by the Explorer X spacecraft [*Bridge et al.*, 1961; *Bonetti et al.*, 1963] that the argument was decided in Parker's favor. Explorer X sampled the solar wind in brief segments as the Earth's magnetopause 'flapped' over it. The Mariner 2 mission to Venus [*Snyder and Neugebauer*, 1964; *Mackin and Neubegauer*, 1966] provided the first extended sampling and study of the solar wind.

We may view the solar wind as the outer part of the solar corona: Gravitational (and magnetic) forces are unable to contain the $> 10^6$ K solar corona, which then "boils off" and streams out in all directions. The ensuing flow, initially driven by the pressure gradient between the corona and the inner part of the solar system, expands supersonically to fill a region of space known as the *heliosphere*. Outside the heliosphere is the Local Interstellar Medium (LISM). The nature of pressure changes over the boundary. Inside the boundary it is dominated by the 'ram' pressure ρV^2 of the solar wind, and outside the internal (magnetic and thermal) pressure of the LISM, which are $\simeq$ 300 times the LISM ram pressure dominates. No spacecraft has yet encountered the edge of the heliosphere, and current estimates of its closest point to the sun range from 80–150 AU [*Zank*, 1999]. (At their current speeds, then, we may expect Voyagers 1 and 2 to leave the heliosphere in 5–20 years.)

1.1.1 Solar Wind at Near-Earth Orbit

The solar wind at near-Earth (1 AU, low heliographic latitude) is highly variable, ranging from a low flow speed of ~ 250 km s^{-1} to a high of ~ 850 km s^{-1}. Embedded within the conducting plasma is a "frozen-in" [*Taylor*, 1938] portion of

the solar magnetic field. *Parker* [1958] pointed out that the combination of solar rotation and a (nearly) radial solar wind expansion would cause the interplanetary magnetic field (IMF) lines to be stretched out into Archimedean spirals:

$$\frac{r}{b} - 1 - \ln\left(\frac{r}{b}\right) = \frac{v}{b\omega}(\phi - \phi_0), \tag{1.1}$$

where b represents the radius ("Alfvén critical radius") at which both solar gravitation and outward acceleration by high coronal temperature may be neglected, and as such may be viewed as a boundary between the corona and the solar wind (current estimates [*Lotova*, 1988] place b in the range 5–20$R_\odot$); v is the outward flow velocity; $\omega = 2.7 \times 10^{-6}$ rad s^{-1} is the angular rate of rotation of the sun; and ϕ_0 is the azimuth of the field line at $r = b$. Figure 1.1 shows this spiral geometry for a constant solar wind speed of 400 km s^{-1}. The field lines become more tightly wound at greater heliocentric distances. Parker's theory further predicts, from $\boldsymbol{\nabla} \cdot \mathbf{B} = 0$, that the magnetic field at the point (r, θ, ϕ) is given by

$$\begin{aligned} B_r(r,\theta,\phi) &= B_0(\theta,\phi_0)\left(\frac{b}{r}\right)^2, \\ B_\theta &= 0, \\ B_\phi &= B_0(\theta,\phi_0)\frac{\omega}{v}(r-b)\left(\frac{b}{r}\right)^2 \sin\theta. \end{aligned} \tag{1.2}$$

It then follows, if r is expressed in units of $R_\odot$ or AU, that the radial fall-off the magnitude of the magnetic field is $B \propto (r^{-4} + r^{-2})^{1/2}$.

At the orbit of the Earth, the corotation speed $r\omega = 405$ km s^{-1}, so that the average radial and longitudinal components of the magnetic field are nearly equal. The angle between the field and a line drawn from the sun to an observer at 1 AU should be close to 45°, as is observed for long-time averages of the IMF [*Smith and Bieber*, 1991].

A variety of transient and source effects can lead to variability of the solar wind parameters at 1 AU. However, following the review by *Barnes* [1979], we show in Table 1.1 a description of typical solar wind conditions in near-Earth orbit.

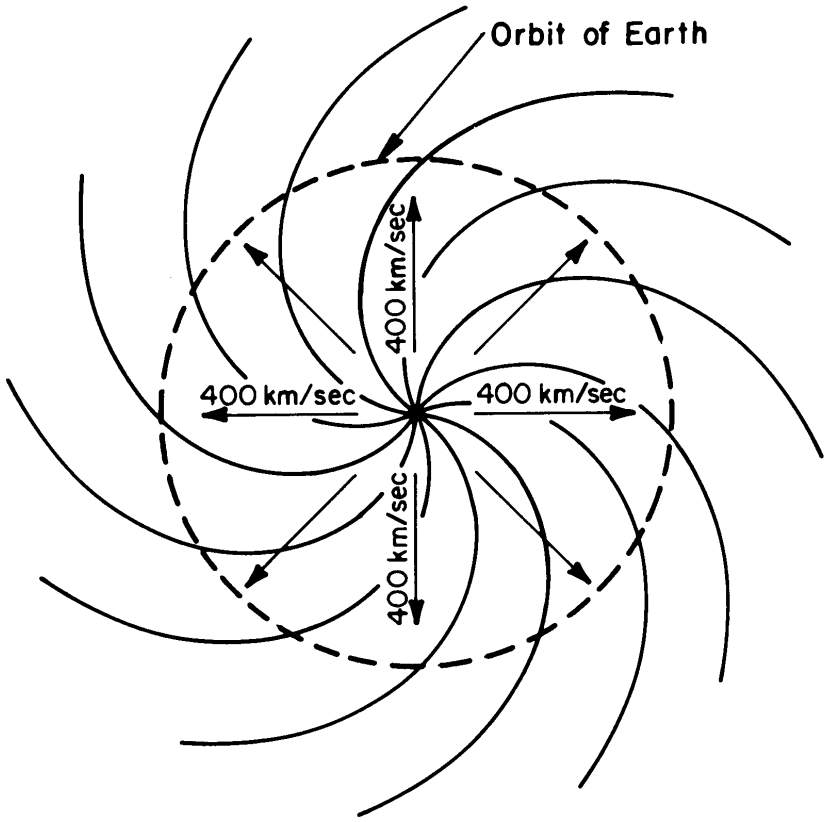

Figure 1.1: Spiral interplanetary magnetic field lines frozen into a radial solar wind expansion at 400 km s^{-1}. Adapted from *Parker* [1963].

Table 1.1: Observed properties of the interplanetary medium in the ecliptic plane

Measured Parameter	Typical value in the ecliptic at 1 AU	Typical value in high-speed streams	Variation with heliocentric radius r
Flow velocity V_{SW}, km s^{-1}	400	750	constant
Proton number density n, cm^{-3}	6	4	$\propto r^{-2}$
Magnetic Field Strength B, nT	5–8	5–8	radial $\propto r^{-2}$ azimuthal $\propto r^{-1}$
Proton temperature T_p, K	$\sim$4–10 $\times 10^4$	$\sim 2 \times 10^5$	$\propto r^{-a}$, $2/7 \lesssim a \leq 4/3$
Electron temperature T_e, K	$\sim$1–2 $\times 10^5$	$\sim 2 \times 10^5$	$\propto r^{-b}$, $2/7 < b \leq 4/3$

The values of the parameters listed in Table 1.1 are only averages; these quantities fluctuate over every measured spatial and temporal scale.

Based on the fundamental quantities shown in Table 1.1, we may derive a number of additional quantities that will prove useful in characterizing the ambient solar wind plasma and/or its effects on the waves and turbulence that we consider in this work. These derived quantities are shown in Table 1.2, where e is the magnitude of the charge of the electron and proton, k_B is Bolzmann's constant and μ_0 is the permeability of free space.[1]

The plasma β (either electron, proton or their sum, the total β) is an extremely useful quantity, and can be viewed as a portmanteau variable covering the

[1] As need arises, we shall use cgs-Gaussian units instead of SI in this dissertation, whereby μ_0 is replaced by 4π and the formula for gyrofrequency becomes eB/m_pc. We do this for numerical comparison with previous works in this field and because SI gives a less symmetric, and arguable less clear, notation for some of the plasma equations of motion and Maxwell's equations. See, *e.g.*, Appendix A of *Jackson* [1975] for a discussion of the differences between the two systems.

Table 1.2: Useful derived quantities, and their characteristic values in the ecliptic plane at 1 AU.

Derived Quantity	Formula	Typical value at 1 AU
Proton plasma β	$\beta_p = 2\mu_0 n_p k_B T_p / B^2$	~ 1
Electron plasma β	$\beta_e = 2\mu_0 n_e k_B T_e / B^2$	$\sim$ 1–1.5
Ion gyrofrequency	$\Omega_p = eB/m_p$	$\sim$ 0.1 Hz
Thermal speed	$v_{th} = (k_B T_p / m_p)^{1/2}$	$\sim$ 50 km s^{-1}
Alfvén speed	$V_A = B/\sqrt{\mu_0 \rho}$	$\sim$ 50 km s^{-1}
Larmor radius	$R_L = v_{th}/\Omega_p$	50–100 km
Ion inertial length	$\rho_i = V_A/\Omega_p$	50–100 km

variability of the three quantities used in its definition: density, temperature and field strength. The reader may recognize it as the ratio of plasma pressure to magnetic pressure, or equivalently as the ratio $2v_{th}^2/V_A^2$.

1.1.2 Solar Wind at High Latitudes

Although not addressed in detail here, it is worth noting that the high wind speed observations from near-Earth orbit are a manifestation of high-latitude solar sources. Ulysses measurements [*Phillips et al.*, 1995] show a much hotter, faster solar wind at high latitudes, along with strong correlation between fluctuations in the magnetic and velocity fields.

Foukal [1990] offers the following simple explanation for the $\gtrsim$ 800 km s^{-1} flow: In coronal holes the magnetic field lines diverge much more rapidly than radial expansion over the first few solar radii. Eliminating density from the equation for solar wind expansion gives

$$\left(v - \frac{v_s^2}{v}\right)\frac{dv}{dr} = \frac{v_s^2}{A}\frac{dA}{dr} - \frac{dv_s^2}{dr} - \frac{GM_\odot}{r^2}, \tag{1.3}$$

where A is the cross-sectional area of wind flow and $v_s = (P/\rho)^{1/2}$ is the isothermal sound speed. From equation (1.3), we see that plasma acceleration dv/dr is determined in part by the outward increase in A of wind flow as well as by the gradient of

sound speed (and thus temperature) and by the retarding gravitational force. Acceleration is increased as A grows more rapidly with r, so the diverging magnetic field line geometry of coronal holes should tend to accelerate the wind more rapidly than a spherically symmetric expansion. There are some problems with the explanation outlined above, most notably that increased thermal conduction "bleeds away" heat that would otherwise be available for conversion to the kinetic energy of the flow. Much research is currently being done to fully explain the acceleration of polar solar wind.

Modern models of the solar wind source region describe both the high latitude wind source emanating from the polar holes and multiple low-latitude sources (the "streamer belt"). Observations at near-Earth orbit include wind sources from both regions in a highly variable and dynamic interaction of high-speed wind overtaking low-speed wind, creating shocks [*Kennel et al.*, 1985; *Richter et al.*, 1985, see section 1.1.4] and wind shear, large vortices, rarefaction regions, and a host of complex interaction regions, which evolve dynamically with distance and latitude. These interactions are sources of fluctuation energy at the same time as they process the plasma, according to a variety of linear and non-linear dynamics.

1.1.3 Sector Structure

The solar photosphere was first shown to be the source of the interplanetary magnetic field by *Ness and Wilcox* [*Wilcox and Ness*, 1965; *Ness and Wilcox*, 1965], using the IMP 1 spacecraft. They demonstrated that the IMF has the same 27-day rotation rate as the sun in a Sun-Earth system, and they also delineated the sector structure of the field. On average, the sector structure of the IMF is a quasi-stationary pattern of alternating regions of dominant field polarity, either towards or away from the sun along the spiral direction.

The IMF sector polarity can be deduced from polar geomagnetic observations; the geomagnetospheric field line configuration is dependent on the (sign of

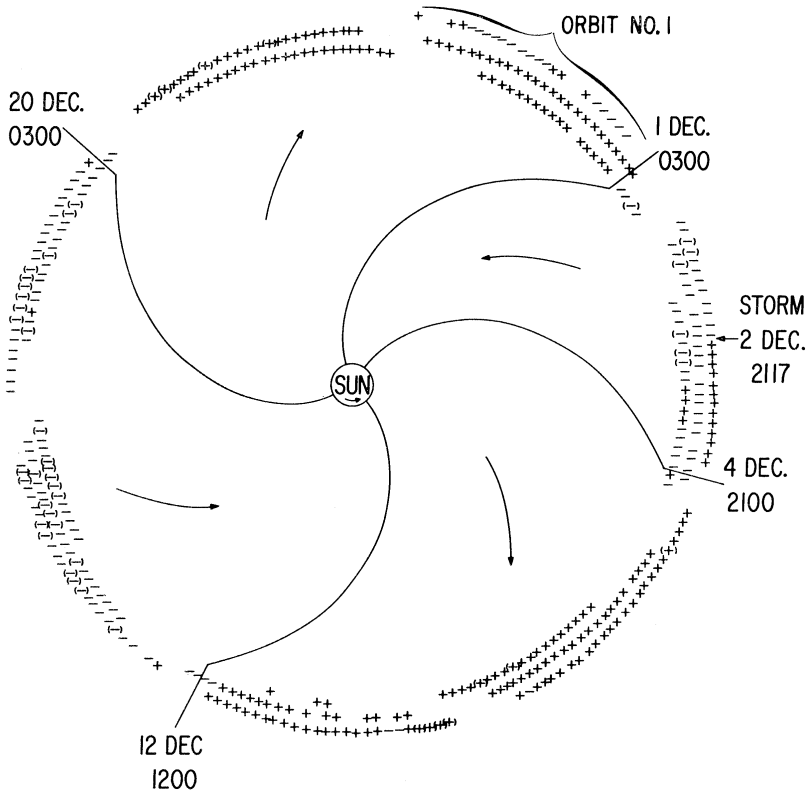

Figure 1.2: Sector structure of the IMF. Reproduced from *Wilcox and Ness* [1965].

the) azimuthal component of the IMF field. Using this technique, *Svalgaard* [1972] inferred the sector polarity all the way back to 1926 and suggested that the sector pattern was broadly the same through each solar sunspot cycle. A two-sector pattern is characteristic of solar maximum, whereas a four-sector pattern is highly likely during solar minimum and is more common during most of the solar cycle. Figure 1.2 shows typical sector boundaries from near solar minimum in December 1963.

Although not the principal thrust of this dissertation, the IMF sector structure has been discussed for two reasons. Firstly, the analysis described later must avoid the IMF reversals associated with the passage of a sector boundary because it leads to non-representative IMF spectra. Second, the IMF sector structure determines why some intervals of interest possess a mean IMF direction directed away

from the sun, while others have the field directed towards the sun. This bipolar feature of the mean field will aid in determining the plasma modes associated with the dissipation process.

When sector reversals are combined with high solar wind speeds, a spacecraft in near-Earth orbit gains the ability of sampling, comparing and contrasting the two opposing high-latitude source regions.

1.1.4 Shocks

The existence of interplanetary shock waves originating at from the sun was suggested on the basis of the abrupt onset of geomagnetic disturbances [*Gold*, 1955], even before their direct observation. This was despite the objection that the material in interplanetary space must be so tenuous that ordinary Coulomb collision lengths were 'astronomically' large. Shock waves *can* form in a magnetized plasma with a thickness much smaller than the collisional mean free path of the plasma; hence the terminology "collisionless shocks." By the solar wind, the typical collisional mean free path, as calculated from kinetic theory, is about 1 AU. In contrast, the Earth's bow shock and interplanetary shocks have thicknesses of the order of 1000 km.

Shocks occur when: (*i*) the supersonic and super-Alfvénic solar wind interacts with the magnetic field of a planet; (*ii*) it encounters so many pickup ions that mass loading requires the flow to become sub-Alfvénic (this happens upstream of comets); (*iii*) when a fast stream overtakes a slow stream within the solar wind; and (*iv*) when eruptions on the sun such as flares and coronal mass ejections forcibly expel material into space. The first two possibilities will not be mentioned further in this dissertation. A shock front moving outward through the solar wind overtakes the slower-moving plasma ahead of it, heating (by compressing) what it sweeps up. The shock transfers momentum and energy to an expanding region of solar wind plasma. Unless momentum and energy are continually replenished, *i.e.*, if the shock is driven, it must decelerate as it expands into the ambient solar wind.

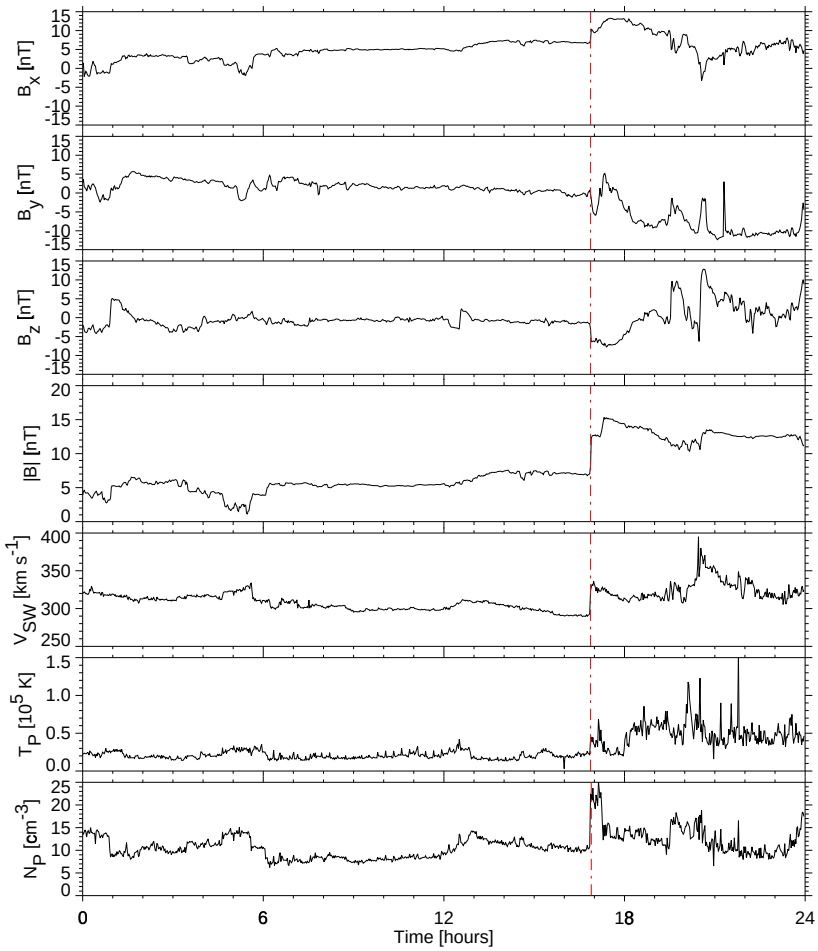

Figure 1.3: Interplanetary shock observed by WIND at 1652 UT on April 7, 1998.

An interplanetary observer (or spacecraft) detects the passage of a shock wave by an abrupt decrease in the plasma speed, and abrupt enhancements in the density, temperature and magnetic field (in both magnitude and direction). An example of such an interplanetary shock can be seen in Figure 1.3.

The enhanced dissipation and heating associated with a shock was an early motivation for the work described here. Before addressing the very interesting questions of shock wave dissipation, it was recognized that related questions for the undisturbed quiescent solar wind plasma were incompletely resolved. Nevertheless, in so far as shocks represent regions of strong, localized dissipation in association with compression, they remain an interesting subject of study with added degrees of complexity beyond those discussed here.

1.1.5 Coronal Mass Ejections and Magnetic Clouds

Coronal mass ejections (CMEs) are an almost daily occurrence on the sun. A large mass (10^{12}–10^{13} kg, or about 1% of the daily mass-loss rate of the quiet solar wind) of coronal, and sometimes prominence material that was previously contained by magnetic field lines is suddenly and violently expelled into interplanetary space.

The ejecta detected by an orbiting spacecraft is referred to as an Interplanetary Manifestation of a CME, or ICME for short. The ICME is almost always preceded by a shock, is often followed by a reverse shock located behind a high speed stream, and often has a very distinct magnetic structure. The primary diagnostic of an ICME is an extended period of bi-directional electron heat flux, indicative of magnetic connection to the solar corona on both sides of the spacecraft.

Burlaga et al. [1981] described this magnetic structure as a "Magnetic Cloud." According to Burlaga's definition, there are three required properties for a magnetic structure to be identified as a magnetic cloud: (*i*) a very low proton temperature; (*ii*) a large smooth rotation of the field direction; and (*iii*) enhanced magnetic field

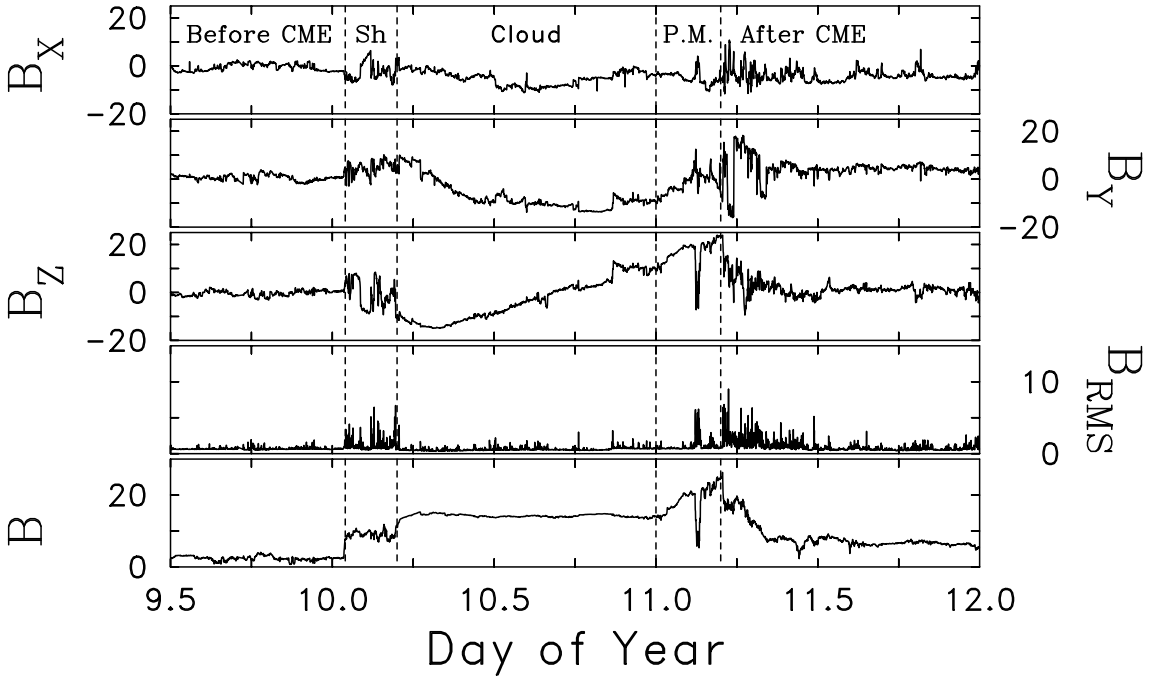

Figure 1.4: Time series for magnetic field components (B_X, B_Y, B_Z) in nanotesla (nT) and GSE coordinates at 92 s resolution plus magnitude of field and RMS value of fluctuations. Approximate times of non-CME observations, sheath (Sh), cloud, and prominence material (P.M.) as determined by *Burlaga et al.* [1998] are noted in the figure.

strength. Clouds are also large: they may take $\frac{1}{2}$ to $1\frac{1}{2}$ days to pass by a spacecraft at 1 AU. They frequently exhibit greatly reduced fluctuation levels as well.

Figure 1.4 is an example of a magnetic cloud embedded within an ICME, taken from WIND data in January 1997. At this time, WIND was some 100–115R_E upstream of Earth, and slightly below the ecliptic plane. The remarkably constant enhanced field strength (14 nT) and smooth rotation are clearly visible. We study this particular magnetic cloud in sections 2.1.1 and 3.6.

1.1.6 Solar Cycle Variability

The character of the solar wind changes on an 11-year solar cycle. We have already discussed the sector structure, which can vary from 4 sectors at solar minimum to 2 sectors at solar maximum. As the solar cycle descends to its minimum, an increasing amount of high speed solar wind emanating from the coronal holes is observed at 1 AU. This is the result of the polar coronal holes expanding to lower and lower solar latitudes as the solar cycle approaches minimum.

The photospheric magnetic field becomes increasingly looped, twisted and generally more complicated as the cycle approaches maximum. As a result, the number of flares, prominences and ejecta increase. The solar magnetic field, and therefore, its extrusion into interplanetary space, also increases in magnitude with the approaching solar maximum. This is, perhaps, not surprising given the increasing number of sunspots and the intense magnetic fields associated with them.

1.2 Fluctuations

Two paradigms are currently in vogue for describing the basic nature of low-frequency (from $< 10^{-4}$ to ~ 1 Hz in the spacecraft frame) IMF fluctuations. In the first paradigm, IMF fluctuations are thought to consist mostly of waves described by the magnetohydrodynamic (MHD) equations (see *Coleman* [1966] and review by *Barnes* [1979]). The standard argument holds that these waves originate at the Sun near the Alfvén critical point, propagate outward, and are largely unaffected along their propagation path except for WKB transport effects [see *Hollweg*, 1990]. The near-Sun source is supported in part by observations near 1 AU of correlations between the magnetic and fluid velocity fluctuations that suggest a predominantly outward propagation of the wave [*Belcher and Davis*, 1971].

Propagation of the waves at small angles to the ambient mean magnetic field is commonly assumed on the basis of the observation of minimum variance directions

which tend to be aligned with the mean field near 1 AU [*Belcher and Davis*, 1971; *Daily*, 1973].

Apart from the high IMF-fluid velocity correlations (high cross helicity[2]) several other observations and theoretical considerations support and refine the wave paradigm. The damping of slow mode waves generally and of the fast mode wave due to nonlinear steepening and Landau damping [*Barnes*, 1979] at nonzero angles of propagation relative to the mean magnetic field suggest that the parallel-propagating Alfvén mode should be dominant in the solar wind, since it is the only wave mode without a significant first-order damping mechanism for wavenumbers far below the ion cyclotron scale. Such waves, with limited nonlinear interactions, may be a relict of solar atmospheric fluctuations if the wave paradigm is correct. The test of this paradigm is whether the fluctuations evolve radially in a manner consistent with non-interacting waves (some studies suggest they do not—as we shall see in section 1.2.2).

In the second paradigm, the turbulence paradigm, it is argued that the IMF fluctuations are fundamentally nonlinear and interactive so that self-organization of fluctuations over a broad range of frequencies is achieved [*Coleman*, 1968; *Matthaeus and Goldstein*, 1982a]. In this model, fluctuation energy that originates at or near the sun may propagate or convect outward, but added energy due to large-scale, *in situ* processes and dissipation may be important [*Goldstein et al.*, 1995; *Tu and Marsch*, 1995]. The magnetic energy is transferred through the spectrum to spatial scales that might otherwise be depleted so that a self-deterministic spectrum is achieved. As we shall see below, in this paradigm the IMF fluctuations in the range from $< 10^{-4}$ to ~ 1 Hz form the "inertial range" of the spectrum, and at higher frequencies heating is implied [*Coleman*, 1968].

---

[2] Defined and discussed more fully in section 2.3, but for now it may be considered a measure of what fraction of the fluctuations are moving inwards or outwards.

1.2.1 WKB Theory

WKB theory, named for its inventors *Wentzel* [1926], *Kremers* [1926] and *Brillouin* [1926], is a tool of Quantum Mechanics, developed to calculate approximate solutions of the Schrödinger equation. *Jeffreys* [1923] developed the method independently for the more general study of wave equations, and some researchers refer to the theory as 'WKBJ.'

In Quantum Mechanics it is a 2-timescale approximation where the solution at any time is the unperturbed normal mode that is then allowed to evolve on a longer timescale. In its usual version in the discussion of MHD waves, the theory assumes that the waves are monochromatic with angular frequency ω, are of small amplitude, and propagate in a stationary background. The quantum analogy comes from the fact that $\omega(\mathbf{k}, \mathbf{x})$ is a constant of the motion; the waves may be viewed as quanta of energy ω and momentum $\mathbf{k}$.

A fluctuating quantity (*e.g.*, the fluctuating part $\delta\mathbf{B}$ of the magnetic field) is taken to be of the form:

$$\delta\mathbf{B}(\mathbf{x}, t) = [\delta\mathbf{B}_1(\mathbf{x}) + \delta\mathbf{B}_2(\mathbf{x}) + \ldots] \exp[iS(\mathbf{x}) - i\omega t]. \tag{1.4}$$

The dynamical equations are then linearized in the fluctuating variables. The phase $S(\mathbf{x})$ is assumed to vary on a length scale λ that is short compared to the scale L of large-scale fluctuations in the unperturbed background: $\mathbf{k}(\mathbf{x}) = \boldsymbol{\nabla} S$ is assumed to vary only on the long scale L, and $|\delta\mathbf{B}_2|/|\delta\mathbf{B}_1| \sim \lambda/L \ll 1$. The independent variables and the dynamical equations are expanded in powers of λ/L. The resulting equations (in first order) are only self-consistent if $\mathbf{k}(\mathbf{x})$ and ω are related by the usual dispersion relation, *i.e.*, if the dispersion relation

$$\det \mathbf{D}(\mathbf{k}, \omega) = 0 \tag{1.5}$$

derived from the theory of waves in a spatially homogeneous background is locally satisfied. Equation (1.5) is a first-order partial differential equation for S and may

either be solved by the method of characteristics or by Hamilton-Jacobi theory, whence the quantum mechanical approach and nomenclature.

1.2.2 Evolution of Fluctuations

The test of any theory is whether its predictions are consistent with observations. The basic assumptions of WKB theory (no reflected waves and no dissipation) are invariably violated [*Hollweg*, 1974]. (Indeed, this dissertation is about the dissipation of IMF fluctuations.) However, assuming that the density decreases as r^{-2} in the heliosphere,[3] WKB theory predicts that the magnetic fluctuation power should decrease as r^{-3}, a result that has been confirmed by many studies [*e.g.*, *Belcher and Burchsted*, 1974; *Roberts et al.*, 1990] covering radial distances from 0.7 to 8 AU.

More recently, [*Zank et al.*, 1996, see their Figure 4] extended the radial scale for fluctuation power to 40 AU, using Voyager 1, Voyager 2, and Pioneer 11 data, finding that "there is a remarkably consistent power law trend out to 40 AU." While the WKB prediction follows the data well at heliocentric distances less than 6–10 AU, there is an excess of fluctuation power (the power law decays more slowly than predicted by WKB theory) further out in the heliosphere. *Zank et al.* [1996] then derive an evolution equation for the fluctuation power, and find turbulent dissipative solutions driven by stream interactions and pickup ions that provides a better fit to the data than the evolution of WKB waves. *Matthaeus et al.* [1999b] expand on this model to include the radial temperature profile—see Figure 1.6 and section 1.4 below.

---

[3] The continuity (mass conservation) equation is $\partial\rho/\partial t + \boldsymbol{\nabla}\cdot(\rho\mathbf{V}_{SW}) = 0$. For time-steady flow, the divergence term, in spherical polar coordinates, becomes

$$\frac{1}{r^2}\frac{d}{dr}\left(r^2\rho V_{SW}\right) = 0$$

from which the r^{-2} dependence follows immediately.

WKB theory also predicts that the solar-originating fluctuations refract in a spherically expanding solar wind,[4] so that their wave vectors **k** are almost radial at 1 AU, whereas observations [*Belcher and Davis*, 1971] give the minimum variance direction aligned with the mean magnetic field.

Roberts et al. [1987a, b] studied the evolution of cross helicity using data from Helios and the Voyagers. Their results were mixed for the wave paradigm. Close to the sun, the cross helicity is high, indicating a predominance of outward-propagating waves, but there is a definite evolution towards a less purely Alfvénic state and by $\sim$ 10 AU, the mean cross helicity is zero, indicating as many inward-propagating waves as outward-propagating ones. Since inward-propagating waves generated below the Alfvén critical point cannot propagate past it, not all observed fluctuations can be generated in the solar atmosphere. Furthermore, the Alfvén ratio, the ratio of kinetic to magnetic energy of the fluctuations, is also found to decrease in the outer heliosphere, in disagreement with WKB theory [*Roberts et al.*, 1990], which predicts equipartition at all distances.

1.3 IMF Spectra

A superior technique for separating spatial or temporal scales in IMF time series is the spectral decomposition and cross-correlation of those time series.

Three methods of computing the power spectrum were used in the analysis of data presented here: the fast Fourier transform (FFT), the *Blackman and Tukey* [1958] algorithm based on transforming the correlation function of the data, and a similar method based on transforming the structure function of the data [*Smith et al.*, 1990b]. Appendix A discusses these methods and their manner of computation in more detail.

[4] This is essentially a geometric effect due to the expansion of the solar wind.

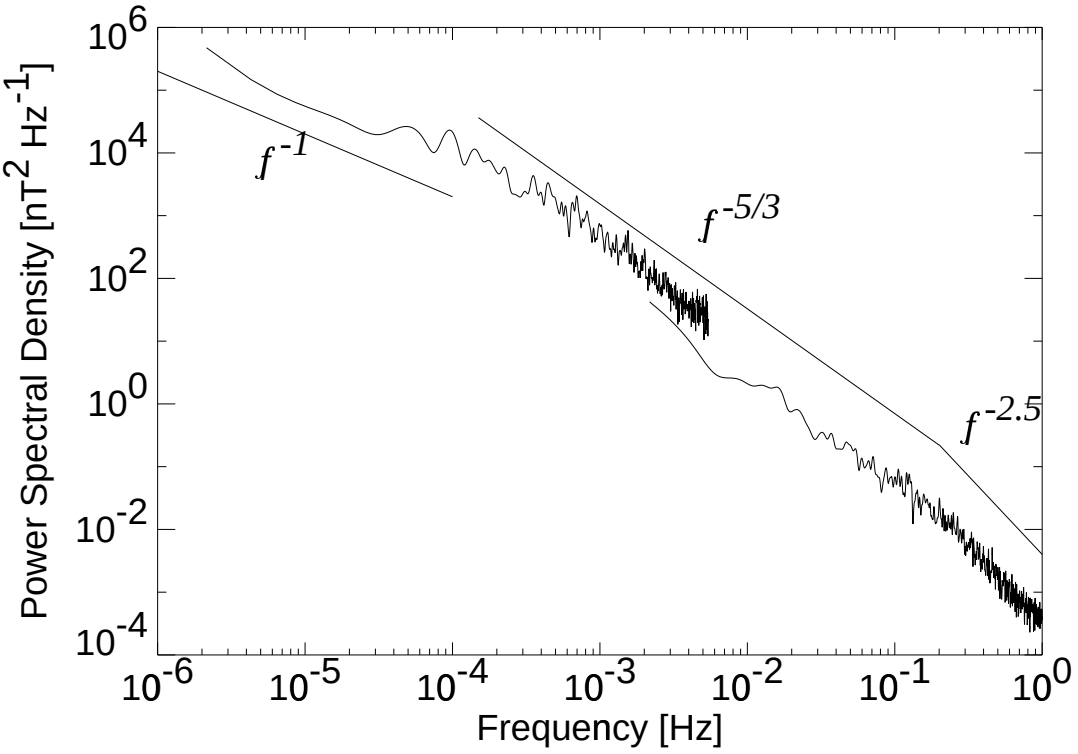

Figure 1.5: Spectrum of fluctuations in the Normal (to the ecliptic) component of the magnetic field showing the three power law ranges. The upper trace is taken from almost five and a half days of quiet solar wind, starting from April 24, 1998, 0000 UT, using 92 second WIND data. The lower trace computes the power spectrum of the last hour of the above interval, April 29, 0800 UT, from 11 vectors per second high-resolution WIND data.

All the results shown are calculated via the Blackman-Tukey algorithm; the FFT method is less accurate and reliable, and the structure function method, in its current state of development, is incapable of calculating magnetic helicity.

Figure 1.5 shows a composite example spectrum of fluctuations in the Normal component of the magnetic field in the solar wind at 1 AU. The Normal component alone is shown to avoid contamination by sector crossings, which the other two components are affected by. (The spectrum of a step function is $\propto f^{-2}$.) Shocks

also distort spectra, for the same reason. There are three clear power law "ranges" visible:

At the largest scales, on the scales of 10–12 hours (few $\times 10^{-5}$ Hz) up to a month (or at least, the 27-day sidereal rotation period of the sun), the spectrum exhibits a $1/f$ form. *Matthaeus and Goldstein* [1986] showed precisely why the spectrum should display this form, in an argument based on the scale-invariance of the correlation length of the turbulence. In travelling up through the corona from the solar surface, a structure undergoes many magnetic reconnections, each of which amplifies the size of the structure and the energy it contains. When this process stops at the Alfvén critical point, the large-scale fluctuations have significant energy. As such, this range is called the "energy-containing range."

At intermediate scales, the "inertial range" is essentially a conduit from the larger scales that contain energy to the smaller scales where that energy is dissipated. *Kolmogoroff* [1941a] first explained theoretically the $-5/3$ power law in the inertial range of hydrodynamic turbulence. His argument was based on dimensional analysis: the power spectral density $E(k)$ at a given wavenumber k can depend only the wavenumber and the transfer or cascade rate, which in turn depends on the triple correlation time, τ_3. *Kolmogoroff* took the triple correlation time to be the eddy turnover time, or nonlinear timescale of the turbulence, $\tau_{NL} = (v_k k)^{-1}$, where $v_k = [kE(k)]^{1/2}$. The $-5/3$ result follows immediately. (See also section 5.1.3.3, and in particular equation (5.6).) *Kraichnan* [1965] suggested that, under some circumstances, the triple correlation time also involved the Alfvén speed, or more precisely, $\tau_3 = \tau_{NL}^2/\tau_A$, where $\tau_A = (kV_A)^{-1}$. A power spectrum with spectral index $-3/2$ follows.[5] *Kolmogoroff*-type spectra are observed predominantly in the solar wind.

[5] *Matthaeus and Zhou* [1989] have shown that the *Kolmogoroff* and *Kraichnan* predictions are the extreme opposite limits (weak and strong magnetic field, respectively) of one more general phenomenology.

The onset of the third range, the "dissipation range," occurs when the competing rates of energy transfer (the spectral cascade) and dissipation due to damping processes balance. In the spacecraft frame, this typically is at scales of a few seconds.

The study of the physics of the dissipation range and its cause are the main aims of this dissertation.

In Figure 1.5, the power law index is -2.5. At 1 AU, this index is seen to vary from about -2 to about -4.5, with an average of about -3. The average index appears to be greater closer to the sun and less at larger heliocentric distances [*Smith et al.*, 1990b]. The reason for the observed spectral index is not well understood for MHD turbulence in the solar wind. Hydrodynamics [*Batchelor*, 1970] predicts a (slow roll-over into a) -7 dissipation range. Some intervals examined for this study (not included in the final 33 events listed in chapter 2) showed some roll-over, indicative of a gradual onset of dissipation.

1.4 Solar Wind Heating

There is now ample evidence that both the inner heliosphere [*Freeman*, 1988; *Marsch*, 1991] and the outer heliosphere [*Richardson et al.*, 1995] are subject to a measurable degree of *in situ* heating, because the radial temperature profile falls off more slowly with distance than the $R^{-4/3}$ decay of adiabatic expansion. This is demonstrated in Figure 1.6. While shock compression may provide a measure of that heating locally [*Zank et al.*, 1996], the dissipation of distributed IMF fluctuations has been argued to provide a means for the majority of the heating of the solar wind in the inner heliosphere [*Coleman*, 1968].

If dissipation of magnetic energy is needed to account for the apparent heating of the solar wind plasma, then the two paradigms discussed above in section 1.2 imply potentially very different heating rates. If the IMF fluctuations are noninteracting waves with distant origins, then the wave energy at a given frequency (assumed to be significantly lower than the cyclotron frequency) is unavailable for

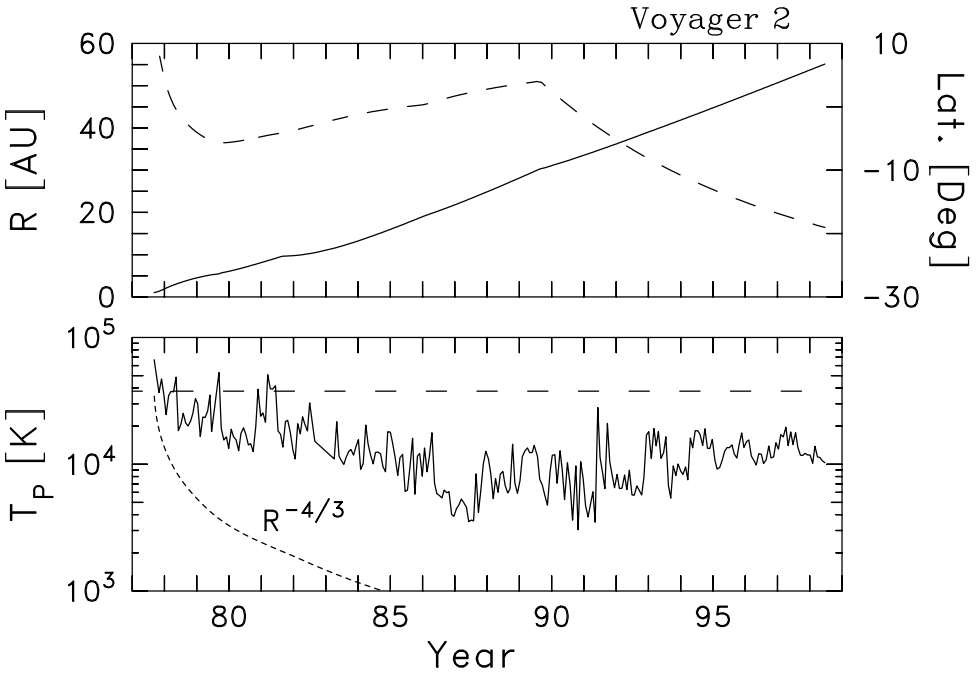

Figure 1.6: Upper panel: Voyager 2's trajectory with both heliocentric distance (solid trace, left-hand scale) and latitude (dashed trace, right-hand scale). Lower panel: proton temperature profile. Superimposed is the $R^{-4/3}$ prediction of adiabatic expansion. The dashed horizontal line is the assumed 1 AU temperature used by *Richardson et al.* [1995].

heating the background ions until the kinetic processes responsible for coupling the fluctuations to the background ions are shifted to that given frequency through changes in the background parameters [cf. *Schwartz et al.*, 1981, Figure 1]. For instance, the proton cyclotron frequency, where resonant dissipation becomes significant for Alfvén waves, scales with the mean magnetic field, $\Omega_p \sim B$, so the cyclotron frequency varies with heliocentric distance as $\Omega_p \sim R^{-1}$ in the outer heliosphere. Within the inner heliosphere, $\Omega_p \sim R^{-2}$. This suggests a relatively slow process whereby the IMF fluctuation spectrum (of solar origin) is damped ('consumed') from the high-frequency end only as the kinetic processes of wave damping shift to lower frequency. This greatly limits the amount of energy available for *in situ* heating of the background ions and has been shown by *Schwartz et al.* [1981] to be inadequate to explain the apparent heating of thermal ions in high-speed streams. Consideration of minor ion species permits cyclotron damping at lower frequencies, but only at reduced rates, because of the reduced number density.

Other damping mechanisms, such as Landau damping [*Barnes*, 1966, 1979; *Stix*, 1992], operate over a wide range of wave frequencies. It is unclear whether or how they would lead to a sharp spectral feature of the type we discuss here. We adopt the implication, taken from traditional fluid dynamics, that a spectral break at the high-frequency end of the inertial range leading to a steepened power spectrum is indicative of the onset of dissipation. Other interpretations are not ruled out by this analysis.

If the IMF fluctuations are fundamentally turbulent with a self-organizing spectrum and active spectral cascade of energy from large spatial scales to small scales, then the so-called "energy-containing fluctuations" at the largest spatial scales [*Batchelor*, 1970] provide a source of energy which is transferred through the inertial range to replenish the depleted high-frequency spectrum and thereby enhance the heating of the background ions. Indeed, such an energy-containing

spectral transfer is the very definition of an inertial range [*Kolmogoroff*, 1941a]. The high-frequency region of the spectrum where magnetic energy is coupled to the thermal motions of the ions is known in traditional fluid turbulence theory as the dissipation range [*Batchelor*, 1970], and is characterized by a steepening of the power spectrum relative to the inertial range, such as is seen in the solar wind at frequencies comparable to the proton gyroradius [*Behannon*, 1975; *Denskat et al.*, 1983; *Smith et al.*, 1990b; *Goldstein et al.*, 1994]. In this way, IMF turbulence may provide an enhanced heating rate relative to the wave paradigm so long as: (1) an active spectral transfer of magnetic energy is maintained to replenish the damped oscillations; and (2) a mechanism is available for coupling the magnetic fluctuations of the dissipation range to the background ions.

The dissipation of magnetic energy can be matched by the spectral transfer rate (indeed, the transfer rate may govern the rate at which energy is dissipated) and yields a stationary spectrum that changes only as the bulk parameters such as Ω_p change.

1.5 Cosmic Ray Propagation

This dissertation does not address the propagation and scattering of high-energy cosmic rays directly, but the presence of a dissipation range has implications for cosmic rays. IMF fluctuations act as scattering centers (in particle pitch angle) for the particles. High energy particles, as well as all particles with pitch angles of $\sim 90^\circ$ are resonant with dissipation range fluctuations.

The seminal work in this field is *Jokipii* [1966], who considered scattering for magnetostatic, dissipationless turbulence with slab geometry through quasi-linear theory. However, there are two major discrepancies between the prediction of this model and observations, as can be seen in Figure 1.7: The predicted mean free paths are "too small," with a typical discrepancy of a factor of 10 for 10 MeV protons; furthermore, the observations have the "wrong" energy dependence, being broadly

consistent with a rigidity-independent mean free path from 0.5 to 5000 MV, whereas theory predicts that the mean free path should increase with increasing rigidity.

Bieber et al. [1988] and *Smith et al.* [1990] showed that changes in the dissipation range spectrum can effect the mean free path of energetic particles. *Bieber et al.* [1994] then suggested a resolution for the mean free path length and rigidity problems by: (*i*) including a dissipation range; and, more important, (*ii*) assuming that 80% of the energy was carried by wave vectors aligned perpendicular to the mean magnetic field. The 80% fraction was merely the value that best fit the mean free path data. *Bieber et al.* [1996] developed a test and found that, on average, 85% of magnetic fluctuations were aligned perpendicular to the mean magnetic field. In section 3.5 we return to discuss Bieber's test in more detail and apply it to our own data.

1.6 Heating Elsewhere in the Solar System

This dissertation concerns the effects and implications of dissipation of magnetic fluctuations at 1 AU. However, it is almost certain that different mechanisms provide the heating of plasma in different regions of the solar system.

Beyond about 20 AU, the damping of waves generated by scattering of pick-up ions is the main source of energy. Current models work reasonably well assuming that all waves are parallel-propagating Alfvén waves that then cyclotron damp. (This far out in the heliosphere the Archimedean spiral magnetic field is almost perpendicular to the radial wind velocity.) The recent work of *Matthaeus et al.* [1999b] suggests that the heating of the solar wind observed beyond 20 AU cannot be explained by shear driven turbulence alone. Driving by injection of wave energy associated with pickup ions works well at a theoretical level [*Williams et al.*, 1995], but such waves are yet to be observed. (There is, however, the possibility that the temperature increase beyond 20 AU is a latitude-dependent effect, and not a radial one [cf. *Williams et al.*, 1995]; since its encounter with Neptune, Voyager 2

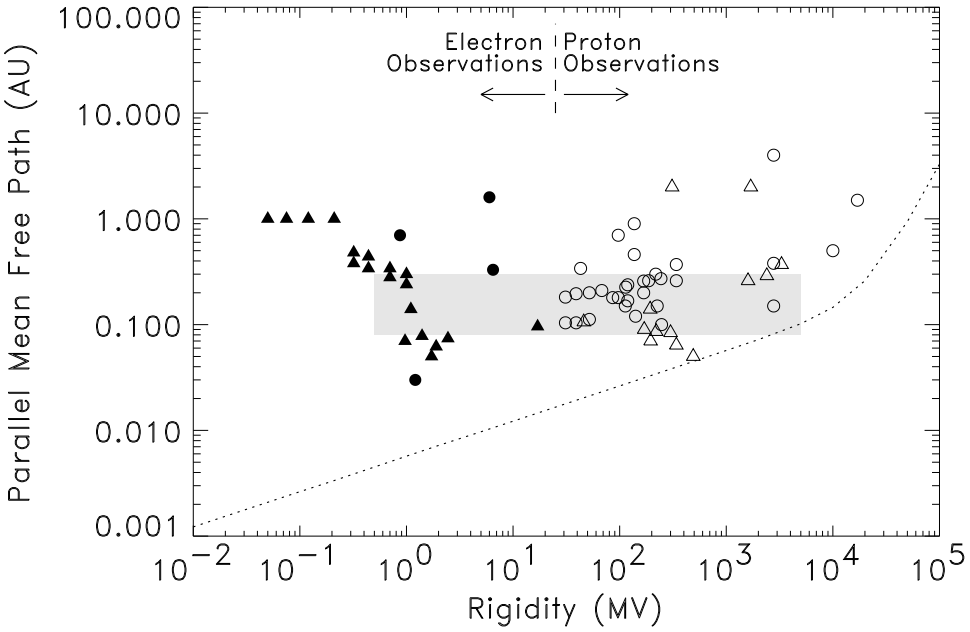

Figure 1.7: Cosmic-ray parallel mean free path vs. particle rigidity. Filled and open symbols denote results derived from electron and proton observations, respectively. Circles and upward-pointing triangles denote actual values and lower-limit values, respectively. The shaded band is the observational consensus enunciated by *Palmer* [1982]. The dotted line represents the prediction of standard quasi-linear theory for magnetostatic, dissipationless turbulence with slab geometry [*Jokipii*, 1966]. Reproduced (with Bieber's permission) from *Bieber et al.* [1994].

trajectory has been increasing in (southern) latitude at the rate of $\sim 2^\circ$ per year, as can be seen in the upper panel of Figure 1.6.)

The heating of the solar corona and acceleration of the solar wind within a few solar radii of the photosphere is another problem that is little understood. Various mechanisms have been proposed; one would think that if damping of electromagnetic plasma waves provides the heating at 1 AU, related damping mechanisms might be valid at distances $\ll 1$ AU. Comparison of similar mechanisms operating at 1 AU and in the corona is complicated by the fact that in the solar corona, below the Alfvén critical point, the Alfvén speed is much greater than either the thermal speed (*i.e.*, $\beta \ll 1$) or the outflow velocity.

1.7 Outline

The study of the physics of the dissipation range and its cause are the main aims of this dissertation. Compared to the larger spatial scales of the inertial range, the dissipation range is largely neglected in previous work. A large fraction of the prior literature is formed by *Behannon* [1975], *Denskat et al.* [1983], *Smith et al.* [1990b] and *Goldstein et al.* [1994]. Whatever the dynamic nature of the fluctuations may be and however the magnetic spectrum may evolve in the solar wind, we can test some aspects of the models for the dissipation dynamics as well as the geometry, *i.e.*, the relative distribution of energy over the full three-dimensional (3-D) space of wave vectors, of the magnetic spectrum using *in situ* measurements. To this end, we examine IMF fluctuations within the dissipation range using WIND data collected at 1 AU.

In chapter 2, the method for characterizing the dissipation range fluctuations is described and we present the basic parameterization of the intervals used in this study.

In chapter 3 these observations are applied, repeating and extending some

classic analyses of inertial range fluctuations at dissipation range frequencies. In testing dissipation dynamics, we consider whether simple models of cyclotron damping of parallel-propagating Alfvén waves can provide sufficient organization of the observations to warrant refined treatments. However, we conclude that such waves are unable to account for the observed characteristics of the dataset. On analyzing the geometry of the fluctuations in the dissipation range, we find that a large fraction of the total power resides in wave vectors that are quasi-perpendicular to the mean magnetic field.

Since parallel-propagating waves fail to explain the observed IMF power spectra, in particular the location of the spectral break frequency, we instead consider predictions from the damping of obliquely-propagating kinetic Alfvén waves. Chapter 4 investigates numerically the dispersion, dissipation and polarization properties of kinetic Alfvén waves, the effects of cyclotron-resonant and Landau damping, and how the effects of the two damping mechanisms change with changing ambient plasma parameters.

Using the results of chapter 4 in chapter 5, a three-dimensional (3-D) spectrum $E(\mathbf{k})$ is constructed that is consistent with the observations, although not unique. From this 3-D spectrum we calculate the heating rate due to the damping of kinetic Alfvén waves, and compare it to the additional heating required to explain the nonadiabatic temperature profile of the solar wind. We also compare the dissipation heating rate to the observed inertial-range turbulent cascade rate.

Finally, in chapter 6, we provide a summary of the work and discuss its contributions in context. Some suggestions of future follow-up studies are also presented.

1.8 Disclaimer

Much of this dissertation has already been published in refereed scientific journals. Chapters 2 and 3 come primarily from 3 papers published in 1998, but reorganized for coherence [*Leamon et al.*, 1998a, in the *Journal of Geophysical Research*].

The discussions of magnetic helicity, Figure 3.2, and the cascade-and-dissipation model of section 3.4 are from *Leamon et al.* [1998b] in *Astrophysics Journal Letters*; and the sections on the January 1997 CME are from *Leamon et al.* [1998c] in *Geophysical Research Letters*. Apart from the didactic presentations of damping mechanisms, the analytic derivation of the dispersion relation and the application of the Vlasov-Maxwell equations (sections 4.2–4.4), chapters 4 and 5 are essentially *Leamon et al.* [1999a], also published in the *Journal of Geophysical Research*. The work in chapters 2, 3, 4, and 5 was reviewed in two papers presented at the Solar Wind Nine conference [*Leamon et al.*, 1999b, c]. This dissertation follows the logical organization of those two conference papers. Finally, parts of the discussion of chapter 6 are from the discussion sections of *Leamon et al.* [1998a].

Chapter 2

THE WIND DATASET, ANALYSIS METHODS AND TECHNIQUES

2.1 Contents

The original study [*Leamon et al.*, 1998a] contained in this dissertation used as its basis a collection of 33 one-hour intervals of data from the WIND Magnetic Field Investigation (MFI) instrument [*Lepping et al.*, 1995] and thermal particle measurements from the SWE instrument [*Ogilvie et al.*, 1995]. WIND was in near-Earth orbit and was typically between $100R_E$ and $200R_E$ upstream of Earth during the intervals in question, recorded between January 1995 and February 1997. Table 2.1 lists the dates and times of those 33 intervals. For all intervals in this study, we use the highest available resolution magnetic field data; depending on the distance from WIND to Earth, the sampling rate was either 46, 92, or 184 ms. The resolution of the plasma data was 92 s.

No attempt was made to limit this study to "...the purest examples of ... outwardly propagating Alfvén waves occur[ring] in high-velocity solar wind streams and on their trailing edges..." as did *Belcher and Davis* [1971] or to exclude disturbance regions such as ICME's or shocked plasma. However, we do attempt to eliminate periods of non-stationary behavior that might lead to spectra that are not representative, and intervals with power spectra that demonstrate significant upstream wave activity (due to apparent magnetic connection to the Earth's bow

Table 2.1: List of the 33 intervals that form the quiet solar wind dataset

Date	Time (UT)	Date	Time (UT)
19950104	0300	19960803	1100
19950129	1830	19960814	1100
19950130	0400	19960816	0800
19950130	1300	19960823	0100
19950327	0100	19960829	0000
19950327	2300	19960904	1100
19950602	1300	19960904	1700
19951019	1430	19961022	0900
19951019	1830	19961023	0100
19951107	0330	19961023	1100
19951225	2000	19961222	0100
19960326	0900	19961225	0100
19960515	0400	19970103	2200
19960522	2200	19970110	0300
19960527	2300	19970128	0700
19960729	0600	19970208	1130
		19970217	1100

shock) are also rejected. Some spectra computed were rejected because no break in the spectrum was visible below the Nyquist frequency.

Only periods that result in power law inertial range spectra are kept; power law dissipation range spectra were almost always seen when a distinct spectral break was observed, and it was generally a poorly determined (*i.e.*, non-powerlaw) inertial range spectrum that led to the rejection of some candidate intervals in this study.

Rapid changes in the computed and employed zero levels of the individual sensor axes have been a problem for the WIND/MFI instrument. Inclusion of these rapid changes generally leads to power spectra without powerlaw forms. We omit such intervals and use only constant-zero sets for each time interval studied.

Candidate intervals were selected by looking at daily time series displays of the data. Almost 100 such intervals were processed, and only those meeting the above-outlined criteria were allowed into the final dataset.

The 33 intervals used here span a wide range of basic plasma parameters:

$$333 \leq V_{SW} \leq 692 \text{ km s}^{-1}$$

$$3.1 \leq \langle B \rangle \leq 28.5 \text{ nT}$$

$$9.1^\circ \leq \Theta_{BV} \leq 87.1^\circ$$

$$0.034 \leq \beta_p \leq 2.75$$

$$18.5 \leq V_A \leq 110.2 \text{ km s}^{-1}$$

$$2.3 \leq n_p \leq 49.5 \text{ cm}^{-3}$$

$$2.24 \times 10^4 \leq T_p \leq 4.09 \times 10^5 \text{ K},$$

which are solar wind speed, magnetic field strength, field-to-flow angle, proton plasma β, Alfvén speed, proton density, and proton temperature, respectively. Candidate intervals were deliberately selected with wide variability in these parameters, since one of the original goals of the study was to see what dependence, if any, there was on these basic plasma parameters.

Figure 2.1 shows the total power spectral density for hour 1300 of January 30, 1995, which is typical in most regards of the events used here. The high-frequency end of the inertial range spectrum is shown at spacecraft frame frequencies $\nu_{sc} <$ 0.44 Hz. The inertial range terminates in a spectral break to a steeper spectral index. This spectral break marks the onset of the dissipation range at $\nu_{sc} > 0.44$ Hz.

2.1.1 The January 1997 Coronal Mass Ejection

Figure 2.2 is a sample interval of the second part of the WIND dataset. Hour 2200 of January 11, 1997 is in a high-speed stream following a large ICME and magnetic cloud. Sixty contiguous hours from January 9, 1200 UT to January 12, 0000 UT were processed by the same method used to produce the 33 solar wind intervals. Ten of these intervals did not produce good spectra, so the second part of the WIND dataset consists of 50 one-hour intervals.

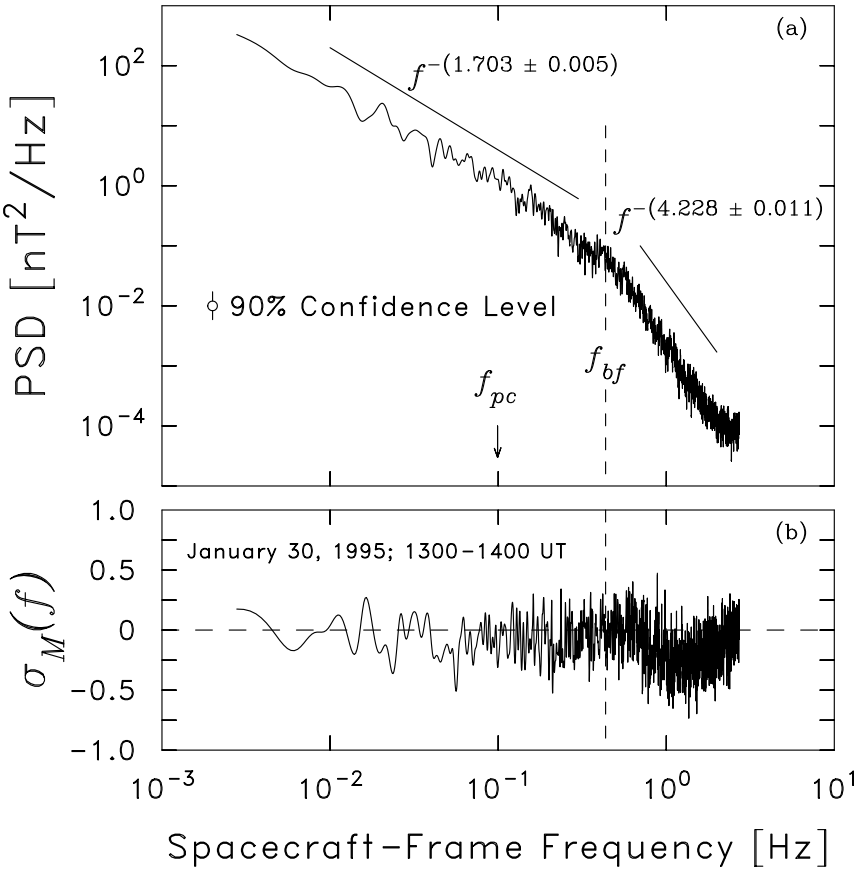

Figure 2.1: Typical interplanetary power spectrum providing an example of inertial and dissipation ranges at 1 AU. (a) Trace of the spectral matrix with a break at ~ 0.4 Hz where the dissipation sets in. (b) The corresponding magnetic helicity spectrum. For this period, $B = 6.4$ nT, $\beta_p = 0.71$, $V_{SW} = 692$ km s^{-1} and $\Theta_{BV} = 23°$.

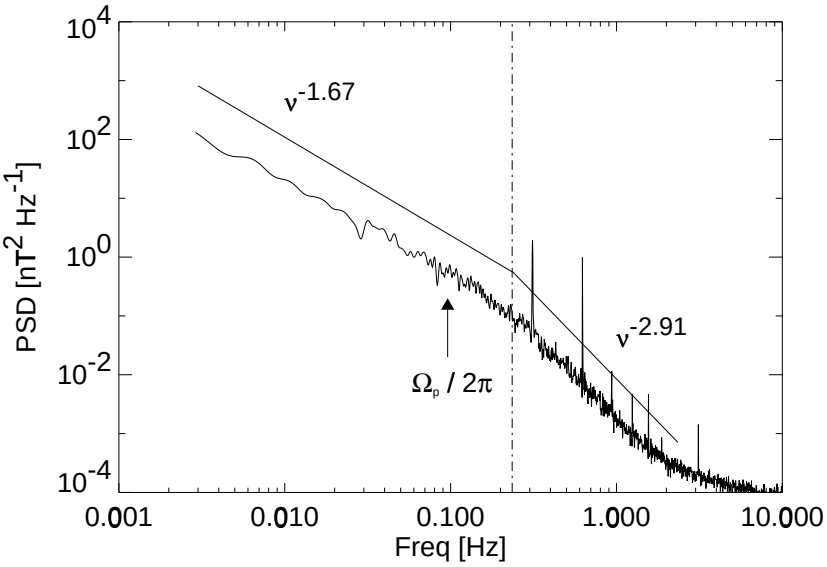

Figure 2.2: Trace of power spectral density matrix for hour 2200, January 11, 1997. For this period, $B = 6.27$ nT, $\beta_p = 0.48$, $V_{SW} = 517$ km s^{-1}, and $\Theta_{BV} = 38.1°$. The spectral break frequency is computed to be 0.235 Hz. Two spacecraft-generated noise signals affect the spectrum: above ~ 1 Hz the spectrum flattens due to onboard clock problems, and sharp peaks are seen at harmonics of 0.33 Hz, the spacecraft rotation rate.

Figure 1.4 on page 12 showed the time series magnetic field data indicating the ICME. The 60-hour interval can be divided into 5 distinct regions [*Burlaga et al.*, 1998; *Leamon et al.*, 1998c]: (*i*) the solar wind prior to the ICME (prior to the shock at day 10.0); (*ii*) the sheath region between the shock and the beginning of the cloud at day 10.2; (*iii*) the magnetic cloud, which is taken to end with January 10, when B starts to increase above 14 nT; (*iv*) the solar prominence material at the beginning of January 11; and (*v*) the solar wind behind the ICME (after day 11.2). For more detailed analyses of the ICME structure, the cloud and the identification of the solar prominence material, see *Burlaga et al.* [1998]. Not shown in Figure 1.4 are the plasma data, which show that the solar wind speed V_{SW} is very low prior to the ICME and high following the ICME; and that V_{SW}, the proton temperature and proton density are all extremely constant within the magnetic cloud.

2.2 Method

We used the following algorithm to analyze each data interval:

1. Eliminate "flyers" and bad points. Any measurement that is more than 3.5× the variance σ from the mean in any component is removed. Typically, 1% of the dataset ($\sim$ 400 points out of 40 000) are removed in this way. Spectra are extremely sensitive to isolated outlying points in a time series, and such points can affect broad ranges of frequency spectra.[1] Details on the inner workings of the badpoint editor are discussed in section A.4.1 of Appendix A.

2. Rotate the data, as necessary, into either RTN (Radial, Tangential, Normal; see Appendix B) or mean-field coordinates. In order to compute magnetic helicity, the data need to be in RTN coordinates (see Appendix A); the anisotropy and geometry analyses of sections 3.1 and 2.3 require mean field coordinates.

[1] Recall that the Fourier transform of a one-point spike is approximately a Gaussian, with a width proportional to the height of the errant spike in the time series.

3. Prewhiten the data with a first-order difference filter to reduce the influence of leakage when computing the spectra of the (steeply-falling) dissipation range.

4. Compute the power spectra using the correlation matrix method of *Blackman and Tukey* [1958]. A maximum lag of 10% of the length of the dataset results in 20 degrees of freedom for the spectral estimates. The resulting spectra are then 'postdarkened' to correct for the earlier prewhitening [*Chen*, 1989; *Bieber et al.*, 1993a]. More details on the prewhitening method can be found in section A.4.2 of Appendix A.

5. Fit power laws to inertial and dissipation range spectra using a least squares fit. We omit frequencies close (within $\sim$ 0.05–0.1 Hz) to the apparent spectral breakpoint when fitting the two spectral ranges. From the intersection of the two power law fits we can calculate the breakpoint frequency for the onset of dissipation.

   On average, the uncertainty in the spectral breakpoint frequency produced by this method is 20% of the computed spectral breakpoint frequency.

2.2.1 Sensor Noise Problems

As mentioned on page 30, the changes in the computed and employed sensor zero levels are a problem for the WIND/MFI instrument.

Figure 2.1 is typical in most respects for the spectra considered here, except that it does not show sharp peaks at harmonics of the spacecraft spin tone. However, these are an almost omnipresent feature in spectra with slightly lower power levels, as illustrated by Figure 2.2. Consequently, these frequencies (harmonics of 0.33 Hz) are omitted from the least-squares fitting of the two ranges using a $\pm$10% window around each harmonic. A flattening of the high-frequency spectrum is evident in Figures 2.1 and 2.2 at frequencies $>$ 1 Hz and is more evident in other intervals with lower power levels and higher Nyquist frequencies. The flattening asymptotes

to $\sim 10^{-4}$ nT^2 Hz^{-1} in Figures 2.1 and 2.2, which seems to be the most common value; in some instances, though, the flat spectrum is as high as $\sim 10^{-3}$ nT^2 Hz^{-1}. The flattened spectrum is not associated with the IMF, and the source of this noise is believed to be a jitter problem with the onboard spacecraft clock.

We omit the highest-frequency flattened spectra from the spectral fitting.

2.3 Turbulence Concepts

In section 1.2, we discussed the paradigm of IMF fluctuations being incompressible turbulent fluctuations. For the most part, the study of a turbulent fluid infused with a magnetic field, or magnetofluid, (such as the solar wind) is similar to the study of Navier-Stokes fluid turbulence, which has a long history. We review briefly the somewhat specialized language of turbulence and its relevance to the current work.

It is useful to adopt a leading order description based upon incompressible turbulence, in view of the low level of interplanetary density fluctuations [*Roberts et al.*, 1987b], the observed density spectrum [*Montgomery et al.*, 1987] and the low average turbulent Mach number [*Matthaeus et al.*, 1990] This perspective is also consistent with the persistence of the $k^{-5/3}$ signature of the *Kolmogoroff* [1941a] inertial range cascade spectrum. Neglecting small internal energy fluctuations, the turbulent energy per unit mass, E, consists of contributions from the turbulent (ion) velocity $\mathbf{v}$ and the fluctuating component of the magnetic field $\mathbf{b}$. It is common in this field to scale magnetic fluctuations to Alfvén speed units, by dividing by $\sqrt{\mu_0 \rho}$ (or $\sqrt{4\pi\rho}$ in cgs-Gaussian units). For an appropriately defined ensemble average $\langle \ldots \rangle$, the contribution to the energy from velocity fluctuations E_v and from magnetic fluctuations E_b is

$$E = E_v + E_b = \frac{\langle |\mathbf{v}|^2 \rangle}{2} + \frac{\langle |\mathbf{b}|^2 \rangle}{2}. \tag{2.1}$$

In its idealized definition, the turbulent energy includes contributions from all wavenumbers and frequencies. However, in some circumstances one might consider only contributions from certain scales, so that, for example, the spectral decomposition of magnetic energy, $E_b = \int d\mathbf{k} E_b(\mathbf{k})$ might include only a certain range of wavenumbers. One might choose to look at the energy in a finite band of wavenumbers or frequencies, for example, when the physics of the inertial- or dissipation range is discussed.

Apart from energy, other quantities of importance for MHD turbulence are the magnetic helicity $H_m = \langle \mathbf{b} \cdot \mathbf{a} \rangle$, where $\mathbf{b} = \boldsymbol{\nabla} \times \mathbf{a}$, the cross helicity $H_c = \langle \mathbf{v} \cdot \mathbf{b} \rangle$, and the respective spectral decompositions [*Matthaeus and Goldstein*, 1982a]. The amounts of cross helicity and magnetic helicity relative to the energy are conveniently measured by the following dimensionless parameters. The normalized cross helicity

$$\sigma_c = \frac{E_+ - E_-}{E_+ + E_-}, \tag{2.2}$$

is defined in terms of the Elsässer energies $E_\pm \equiv \langle |\mathbf{v} \pm \mathbf{b}|^2 \rangle$ [*Marsch and Mangeney*, 1987], and lies between -1 and $+1$. Normalized magnetic helicity

$$\sigma_m = \frac{E_L - E_R}{E_L + E_R}, \tag{2.3}$$

is written here in terms of E_L, the magnetic energy in left-handed (positive helicity) spatial structures, and E_R, the magnetic energy in right-handed (negative helicity) spatial structures, and is similarly constrained to be between -1 and $+1$. Note that $E_b = E_L + E_R$. Right-handed, in this context, means a sense of rotation from the x direction towards the y direction as one samples in the positive z direction for a right-handed $(\mathbf{x}, \mathbf{y}, \mathbf{z})$ coordinate system. Note that this defined a spatial polarization, which is distinct from the time-domain definitions of polarization offered by plasma physics [*Stix*, 1992] or optics [*Born and Wolf*, 1970]. In terms of the integrated

magnetic helicity spectrum,

$$E_L^b = \frac{1}{2}\left(E_b + \int d\mathbf{k}|\mathbf{k}|H_m(\mathbf{k})\right),$$
$$E_R^b = \frac{1}{2}\left(E_b - \int d\mathbf{k}|\mathbf{k}|H_m(\mathbf{k})\right). \quad (2.4)$$

The magnetic helicity is important in the present context because spatial handedness is related to resonance conditions with charged particles. Cross helicity relates to the direction of propagation of large amplitude Alfvén waves with respect to a uniform or slowly varying background magnetic field $\mathbf{B}_0$ [*Belcher and Davis*, 1971; *Matthaeus and Goldstein*, 1982a]. Both together determine the polarization of the waves in the plasma frame [*Smith et al.*, 1984].

Section A.5 of Appendix A discusses the meaning of magnetic helicity and its computation in more detail.

2.4 Preliminary Results and Characteristics

As mentioned above, Figure 2.1 shows the computed spectral fits for one of the 33 intervals from *Leamon et al.* [1998a]. The computed spectral breakpoint frequency is $\nu_{\rm bf} = 0.44$ Hz and the fitted inertial and dissipation range spectra are $\nu^{-(1.70\pm0.01)}$ and $\nu^{-(4.23\pm0.01)}$, respectively. The fitted inertial range spectra for the 33 events range from $\nu^{-(1.46\pm0.01)}$ to $\nu^{-(1.93\pm0.02)}$. The average fit of inertial range spectra is $\nu^{-1.66}$, in excellent agreement with the $\nu^{-5/3}$ prediction of *Kolmogoroff* [1941a]. The dissipation range spectra range from $\nu^{-(2.00\pm0.02)}$ to $\nu^{-(4.43\pm0.01)}$, with the average being $\nu^{-3.04}$. No clear correlation between the fitted indices of the two ranges is observed.

Figure 2.1b shows the normalized magnetic helicity spectrum for that same interval. There is a negative signature at dissipation range frequencies, averaging -0.275 over those frequencies used to calculate the dissipation range spectral slope. The majority of intervals have helicity signatures: 13 out of 33 have $|\sigma_m| > 0.2$; 21 out of 33 have $|\sigma_m| > 0.15$; and 27 out of 33 have $|\sigma_m| > 0.1$. *Goldstein et al.* [1994]

noted similar behavior wherein many, but not all, intervals studied by them showed significant magnetic helicity signatures in the dissipation range. In contrast, inertial range magnetic helicity spectra oscillate randomly as a function of frequency, in agreement with *Matthaeus and Goldstein* [1982a]. We shall return to this result in section 3.2.

The *Belcher and Davis* [1971, p. 3534] examination of inertial range frequencies argues that "the spectra with slower falloffs tend to be associated with higher temperature regions," and we observe this same dependence at a statistical level (see Figure 2.3a). However, it is perhaps more correct to state that the range of inertial range indices narrows with increasing proton temperature and concentrates on the lowest values in the observed range. The dissipation range indices computed in this analysis behave in the opposite sense: high-temperature proton distributions tend to show the steepest spectra (see Figure 2.3b). This suggests that steeper dissipation range spectra are associated with greater heating rates. To a degree this is not consistent with Navier-Stokes theory, but we must remember that plasma dissipation processes are not the same as the νk^2 forms used by *Batchelor* [1970].

The cyclotron frequency computed from the average magnitude of the field for the interval shown in Figure 2.1 is $\nu_{\rm pc} \equiv \Omega_p/2\pi = 0.099$ Hz. It is always the case for the 33 periods examined that $\nu_{\rm pc} < \nu_{\rm bf}$ as shown in Figure 2.4, but it is also the case that $\nu_{\rm pc} > 0.1\nu_{\rm bf}$.

This relationship indicates that ion cyclotron damping may provide an explanation for the onset of the dissipation range. We pursue this possibility in the next chapter.

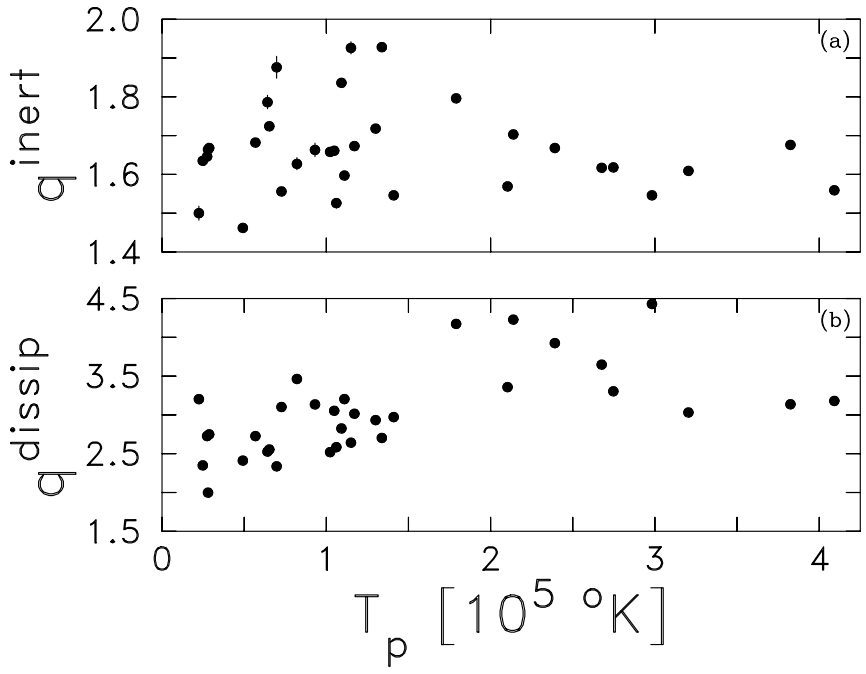

Figure 2.3: (a) Dependence of inertial range spectral index and (b) dissipation range spectral index on solar wind proton temperature.

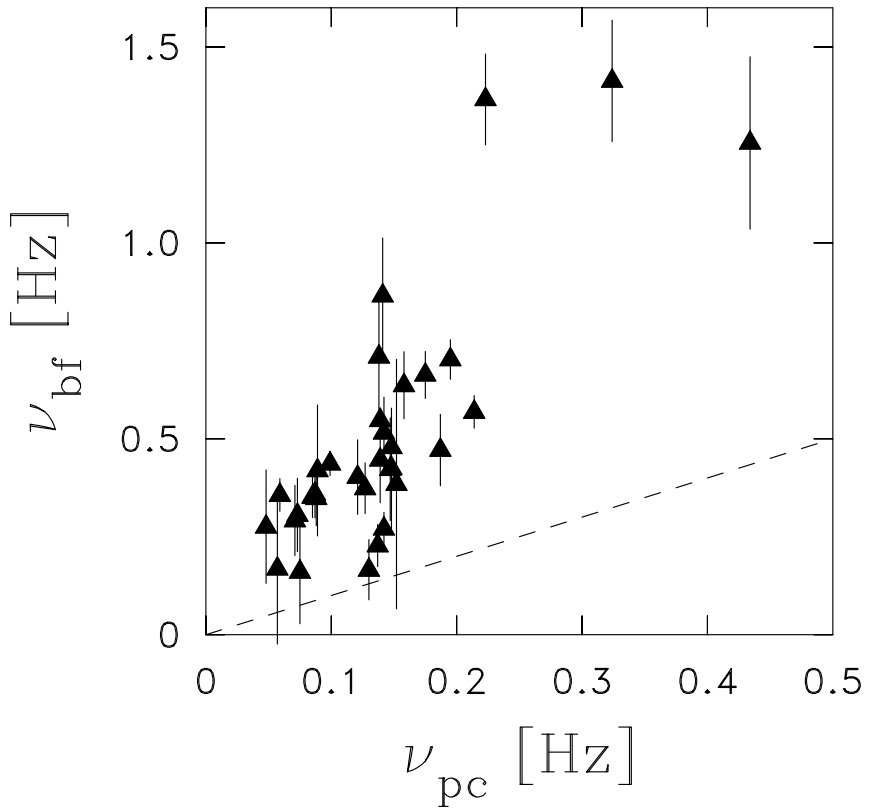

Figure 2.4: Behavior of the observed break frequency $\nu_{\rm bf}$ versus proton cyclotron frequency $\nu_{\rm pc}$. As cyclotron frequency scales with B, the behavior of break frequency with IMF strength is also shown. The dashed curve corresponds to equality $\nu_{\rm bf} = \nu_{\rm pc}$.

Chapter 3

THE CASE FOR AND AGAINST PARALLEL-PROPAGATING, OR 'SLAB,' ALFVÉN WAVES

3.1 Transverse Fluctuations

Belcher and Davis [1971] demonstrate that the inertial range fluctuations $1.6 \times 10^{-4} < \nu_{sc} < 0.04$ Hz are largely transverse to the mean magnetic field. They define a coordinate system relative to the mean magnetic field direction $\hat{\mathbf{B}}$ and radial direction $\hat{\mathbf{R}}$ according to $(\hat{\mathbf{B}} \times \hat{\mathbf{R}}, \hat{\mathbf{B}} \times (\hat{\mathbf{B}} \times \hat{\mathbf{R}}), \hat{\mathbf{B}})$ and conclude that the average variances for these three components have the ratio $5 : 4 : 1$. (*Klein et al.* [1991] and *Chen et al.* [1991] have subsequently shown variations in this result.) We note that this implies a ratio for the total variance transverse to and aligned with the mean field of $9 : 1$. We extend this analysis for inertial range frequencies $0.01 \lesssim \nu_{sc} \lesssim 0.3$ Hz and dissipation range frequencies $0.5 \lesssim \nu_{sc} \lesssim 1.5$ Hz (with large variation due to the location of the computed spectral breakpoint).

For each of our intervals, we rotate the data into the same mean-field coordinate system as *Belcher and Davis* and recompute the power spectra following the method outlined in section 2.2. More details, including the method of matrix rotation are available in Appendix B.

We define $P_{\parallel}$ to be the power in fluctuations parallel to $\hat{\mathbf{B}}$ and $P_{\perp}$ to be the total power in both components perpendicular to the mean field. Therefore $P_{\perp} + P_{\parallel}$ is the total power (trace of the spectral matrix) which is plotted in Figure 2.1. Our

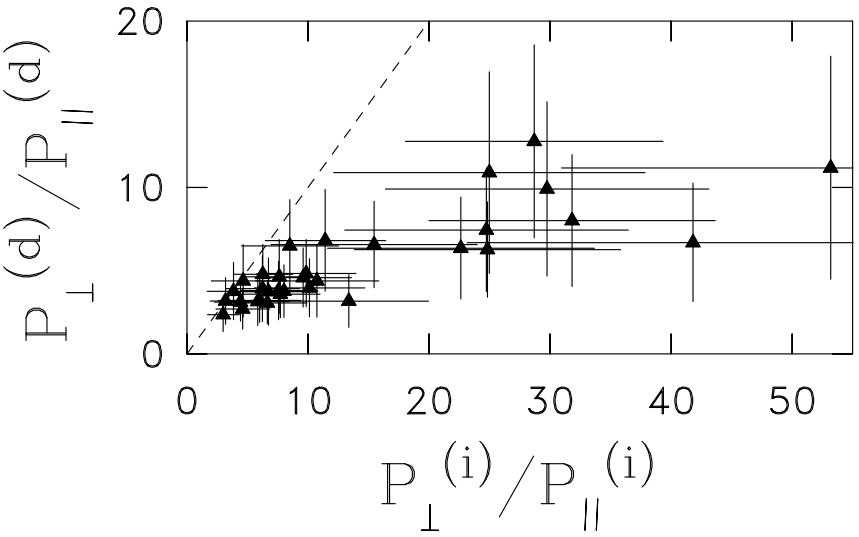

Figure 3.1: Ratio $P_\perp/P_\parallel$ for the inertial (superscript "(i)") and dissipation (superscript "(d)") ranges. The dashed curve again represents equality.

method is different from that of *Belcher and Davis* in that we use spectral power instead of average variance.

For the high-frequency end of the inertial range, we find a mean $P_\perp$:$P_\parallel$ ratio of 14 : 1, with a range $3.0 \leq P_\perp/P_\parallel \leq 53.2$. Taking into account that the above arithmetic mean may be unduly biased by several samples with unusually large values, we note that the geometric mean of $P_\perp/P_\parallel$ is only 10.4, which is in closer agreement with the result of *Belcher and Davis*. For the dissipation range we find a mean ratio of 5.4 : 1 with a range of $2.36 \leq P_\perp/P_\parallel \leq 12.8$ and a geometric mean ratio of 4.9 : 1. A comparison of the ratios of transverse to parallel power for the two spectral ranges is shown in Figure 3.1. The dissipation range ratios $P_\perp/P_\parallel$ are consistently less than inertial range ratios, implying a decreased importance of transverse fluctuations in the dissipation range and a relative increase in the compression of the plasma at these scales.

Belcher and Davis took their observed 9 : 1 geometric mean anisotropy $\delta\mathbf{B} \perp \mathbf{B}$ as evidence of a 'slab,' or one-dimensional, geometry with field-aligned

wave vectors, $\mathbf{k} \parallel \mathbf{B}$. However, the likelihood that the geometry of the magnetic fluctuations is greater than one-dimensional was shown by *Sari and Valley* [1976], who argued that the nonzero spectral power for the parallel component required addition of oblique waves, such as magnetosonic waves, to the slab Alfvén waves. Evidence for IMF fluctuations in association with $\mathbf{k} \perp \mathbf{B}$ was first supplied by *Matthaeus et al.* [1990], based on a "Maltese Cross"-shaped contour plot of the 2-D correlation function. The possibility that these nearly two-dimensional fluctuations with both $\mathbf{k} \perp \mathbf{B}$ and $\delta\mathbf{B} \perp \mathbf{B}$ were, in fact, energetically dominant was established by nearly-incompressible MHD simulations [*Zank and Matthaeus*, 1992a, b] and then shown observationally by *Bieber et al.* [1994, 1996].

All of these potential geometries are consistent with the observations of a large IMF fluctuation anisotropy. We return to this issue in section 3.5, where we determine the geometry of the fluctuations.

3.2 Helicity Analyses

In section 2.4 we noted that most, but not all, dissipation range spectra have moderate bias in the magnetic helicity. Again using our exemplary period of Figure 2.1, we note that $\langle B_R \rangle = -4.9$ nT and $\langle B_R \rangle \langle \sigma_m \rangle > 0$, which implies either a predominance of outward propagating, right-hand polarized waves or inward propagating, left-hand polarized waves [*Smith et al.*, 1983]. If we repeat this same analysis for all 33 quiet solar wind periods in the *Leamon et al.* [1998a] study, we find that only six intervals have $\langle B_R \rangle \langle \sigma_m \rangle < 0$.

We are unable to infer the propagation direction for dissipation range fluctuations because of the time resolution of the plasma data. However, if we compare the magnetic helicity in the dissipation range with the cross helicity σ_c in the inertial range and assume that the dissipation range cross helicity is the same as for the inertial range, then we find that only three of the 33 intervals studied have magnetic helicity signatures that are inconsistent with ion cyclotron damping of Alfvén waves

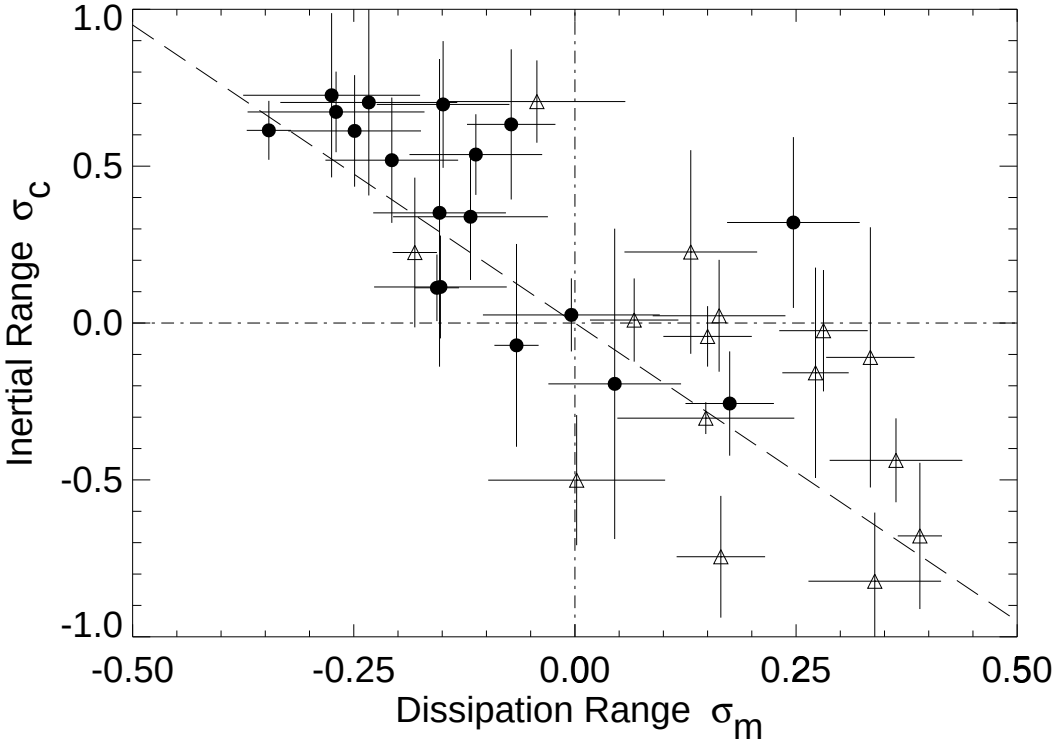

Figure 3.2: Scatter plot, for 33 Wind data intervals, of the normalized cross helicity in the inertial range, σ_c, vs. the normalized magnetic helicity in the dissipation range, σ_m. Triangles are intervals with outward-directed mean magnetic field, and bullets have inward mean fields. The dashed line corresponds to the best-fit line through the origin, $\sigma_c = -1.90\sigma_m$.

[*Stix*, 1992]. Let us now consider in greater detail the data underlying the latter conclusion.

In Figure 3.2 we show the normalized cross helicity σ_c computed from inertial range data, plotted versus the normalized magnetic helicity σ_m in the dissipation range, for the 33 data intervals previously analyzed. Cross helicity H_c can be computed only in the inertial range due to limited sampling rates for plasma data; we use the inertial range H_c as a proxy for the same quantity that is unmeasurable in the dissipation range. In effect, we are assuming that the propagation direction of fluctuations in the dissipation range is the same as the propagation direction of fluctuations in the inertial range. The most notable limitation of this substitution derives from the possibility that preferential dissipation may lead to different cross helicity values in the dissipation range, although there is no observational evidence for this. Indeed, the connection between cross helicity and propagation direction may be complicated in the dissipation range if various kinetic wave modes such as whistlers are present. On the other hand, lower frequency observations of σ_c [see *Matthaeus and Goldstein*, 1982a] often indicate that a single direction of propagation is dominant over several orders of magnitude of scale, which would tend to support the extrapolation into the higher, dissipation range frequencies.

It is apparent from the data in Figure 3.2 that most intervals for which the mean magnetic field is outwardly directed have $\sigma_m > 0$ and $\sigma_c < 0$. On the other hand, inwardly directed $\mathbf{B}_0$ is associated with $\sigma_m < 0$ and $\sigma_c > 0$. This implies a predominance of outward propagating waves. One can readily see that this is consistent with cyclotron-resonant absorption of outward-propagating fluctuations by thermal protons, as follows. A proton moving outward along the magnetic field executes a left-handed helical trajectory. Waves propagating outward at the Alfvén speed will overtake most thermal particles (as $\beta \approx 1$) and therefore, on average, the thermal protons will be in resonance with such waves that have a right-handed

spatial handedness (negative H_m). If the energy of these waves is assumed to be damped by the resonant protons, the energy that remains will preferentially reside in the undamped fluctuations, which have a left-handed structure and positive H_m [see, *e.g.*, *Moffatt*, 1978]. Consequently, outward $\mathbf{B}_0$ should be associated with $\sigma_c < 0$ (outward propagation) and $\sigma_m > 0$. Reversing the direction of $\mathbf{B}_0$ but maintaining the assumption of outward propagating waves (now $\sigma_c > 0$) produces the conclusion that $\sigma_m < 0$ in the dissipation range by the same argument.

The three periods in the top-right and bottom-left quadrants of Figure 3.2 could be consistent with ion cyclotron damping if $\beta_p \gg 1$, which would alter the range of polarizations that provide resonance with thermal ions, but in the three cases here, $\beta_p = 0.034$, 0.191, and 0.885. We find no unique features to otherwise segregate these three intervals as atypical for the set. For the remaining 30 intervals, the magnetic- and cross-helicity analyses suggest that the dissipation range is generally consistent with the depletion of Alfvén waves. (Bullets in the lower-right quadrant of Figure 3.2 and triangles in the upper-left quadrant are consistent with inwardly propagating waves.) This correlation appears encouraging with regard to the inertial range cross helicity proxy used in generating Figure 3.2.

Several damping mechanisms can readily be considered for the formation of the dissipation range (see *Barnes* [1979] for a discussion of several, including Landau damping). The apparent depletion of outward propagating Alfvén waves at frequencies comparable to the proton cyclotron frequency (Figure 2.1b) naturally suggests resonant cyclotron damping of Alfvén waves as a leading candidate, as first suggested by *Coleman* [1968]. We pursue this suggestion with a series of tests which use the cyclotron damping mechanism in an attempt to predict the onset of the dissipation range.

3.3 Cyclotron-Resonant Alfvén Wave Damping

For frequencies $\omega_r \ll \Omega_p$, where ω_r is the plasma-frame wave frequency and Ω_p is the proton cyclotron frequency, the dispersion relation for left-hand polarized Alfvén-ion cyclotron waves, hereafter Alfvén waves, propagating parallel to the magnetic field is [*Stix*, 1992]:

$$\omega_r = k_\parallel V_A, \tag{3.1}$$

where $k_\parallel = \mathbf{k} \cdot \hat{\mathbf{B}}$ is the wavenumber component parallel to the ambient magnetic field and the V_A is the Alfvén speed. For higher frequencies, dissipation becomes important and the solution becomes dispersive. Figure 3.3 shows two solutions to the linearized Vlasov-Maxwell equations for two values of $\beta = v_{th}^2/V_A^2$ that extend into the range where dissipation becomes significant. (The quantity V_A/Ω_p, which is identically equivalent to c/ω_{pi} a nomenclature sometimes preferred by other authors, is the ion inertial scale and provides a natural scaling factor for dimensionless wavenumbers.) We assume single-temperature Maxwellian distributions for both protons and electrons with $T_p = T_e$. The solutions for ω_r approach Ω_p asymptotically as dissipation increases. Dissipation sets in at lower wavenumbers for hotter distributions (larger β) so that the onset of dissipation depends on the proton temperature.

The resonance condition for cyclotron damping in the plasma frame is

$$\omega_r - \mathbf{k} \cdot \mathbf{v} = \pm\Omega_p, \tag{3.2}$$

where $\mathbf{v}$ is the particle velocity. For outward propagating waves and inward moving ions we can reduce the resonance condition to a prediction for the minimum resonant wavenumber:

$$\omega_r + k_\parallel v_p = +\Omega_p, \tag{3.3}$$

where v_p is the proton speed.

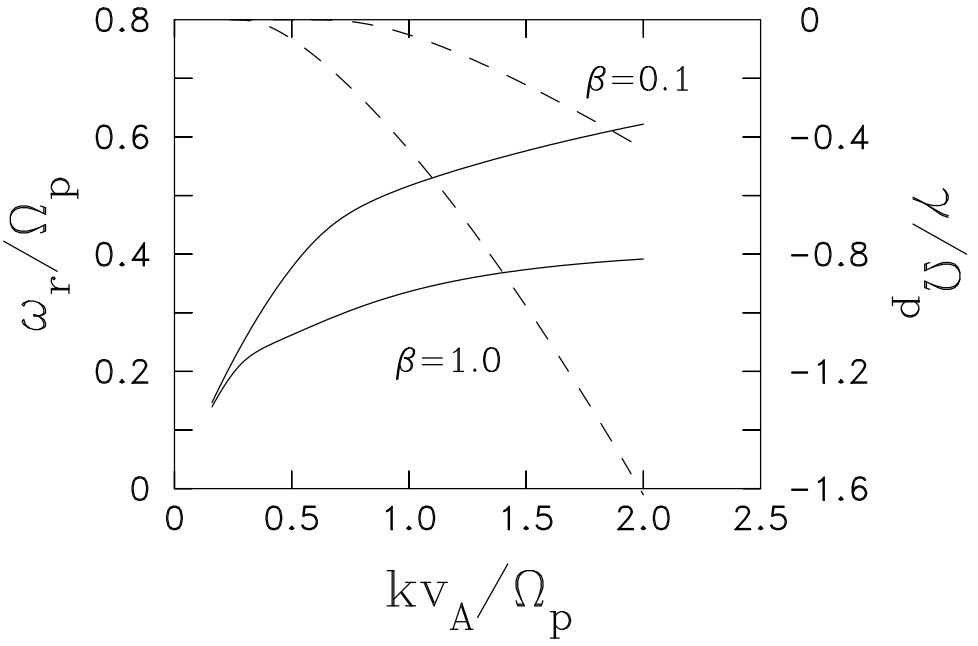

Figure 3.3: Dispersion relations based on numerical solutions of the linearized Vlasov-Maxwell equations. The real part of the frequency, ω_r, is given by the solid curve and left-hand scale. The imaginary part, or decay rate, γ, is given by the dashed curve and right-hand scale. The top two curves for ω_r and γ give the solution for $\beta = 0.1$ and the bottom two curves give the solution for $\beta = 1.0$.

The (Maxwellian) spread of particle speeds, v_{th} results in a spread of wavenumbers that can resonate with the protons. We have two methods to calculate the frequency at which dissipation begins.

3.3.1 Simple Slab Calculation

We assume that $v_p = v_{th}$ and that damping sets in at $\omega_r = kV_A \ll \Omega_p$. Substituting this into the resonance condition (equation (3.3)) gives

$$k_d = \frac{\Omega_p}{V_A + v_{th}} \tag{3.4}$$

as an estimate for the minimum, outward propagating wavenumber at which dissipation by resonance with the background ion distribution becomes important. In principle, if the dissipation range is made up of outward propagating Alfvén waves, then this estimate for k_d should determine the onset of the dissipation range. We can use Figure 3.3 as a rough check of the validity of the estimate of equation (3.4). When $\beta_p = 1$, $V_A = v_{th}$, and $kV_A/\Omega_p = \frac{1}{2}$, we can see from Figure 3.3 that this corresponds to $\gamma/\Omega_p \simeq -0.05$, indicating that dissipation has begun. However, by combining $kV_A/\Omega_p = \frac{1}{2}$ with equation (3.1), we obtain $\omega_r/\Omega_p = \frac{1}{2}$, which is an overestimate. Following the second set of traces for $\beta_p = 0.1$ predicts $\omega_r/\Omega_p = kV_A/\Omega_p = 0.9$, which again gives reasonable dissipation rates of $\gamma/\Omega_p \simeq -0.05$ but overestimates ω_r.

Once we have established the wavenumber at which dissipation starts, we may use the Doppler shift to compute the frequency of an (outward propagating) Alfvén wave resonant with a particle with the mean thermal speed,

$$\nu_{sc} = \frac{\mathbf{k} \cdot \mathbf{V}_{SW}}{2\pi} + \frac{\omega_r}{2\pi}. \tag{3.5}$$

It is possible to find a lower-frequency wave at which the same dissipation rate is present, but this would be an inward propagating solution. If present, the dissipation of this wave may be obscured by the outward-propagating wave at the same

spacecraft-frame frequency with less dissipation (in one dimension, there are only two waves with the same spacecraft frequency), so presumably they would retain greater energy. In either case, the conclusions are nearly equivalent.

3.3.2 Numerical Solution Calculation

Alternately, we can apply the numerical solutions of the type shown in Figure 3.3 and assume that the dissipation range begins when $|\gamma|$ is some fraction of ω_r; say, one third or one tenth. That is, we are considering departures from the dispersion relation of equation (3.1). We then take the the critical wavenumber k_d and wave frequency $\omega_r(k_d)$ from the numerical solutions. We can again use equation (3.5) to translate to a spacecraft-frame frequency.

Since we are assuming parallel-propagating waves, *i.e.*, $\Theta_{BV} = \theta_{kV}$, the vector dot product in equation (3.5) implies a dependence on Θ_{BV} for the dissipation onset frequency for both the numerical solution and slab calculation.

3.3.3 Results

Figure 3.4 shows two events that are almost identical in ambient parameters but with very different field-to-flow angles Θ_{BV}: 23° and 87°. Using the observed average plasma parameters ($\langle B \rangle$ = 6.4 nT, n_p = 3.8 cm^{-3}, β_p = 0.71, V_{SW} = 692 km s^{-1}, and Θ_{BV} = 23°), the prediction for the spectral breakpoint of the first event (the top trace in Figure 3.4) using the simple slab calculation is 0.59 Hz. This is in relatively good agreement with the measured breakpoint value of 0.44 Hz. The average plasma parameters for the second event (the bottom trace in Figure 3.4) are $\langle B \rangle$ = 4.6 nT, n_p = 3.8 cm^{-3}, β_p = 0.67, V_{SW} = 524 km s^{-1}, and Θ_{BV} = 87°. The $\mathbf{k} \cdot \mathbf{V}_{SW}$ term in equation (3.5) is smaller by a factor of $\cos 87° / \cos 23° = 0.06$, implying that the propagation term dominates in the second case, and the observed spectral breakpoint should be ~ 1 decade lower in frequency in the spacecraft reference frame. The predicted spacecraft-frame frequency for the

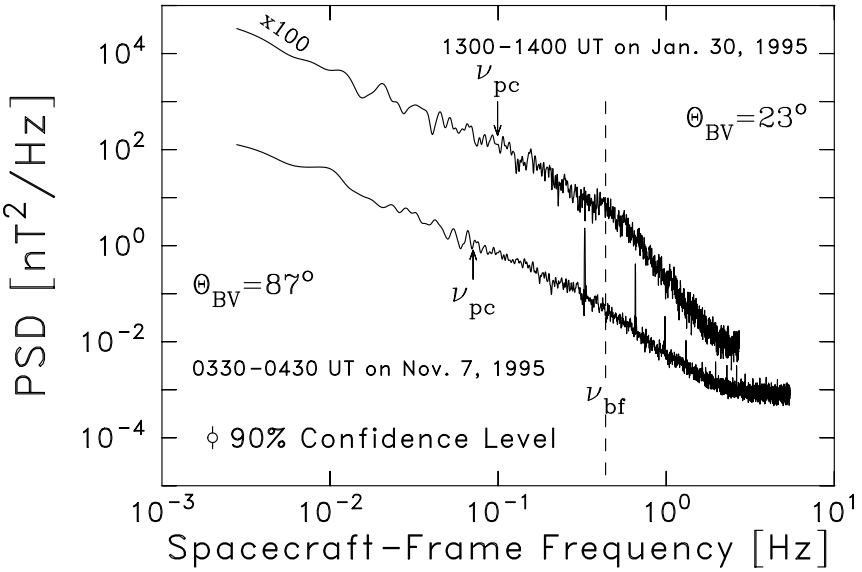

Figure 3.4: Two examples. The top curve is the same spectrum shown in Figure 2.1, and the bottom curve is from November 7, 1995. The two intervals have similar $\langle B \rangle$, β, and V_{SW} but very different values of Θ_{BV}; the second example has the magnetic field almost perpendicular to the solar wind flow. Strong spacecraft spin tone harmonics and an unusually high level of the flat spacecraft noise spectrum, as discussed in section 2.2.1, are evident in the bottom trace. Since WIND was also in its high-rate data mode during this interval, the sampling rate, and thus the Nyquist frequency, are twice that of the earlier example.

spectral breakpoint in this instance using the simple slab model is 0.08 Hz, which is very different from the observed value of 0.29 Hz. The nearly identical frequencies marking the onset of the dissipation range for these two events contradict the expectations and the predictions of parallel-propagating, cyclotron-damped Alfvén wave theory.

These two events are not exceptions to the rule. Figure 3.5 compares the observed spectral breakpoint frequencies with the predicted spectral break frequencies derived from three cases of the two cyclotron resonance models above (simple slab model plus numerical solutions at $|\gamma| = \omega_r/10$ and $|\gamma| = \omega_r/3$). Although all three cases give order-of-magnitude agreement with the observations, none exhibits any close correlation with the observations. The models are unsatisfactory. This might only reflect the simplicity of these three models were it not for an underlying order in the results which is not evident in Figure 3.5.

The systematic error of the theories is revealed in Figure 3.6, where we plot the fractional error of the theory relative to the observation, $(\nu_{\rm bf} - \nu_{\rm theory})/\nu_{\rm bf}$, for

1. the simple calculation (triangles);

2. the numerical solutions for $|\gamma/\omega_r| = 0.1$ (squares); and

3. the numerical solutions for $|\gamma/\omega_r| = 1/3$ (circles).

All three theories exhibit a broad scatter of error and the theories tend to overestimate the observations for values of $\Theta_{BV} < 50°$. The fractional error increases systematically for $\Theta_{BV} > 50°$. To demonstrate that the observations are best fit by a theory of non-field-aligned wave vectors, the solid curve is the predicted fractional error that would result from Doppler shifting an isotropic (radial) wave vector that is erroneously assumed to be field-aligned. If $k_r \equiv 2\pi\nu_{\rm bf}/V_{SW}$ is the (true) breakpoint wavenumber measured along the (radial) solar wind direction, then $k_\parallel = k_r/\cos\Theta_{BV}$ is the predicted wavenumber that is aligned with the magnetic

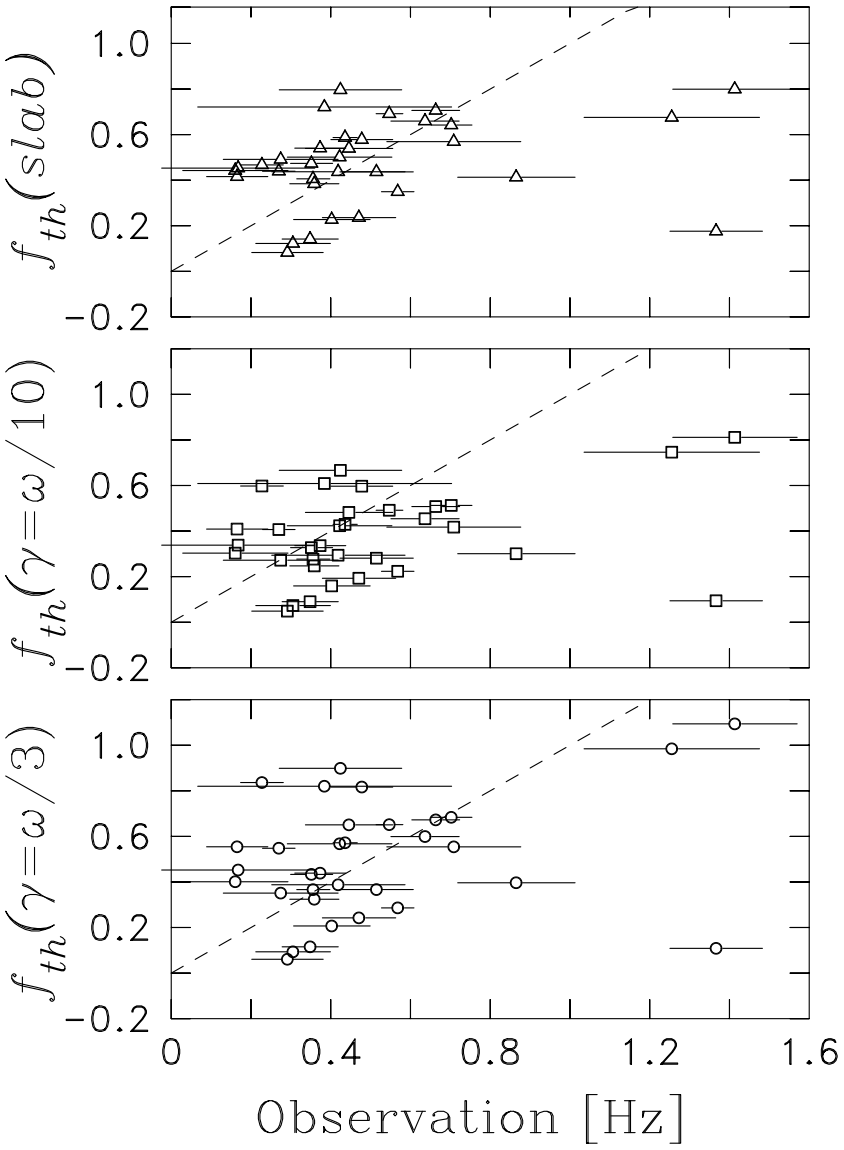

Figure 3.5: Comparison of observed spectral breakpoint frequency with predictions derived from (top) the simple slab model (triangles) and the numerical results for (middle) $|\gamma| = \omega_r/10$ (squares) and (bottom) $|\gamma| = \omega_r/3$ (circles). Dashed curves represent equality. Although the predictions are generally in order-of-magnitude agreement with the observations, the necessary linear scaling is not observed.

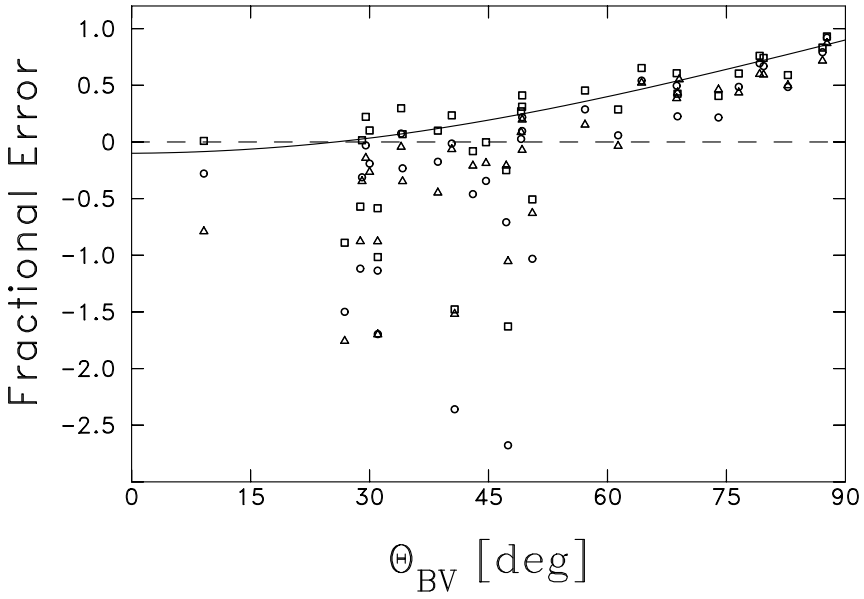

Figure 3.6: Fractional error, defined as $(\nu_{\rm bf} - \nu_{\rm theory})/\nu_{\rm bf}$, for all three models discussed in the text as a function of field-to-flow angle. The symbols are the same as in Figure 3.5. The error is greatest at large angles, true for all wave formulations.

field. We take $\omega_r = 0.1 k_r V_{SW}$ to complete the Doppler shift, *i.e.*, $V_A/V_{SW} \simeq 0.1$. The predicted error (solid curve) is then $0.9 - \cos\Theta_{BV}$, which a good fit to the data points for $\Theta_{BV} > 50^\circ$ in Figure 3.6. This demonstrates that the imposition of a Θ_{BV} dependence upon the observations leads to a systematic error in the results.

It is evident from the data and this analysis that any explanation of magnetic dissipation in the solar wind based on a slab-like, 1-D geometry is likely to contradict observations. We recognize that our treatment here, while using a fully numerical solution of the dispersion relation, can be improved by considering numerous aspects of the plasma, including, for instance, multitemperature Maxwellian distributions. Even so, we contend that any wave mode thought to be associated with the damping process and that propagates at less than the solar wind speed will suffer from a systematic introduction of error if the wave vector is required to be field aligned. This can only be avoided if

1. a systematic correlation between Θ_{BV} and some critical plasma parameter exists that fundamentally alters the resonant process for large Θ_{BV}, or

2. the geometry of the magnetic fluctuations is greater than one-dimensional.

In the remainder of this dissertation we pursue this latter possibility.

3.4 Cascade and Dissipation

We shall return to discuss the exact nature of the oblique fluctuations in subsequent chapters. However, oblique wave fluctuations are generally susceptible to Landau damping [*Barnes*, 1979].

Landau damping affects both right-hand and left-hand polarized fluctuations without regard to polarization, and thus affects the scatter of points in Figure 3.2, as we shall now show.[1] The handedness argument used in section 3.2 explains the clustering of the observational points in the upper-left and lower-right quadrants. However, there are questions that arise. First, if kinetic processes are assumed to be very rapid, why is the signature in the magnetic helicity not pure (± 1) as one would expect for complete cyclotron absorption? Second, how is the above argument modified if instead of pure cyclotron-resonant absorption processes, there is also a contribution due to Landau resonance or nonresonant absorption? Finally, since the observed cross helicities are not "pure," what is the effect of relaxing the assumption of purely outward traveling Alfvén waves?

It turns out that these questions can be addressed, in at least a preliminary fashion, by postulating a cascade and associated dissipation processes that are described by a set of energy balance equations, as follows:

[1] Wave modes of different polarizations may Landau damp at different rates because of the different $E_{\|}$ they generate, but this is a property of the wave mode, rather than the polarization of the wave itself. The assumption we make in this section is that non-cyclotron contributions to the damping are equal for left- and right-hand polarities.

$$\begin{aligned} \frac{dE_L}{dt} &= \frac{S}{2} - \gamma_0 E_L - \gamma_r E_L \\ \frac{dE_R}{dt} &= \frac{S}{2} - \gamma_0 E_R \end{aligned} \tag{3.6}$$

The energies in left- and right-handed spatial structures are respectively designated as E_L and E_R following our discussion of the various turbulence concepts in section 2.3 (in this case the integration over the spectrum now includes, by assumption, only the dissipation range). The rate of supply of energy (per unit mass) transferred into the dissipation range from the inertial range is designated by S. This supply rate is equally apportioned to L and R fluctuations since H_m is random in the inertial range. We assume that the only external contribution to $dE_{L,R}/dt$ is due to the cascade term S, and that in the dissipation range there is no exchange between E_L and E_R, or exchange between kinetic and magnetic energies. The quantity γ_r represents a decay rate due to cyclotron-resonant absorption by thermal protons, and it appears only in the L equation since we assume that fluctuations are outward propagating and $\mathbf{B}_0$ is inward. (This would also occur for inward propagation and outward $\mathbf{B}_0$.) The remaining damping term, γ_0, appears in both the L and R equations and represents decay processes that produce no signature in the magnetic helicity. Included in γ_0 are contributions from Landau damping and other mechanisms that do not involve cyclotron resonance, as well as mechanisms that are fully nonresonant.

We can now proceed to estimate a typical relative strength of cyclotron-resonant and non-cyclotron resonant processes. If we suppose that the cascade is steady, so that $dE_{L,R}/dt = 0$, we may equate the right hand sides of equations (3.6). From the data, we take a typical value of magnetic helicity to be $\sigma_m \approx -1/3$. This corresponds in equation (2.3) to $E_R = 2E_L$ in the dissipation range. Then, for consistency with equations (3.6), we must have $\gamma_0 \approx \gamma_r$, indicating that cyclotron and non-cyclotron absorption mechanisms are approximately of equal strength.

Since observed values of H_c are not pure, the above argument should be refined to account for a distribution of propagation directions relative to the slower thermal protons. Assume, then, that there is a probability $P(L)$ that fluctuations are propagating outward, which produces a resonance between left-handed structures and thermal protons, and implies the appearance of γ_r in the E_L equation. Assigning the probability of inward propagation to be $P(R) = 1 - P(L)$ implies that resonance between right-handed structures and thermal protons is weighted accordingly. Therefore, the cascade balance equations become:

$$\begin{aligned} \frac{dE_L}{dt} &= \frac{S}{2} - \gamma_0 E_L - P(L)\gamma_r E_L \\ \frac{dE_R}{dt} &= \frac{S}{2} - \gamma_0 E_R - P(R)\gamma_r E_R \end{aligned} \tag{3.7}$$

According to the *Elsässer* [1950] representation, fluctuations with energy E_- tend to propagate parallel to the mean field $\mathbf{B}_0$ while fluctuations having energy E_+ tend to propagate antiparallel to $\mathbf{B}_0$. We assume for simplicity that the probability that, at any location in the plasma, a typical thermal proton will "see" outward propagation is proportional to the average outward propagating energy. Thus,

$$P(L) = \frac{E_-}{E_- + E_+} = \frac{1 + \sigma_c}{2} \tag{3.8}$$

and therefore $P(R) = (1 - \sigma_c)/2$.

With this interpretation, we can make use of the data in Figure 3.2 to constrain our model and arrive at further insights about the dissipation processes. From the steady form of equations (3.7), along with the definitions of equations (2.2), (2.3) and (3.8), and assuming that γ_0 and γ_r are independent of σ_c, σ_m and other plasma turbulence parameters, we find that

$$\sigma_c = -\left(1 + 2\frac{\gamma_0}{\gamma_r}\right)\sigma_m. \tag{3.9}$$

The best-fit line forced through the origin is $\sigma_c = -1.90\sigma_m$, while the best-fit straight line through the data is $\sigma_c = -1.80\sigma_m + 0.10$. Considering either 32

or 31 degrees of freedom accordingly, the reduced chi-squared values of the two fits are $\chi_r^2 = 1.78$ and 1.55. Putting $\sigma_c = -1.90\sigma_m$ in equation (3.9) implies that $\gamma_r = 2.22\gamma_0$. The other important consequence of equation (3.9) is that only when $\gamma_0 = 0$ do pure Alfvén waves lead to exclusively helical states.

3.5 Quasi-2-D (Oblique) Wave Vectors

In section 3.1 we considered the spectrum of fluctuations in a field-aligned coordinate system and found that the ratio of power in the two perpendicular directions to the parallel direction decreased in the dissipation range with respect to the inertial range (Figure 3.1). Following *Bieber et al.* [1996], in a test based on the analysis of *Oughton* [1993], we can use the ratio of the power in the two perpendicular directions as another test of the geometry of the fluctuations.

Define a right-handed orthogonal coordinate system in which the z axis is aligned with the mean magnetic field and points away from the Sun, the x axis is in the plane defined by the mean field and the solar wind velocity vector (assumed to be radial) and also points away from the Sun, and the y axis completes the right-handed system. This is the $(\hat{\mathbf{x}}, \hat{\mathbf{y}}, \hat{\mathbf{z}})$ system used by *Bieber et al.* [1996]; *Belcher and Davis* [1971] used the equivalent right-handed triad $(\hat{\mathbf{y}}, -\hat{\mathbf{x}}, \hat{\mathbf{z}})$. $P_{zz}(\nu)$ is, therefore, the power spectrum of fluctuations parallel to $\mathbf{B}_0 \equiv \langle \mathbf{B} \rangle$. *Bieber et al.* call $P_{xx}(\nu)$ the "quasi-parallel spectrum" $P_{(\parallel)}(\nu)$ because the fluctuation component under consideration (x) has a component parallel to the sampling direction; similarly, they denote $P_{yy}(\nu)$ as the "perpendicular" spectrum $P_{(\perp)}(\nu)$ because the y component is perpendicular to the (radial) sampling direction. (The *Bieber et al.* terminology is based upon standard turbulence nomenclature [*e.g.*, *Batchelor*, 1970].) The total spectrum for fluctuations perpendicular to the mean magnetic field $P_\perp$, as discussed in section 3.1, is

$$\begin{aligned} P_{\perp}(\nu) &= P_{(\parallel)}(\nu) + P_{(\perp)}(\nu) \\ &= P_{xx}(\nu) + P_{yy}(\nu). \end{aligned}$$

In this notation, the familiar *Belcher and Davis* [1971] result becomes $P_{(\perp)} : P_{(\parallel)} : P_{zz} = 5 : 4 : 1$.

3.5.1 Slab and 2-D Fluctuations

To conduct our ratio test of turbulence geometry, we first assume a two-component model, which is a composite of slab and 2-D geometries. Although the results of sections 3.1 and 3.3 allow for the possibility of oblique wave vectors at other than 0° and 90° relative to $\mathbf{B}_0$, we will adopt this limitation for the purpose of demonstration. Theoretical models and observational evidence suggest the presence of a significant 2-D component [*Matthaeus et al.*, 1990; *Zank and Matthaeus*, 1992a; *Bieber et al.*, 1994, 1996].

Again following the notation of *Bieber et al.* [1996], the amplitudes of the two components of the model are C_S and C_2; *i.e.*, the slab spectrum in the range of interest is parameterized by $C_S\nu^{-q}$, and the 2-D spectrum by $C_2\nu^{-q}$. The "slab fraction" r is the contribution of the slab component to the energy spectrum, relative to the total energy:

$$r \equiv \frac{C_S}{C_S + C_2} = \frac{1}{1 + r'}, \tag{3.10}$$

where $r' = C_2/C_S$. We assume that both P_{xx} and P_{yy} satisfy the same power law with spectral index $-q$. This is not strictly correct, at least not within our dataset, but is approximately true. Equations (16) and (17) of *Bieber et al.* [1996] and the above definitions and assumptions yields the following formula for the ratio of power between components:

$$\begin{aligned}
\frac{P_{yy}(\nu)}{P_{xx}(\nu)} &= \frac{P_{(\perp)}(\nu)}{P_{(\parallel)}(\nu)} \\
&= \frac{C_S \left(\frac{2\pi\nu}{V_{SW}\cos\theta}\right)^{1-q} + C_2 \left(\frac{2q}{1+q}\right)\left(\frac{2\pi\nu}{V_{SW}\sin\theta}\right)^{1-q}}{C_S \left(\frac{2\pi\nu}{V_{SW}\cos\theta}\right)^{1-q} + C_2 \left(\frac{2}{1+q}\right)\left(\frac{2\pi\nu}{V_{SW}\sin\theta}\right)^{1-q}} \\
&= \frac{(\cos\theta)^{q-1} + r'\left(\frac{2q}{1+q}\right)(\sin\theta)^{q-1}}{(\cos\theta)^{q-1} + r'\left(\frac{2}{1+q}\right)(\sin\theta)^{q-1}}. \qquad (3.11)
\end{aligned}$$

The ratio P_{yy}/P_{xx} and the parameters $\theta = \Theta_{BV}$ and q are derivable from observations by a single spacecraft. Thus, the only unknown in equation (3.11) is r', which, in turn, gives us the slab fraction r. Note that both the solar wind speed V_{SW} and frequency ν cancel from equation (3.11), which thereby becomes independent of frequency in the relevant range.

For both slab and 2-D models, there is no power in the parallel fluctuations and $P_{zz}(\nu) = 0$. Pure slab turbulence ($r = 1$; $r' = 0$), contributes equally to P_{xx} and P_{yy} [*Bieber et al.*, 1996], whereas a pure 2-D geometry predicts that the ratio $P_{yy}(\nu)/P_{xx}(\nu)$ be equal to the power law index q. Equation (3.11) also gives the dependence on field-to-flow angle θ: as $\theta \to 0°$, $P_{yy}/P_{xx} \to 1$, and as $\theta \to 90°$, $P_{yy}/P_{xx} \to q$, assuming $r' \neq 0$ (*i.e.*, forcing a composite geometry).

Although there may be a frequency dependence as the spectrum extends further into the dissipation range, we make the simplifying assumption that there is no frequency dependence for r or r' within the frequency range of interest. For each interval in our WIND dataset we obtain one ratio P_{yy}/P_{xx} by averaging the ratio $P_{yy}(\nu)/P_{xx}(\nu)$ for each frequency ν, excluding those frequencies within a $\pm 10\%$ guard band of any harmonic of the spacecraft spin tone. An error bar was determined from the variance of the data.

We computed a P_{yy}/P_{xx} ratio for the same frequency ranges used to compute the spectral slopes of the high-frequency extent of the inertial range and the dissipation range, as discussed in chapter 2. These frequency ranges were not the

same for each interval (they depend on the break frequency of the spectrum) but typically were $\sim$ 0.01 to $\sim$ 0.3 Hz for the inertial range and $\lesssim$ 1to $\lesssim$ 2 Hz for the dissipation range.

3.5.2 Results

The results of P_{yy}/P_{xx} as a function of field-to-flow angle are shown in Figure 3.7. The curves shown are minimum χ^2 values of r, taking the spectral slopes to be constant (1.66 for the inertial range and 3.04 for the dissipation range, which are the average spectral slopes for our data). However, the χ^2 statistic of the dataset was computed using the observed value of q for each data point.

For the high-frequency inertial range described above, the minimum χ^2 of 10.87 occurs at $r = 0.11^{+0.20}_{-0.11}$. The indicated error bounds were determined from the values of r for which $\chi^2(r) = \chi^2_{\rm min} + 1$ [*Bevington*, 1969]. Note that the error bounds include $r = 0$, or a pure 2-D geometry; in fact, $\chi^2(r = 0) = 11.28$, which is still an acceptable fit. Despite the large error bars on the data points, we have 32 degrees of freedom, which implies that $r = 0.11$ is a good fit to the data. In the pure slab limit, $\chi^2(r = 1) = 23.67$, which is almost low enough to be acceptable.

For the dissipation range, the minimum χ^2 of 7.31 occurs at $r = 0.46^{+0.13}_{-0.11}$. This is a good fit, whereas $\chi^2(r = 0) = 106.0$ and $\chi^2(r = 1) = 30.72$ are not. The best fit value of $r = 0.46$ indicates that the slab fraction is increased in the dissipation range relative to the inertial range. There is a higher percentage of energy that resides in wave vectors aligned with the magnetic field in the dissipation range than in the inertial range.

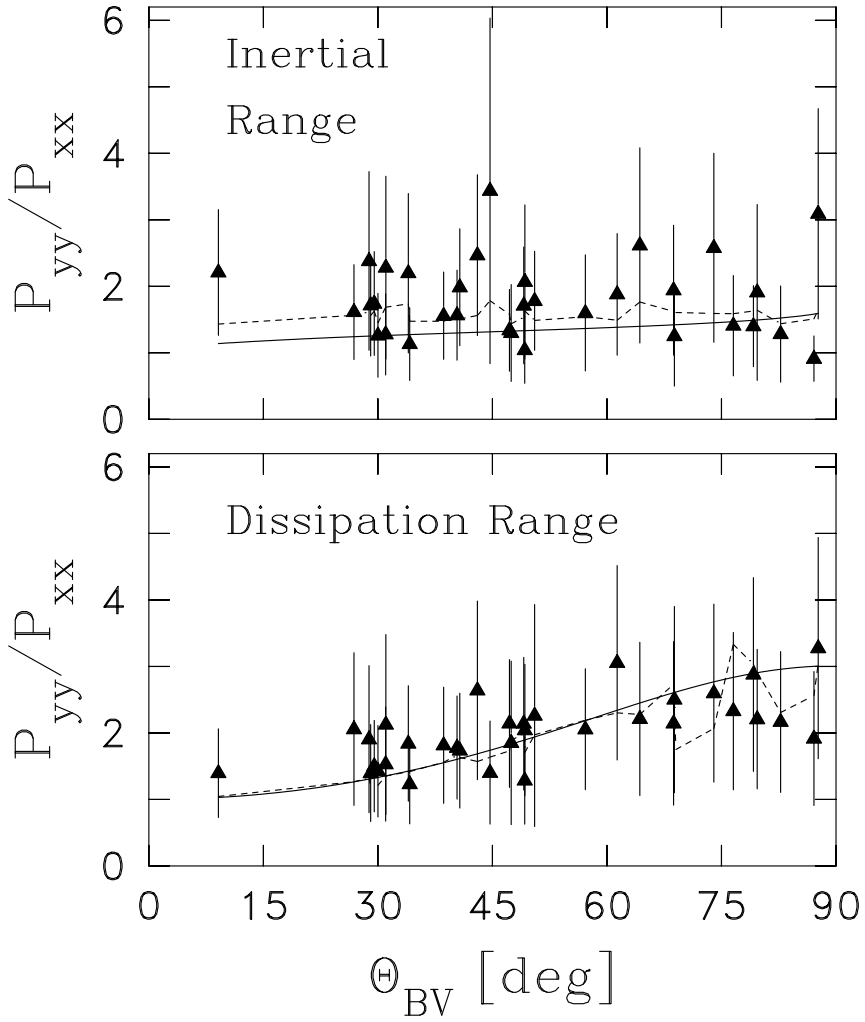

Figure 3.7: Ratio of perpendicular to parallel component spectra as a function of field-to-flow angle: (top) for the inertial range the best-fit curve is for $r = 0.11$ (11% slab component); (bottom) for the dissipation range, $r = 0.46$. Dashed curves show the best fit using individual observed power law indices, while the solid curves show the prediction of the best fit ratio using constant indices.

3.5.2.1 On the meaning of χ^2

The χ^2 statistic of a fit is the total square deviation of the fit from the data, inversely weighted by the errors in the estimates and is calculated from

$$\chi^2 = \sum_{i=1}^{N} \frac{(y^{\text{fit}}(x_i) - y_i)^2}{\sigma_i^2}, \tag{3.12}$$

where σ_i is the error bar of the ith estimate y_i. The reduced chi-squared is defined as $\chi_r^2 = \chi^2/(N-n)$, where N is the number of data points to be fit and n is the number of free parameters to the fit.

Does the "almost low enough to be acceptable" inertial range $\chi^2(r=1) = 23.67$ mean that the result is indeterminate?

It is (almost) certain that not *all* sources of error were included. Each of the data points in the top panel of Figure 3.7 has an error bar computed from the variance of the 300 or so P_{yy}/P_{xx} estimates for the inertial range frequencies. Computational errors from calculating the power spectrum, including propagation of error from individual components to the trace and those from leakage and aliasing not removed by the methods discussed in Appendix A, the error in the mean $\mathbf{B}_0$ resulting from averaging finite duration intervals, and even digitization and zero-level-offset errors from the magnetometer sensor are ignored.

As such, it can be argued that small differences in χ^2 have little physical meaning. To two significant figures in χ^2, the inertial range is as well fit by a pure 2-D geometry and a composite geometry of 11% slab waves; since their χ^2 values are half that of the pure slab wave description, the pure 2-D and composite fits are twice as good as a pure slab wave description. Neither of the pure cases is a good fit in the dissipation range.

3.6 The January 1997 Coronal Mass Ejection

The analyses of section 2.2 and this chapter were repeated on 60 contiguous one-hour intervals through the January 1997 CME. As noted in section 2.1.1, 10

hours did not give clean spectra, so the results summarized here are for 50 one-hour intervals only.

We analyzed the spectral properties for each interval in the (fixed) range of spacecraft-frame frequencies $0.02 \lesssim \nu_{sc} \lesssim 0.2$ Hz for the high-frequency end of the inertial range, and $1 < \nu_{sc} < 2$ Hz for the low-frequency end of the dissipation range.

Figure 3.8 shows the spectrum for one subinterval within the magnetic cloud. The data are rotated into the *Bieber et al.* coordinate system that we use to perform the geometry analysis of section 3.5 and described on page 59.

Note that the high frequency noise flattening is much worse in Figure 3.8 than it is in either Figure 2.1 or Figure 2.2. The signal level is so low in the parallel (P_{zz}) component that it is obscured by noise even before the spectral break at 0.77 ± 0.18 Hz. This is indicative of the result that we shall now discuss.

3.6.1 Anisotropy

Considering our variation on the *Belcher and Davis* analysis (*i.e.*, using spectral powers rather than average variances) yields inertial range anisotropies less than *Belcher and Davis* before the magnetic cloud in the solar wind: the transverse-to-parallel ratio is $(3.4 \pm 0.5) : 1$. In the sheath region, where the fluctuation levels (B_{rms}) are elevated, the fluctuation anisotropy does not change significantly and the ratio is $(4.2 \pm 1.5) : 1$. In the magnetic cloud, however, the fluctuations are highly transverse, and within the cloud the ratio is $(61.7 \pm 8.5) : 1$. Figure 3.9 shows the inertial-range anisotropy ratio for each hour-long subinterval through the whole event. The magnetic cloud, as defined by *Burlaga et al.* [1998] and shown in Figure 1.4 on page 12, is clearly identifiable from the enhanced transverse power.

In the high speed solar wind behind the magnetic cloud the anisotropy ratio is not steady, but is more consistent with the conclusions of *Belcher and Davis* [1971] at $(8.2 \pm 1.3) : 1$. It is hard to differentiate the prominence material from the high speed solar wind using the anisotropy results and Figure 3.9 alone.

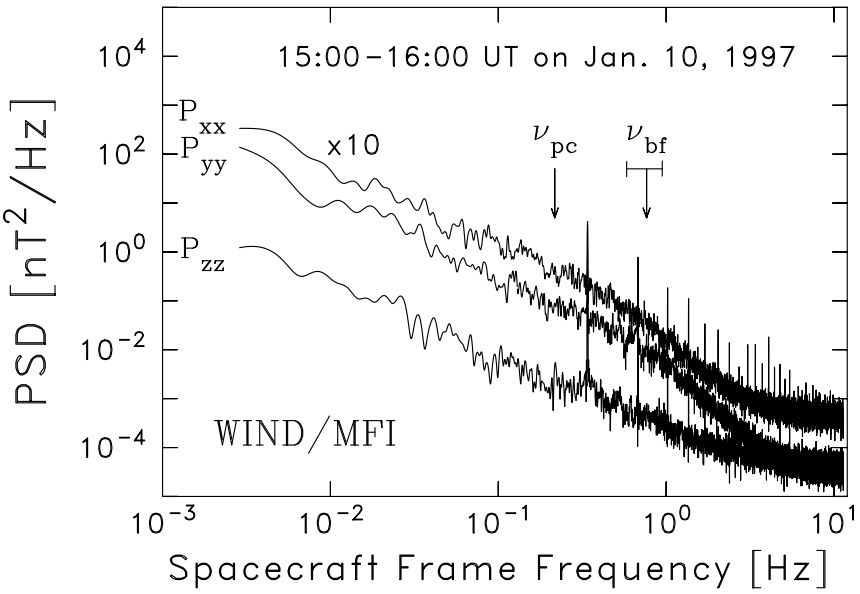

Figure 3.8: Diagonal elements of power spectral matrix computed in the mean-field coordinate system outlined in the text. Fit spectra for the combined perpendicular components, elevated for clarity, are shown with the fit spectral indexes. The x-component spectrum, P_{xx}, is multiplied by a factor of 10. The other two spectra are shown at computed power levels. The break at the dissipation scale (0.77 ± 0.18 Hz) is evident at a frequency greater than the proton gyrofrequency (0.22 Hz), as in all other intervals studied outside the magnetic cloud.

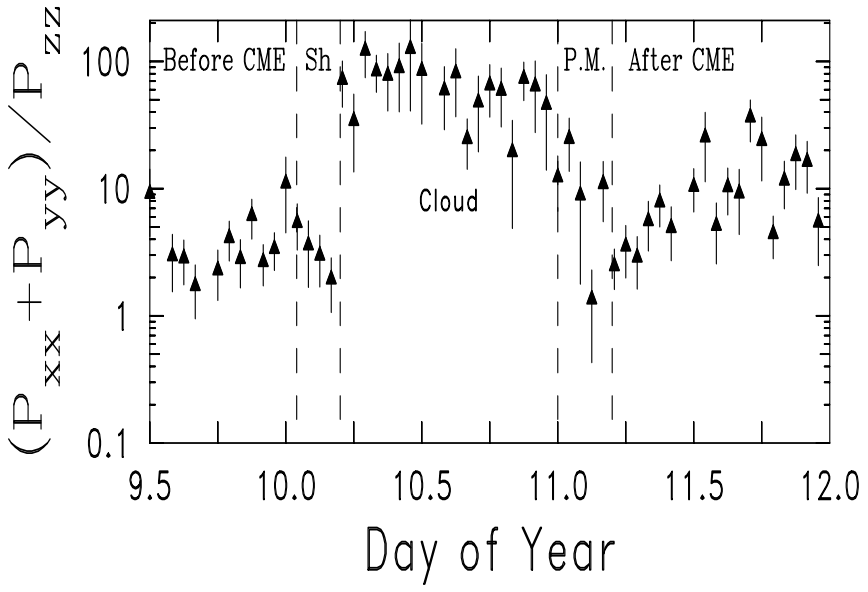

Figure 3.9: Ratio of transverse to field-aligned power in the inertial-range spectrum of magnetic fluctuations for each of the 60 hourly subintervals. Uncertainties are computed from the variation of the power ratio computed across the frequency interval. The anisotropy of the dissipation-range fluctuations are not statistically significant or reliable due to the noise level in the P_{zz} component.

3.6.2 Geometry

Figure 3.10, which is analogous to Figure 3.7 shows the results of P_{yy}/P_{xx} as a function of Θ_{BV} for the magnetic cloud. The solid curves through the data represent minimum χ^2 values of r, assuming a constant (average) value of spectral index q. Although the curves shown use the average value of the spectral indices, the χ^2 statistics of the fit were evaluated using observed values of q of each individual subinterval (dashed lines). For the high-frequency end of the inertial range (upper panel of Figure 3.10) the minimum χ^2 of 7.90 occurs at $r = 0.29 \pm 0.29$. For the dissipation range (lower panel) the minimum χ^2 of 1.35 occurs at $r = 0.04^{+0.25}_{-0.04}$. As before, the indicated error bounds were determined from the values of r for which $\chi^2(r) = \chi^2_{\rm min} + 1$ [*Bevington*, 1969].

In the undisturbed solar wind, we find that the inertial range comprises 89% 2-D turbulence and 11% slab waves and the dissipation range comprises 54% 2-D turbulence and 46% slab waves. We might postulate that in the quiet solar wind the increased dissipation range slab fraction is due to preferential dissipation of 2-D structures. This assumption is invalid in the magnetic cloud, where slab waves are completely absent. At the same time, we must reconcile the increased inertial range slab fraction (29% compared to 11%) in the magnetic cloud. Within error bounds, though, the inertial range values are the same.

We repeat the geometry fitting analysis for the slow solar wind prior to the magnetic cloud and in the high speed stream that follows it. In the 12 hours prior to the shock, the inertial range is also best described by 29% slab waves ($r = 0.29^{+0.31}_{-0.22}$ with $\chi^2_{\rm min} = 1.63$); however, the dissipation range is 91% slab waves ($r = 0.91^{+0.08}_{-0.16}$ with $\chi^2_{\rm min} = 4.87$). In the high-speed stream the inertial range is best characterized by a 34% slab component ($r = 0.34^{+0.25}_{-0.23}$ with $\chi^2_{\rm min} = 4.88$), and the dissipation range by $r = 0.32^{+0.13}_{-0.11}$ ($\chi^2_{\rm min} = 2.64$).

If we explain the increase of one geometry in the dissipation range relative to

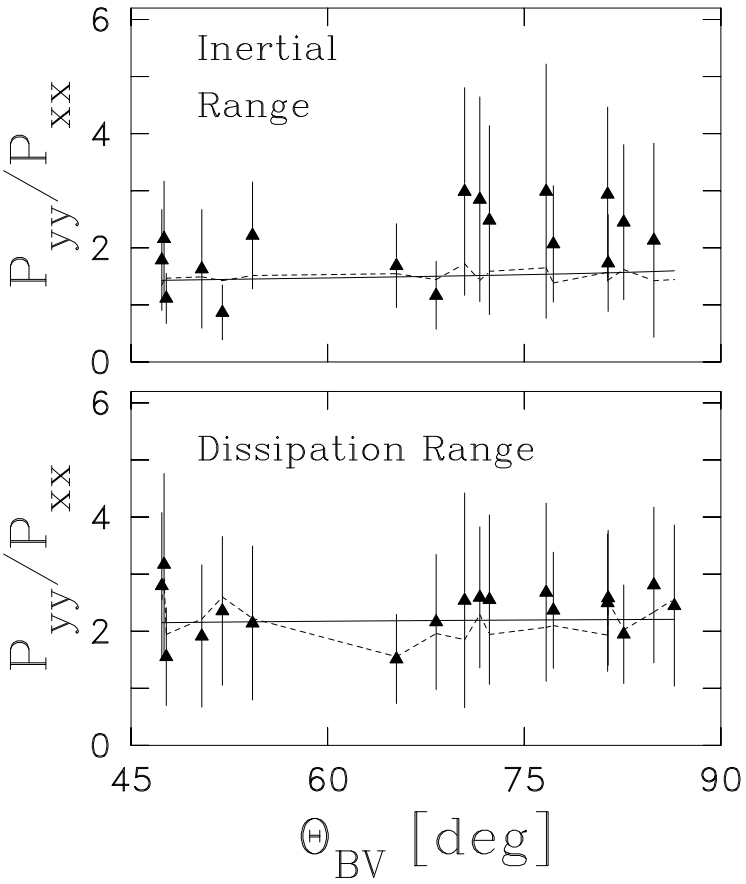

Figure 3.10: Geometry of the magnetic fluctuations in the high frequency region of the inertial range (top panel) and the dissipation range (bottom panel). In both cases the energy is composed predominantly, and almost exclusively, of 2-D fluctuations with wave vectors nearly at right angles to the ambient magnetic field. The solid curves correspond to the best-fit values of r using the average spectral index: for the inertial range, $r = 0.29$, and for the dissipation range $r = 0.04$. The dashed lines correspond to the best-fit values using the individual observed spectral indices. Uncertainties are computed from the variation of the power ratio computed over the spectral subrange in question.

the inertial range value to be due to the preferential dissipation of the other, why is the cloud's geometry in the dissipation range almost purely 2-D fluctuations while in the preceding solar wind, the fluctuations are over 90% slab waves? Consider the following. The inertial range geometry is approximately constant with 30% slab waves; it is the dissipation range geometry that varies. From the preceding solar wind to the high-speed stream to the cloud, the average proton plasma β decreases from 1.362 to 0.609 to 0.039, and the proportion of slab waves decreases from 91% to 32% to 4%. Low β favors the collapse to 2-D, as is suggested by considering the equations of reduced MHD [*Zank and Matthaeus*, 1992a], and this process may be more rapid at the smaller scales of the dissipation range.

We tried to fit geometry models to the sheath and prominence observations, but the uncertainties and χ^2 values were too large to lend confidence to the results.

3.7 Chapter Summary

In this chapter we have repeated the analyses of two inertial range studies [*Belcher and Davis*, 1971; *Bieber et al.*, 1996] and extended their results to the dissipation range using the increased capabilities of the WIND spacecraft.

The results of our investigation of magnetic fluctuations agree for the most part with those of *Belcher and Davis* [1971]: the total variances transverse to and aligned with the mean field are in a ratio 10.4 : 1 for the high-frequency end of the inertial range. In the same coordinate system $(\hat{\mathbf{B}} \times \hat{\mathbf{R}}, \hat{\mathbf{B}} \times (\hat{\mathbf{B}} \times \hat{\mathbf{R}}), \hat{\mathbf{B}})$ used by *Belcher and Davis* the ratio of geometric mean variances is 6.7 : 3.7 : 1. In the dissipation range, transverse fluctuations are less dominant, and the ratio of total transverse to parallel powers falls to 4.9 : 1, while the component-to-component ratio becomes 3.3 : 1.6 : 1.

The onset of the dissipation range, the spectral break frequency $\nu_{\rm bf}$, occurs at frequencies roughly comparable to the proton cyclotron frequency $\Omega_p/2\pi$. Together with a bias in the magnetic helicity spectrum that implies a depletion of outward

propagating Alfvén waves (observed in all but six of the 33 events used in this study), one might expect resonant cyclotron damping to explain the dissipation range. However, we find that Doppler-shifted resonant damping cannot explain the observations, and the percentage errors tend to 100% as the field-to-flow angle Θ_{BV} approaches 90°. In fact, any imposed Θ_{BV} dependence leads to a systematic error in the results.

Repeating the analyses of *Bieber et al.* [1996] in section 3.5, we find that fluctuations in the high-frequency end of the inertial range are best described as a mixture of 11% slab waves and 89% 2-D geometry with the greatest percentage of wave vectors at large angles to the mean magnetic field. In the dissipation range the fluctuations are best described by a mixture of 46% slab waves and 54% 2-D geometry. The increased slab fraction may be explained by the preferential dissipation of oblique structures. Whatever the mechanism of dissipation, it must leave a polarized magnetic helicity spectrum in the remaining slab fraction exactly as observed.

The two-component model constrains the 3-D spectrum since it is formed from only slab and 2-D components. As mentioned at the start of this chapter, *Sari and Valley* [1976] suggested that (moderately) oblique waves were necessary in addition to slab Alfvén waves, because of the existence of nonzero spectral power for the component along the mean magnetic field. Despite the fact that no direct observation of magnetosonic waves had (or still has) been made, *Sari and Valley* [1976] claimed that all the intervals they studied were consistent with $\lesssim 20\%$ of power in magnetosonic waves. It seems likely that the fully 3-D spectrum is a combination of slab, 2-D, and oblique wave vectors. This analysis suggests that the 2-D, or at least, highly oblique component dominates.

In sections 1.2 and 1.4 we discussed two paradigms for the IMF fluctuations and their implications for solar wind heating. While the results of this chapter have

not entirely ruled out the simpler paradigm of noninteracting waves, its applicability has been severely limited. The conclusion of this study is that a a significant fraction of the magnetic wave energy must necessarily reside in highly oblique waves or quasi-2-D structures. Furthermore, the onset of dissipation cannot be governed by the dynamics of ion cyclotron damping of parallel-propagating waves.

In the next two chapters we consider the possibility that obliquely propagating waves form at least a portion of the inferred 2-D component.

Chapter 4

PROPERTIES OF THE KINETIC ALFVÉN WAVE

4.1 Introduction

As discussed in section 3.3, the observed data cannot be explained solely by parallel-propagating waves. From an entirely different perspective, the examination of the data in section 3.5 suggests that a substantial fraction of the magnetic fluctuation energy in the dissipation range resides in highly oblique Fourier modes. The latter result is entirely of a geometric nature and makes no biasing assumptions as to the dynamical nature of the excitations associated with the oblique wave vectors. (Note, however, that conversion from frequency f to wave vector k using a single spacecraft requires use of the "frozen-in assumption," which requires that the characteristic speed of the fluctuations be much smaller than the solar wind speed.) In any event, there remains the challenge of finding a dynamical model that might adequately describe these highly transverse, nonslab fluctuations, thus forming a physical basis for understanding the couplings between fluid and kinetic scales in the dissipation range.

Consider the possibility that obliquely propagating waves form at least a portion of the inferred 2-D component. There are three wave modes for low-frequency, obliquely propagating electromagnetic waves:

1. the fast magnetosonic wave;

2. the shear Alfvén wave; and

3. the slow-mode wave.

Both the fast magnetosonic wave and the slow-mode wave are heavily damped in a high-β plasma, regardless of wavelength [*Barnes*, 1979]. However, WIND data studied herein, as well as those reported elsewhere, indicate the presence of a spectral breakpoint at scales near those of ion gyromotion, which we associate with the dissipation processes. In this interpretation it is highly unlikely that the fast- and slow-mode waves can provide an adequate explanation of the observed data. The shear Alfvén wave becomes the kinetic Alfvén wave which develops a substantial parallel electric field component when the wavenumber k increases such that $k_\perp \rho_i \sim 1$, where $\rho_i = V_A/\Omega_p$ is the ion inertial scale [*Hasegawa and Sato*, 1989; *Stix*, 1992]. (In a $\beta \sim 1$ plasma, the condition for the onset of the parallel electric field may be written as $k_\perp R_L \sim 1$, where $R_L = v_{th}/\Omega_p$ is the proton Larmor radius.) In this regime, the kinetic Alfvén wave is highly dispersive, and the real part of the wave frequency asymptotically approaches the ion cyclotron frequency. Electron Landau damping becomes important because of the presence of the parallel electric field component, and ion cyclotron damping can also play a significant role in the damping process if $\omega \sim \Omega_p$.

The onset of substantial damping appears to scale with the Larmor radius, as is suggested in Figure 4.1, which shows two representations of the relationship between the Larmor radius for thermal protons and the dissipation wavenumber $k_{diss} \equiv 2\pi\nu_{bf}/V_{SW}$. Dissipation sets in when k^{-1} scales are of the order of the proton Larmor radius, without regard for Θ_{BV}. A slab geometry would introduce an extra factor of $\cos\Theta_{BV}$ into the dependence of k_{diss} on R_L, which is manifestly absent in Figure 4.1. We have already seen in Figure 3.5 on page 54 that the particular choice of a slab geometry fails to organize the observations. On the other hand, Figure 4.1 seems to suggest that there are always fluctuations that project onto V_{SW} as (some multiple of) R_L to mark the onset of dissipation. The

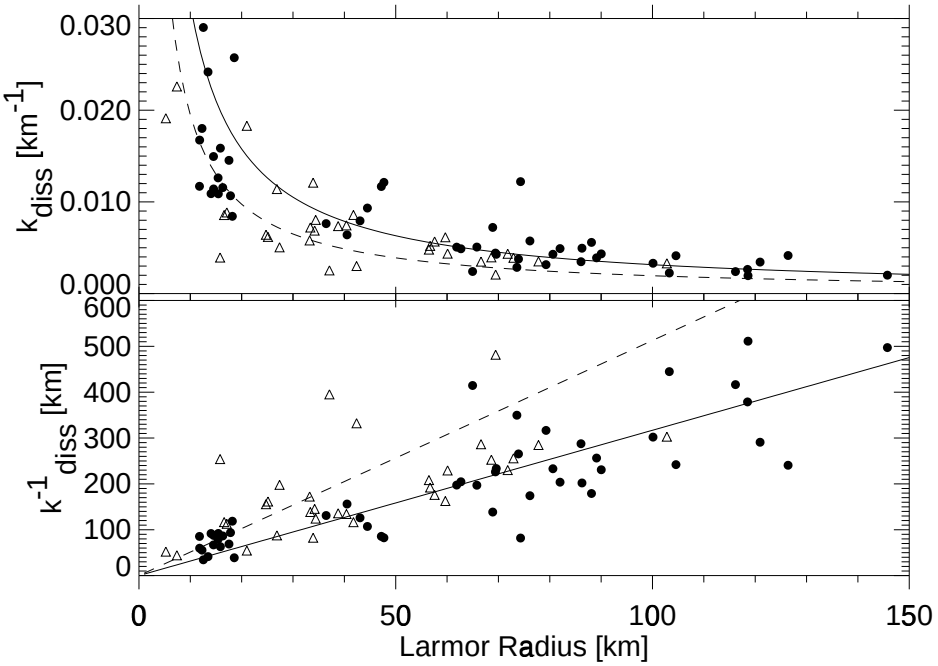

Figure 4.1: Two scatterplots showing the inverse relationship between the observed frequency marking the onset of the dissipation range and the Larmor radius for a thermal proton. The solid line in each case corresponds to the best-fit straight line of the bottom panel, namely $k_{diss}^{-1} = (3.172 \pm 0.152)R_L$, and the dashed curve corresponds to the best-fit hyperbola of the top panel, $k_{diss} = (0.195 \pm 0.012)R_L^{-1}$. Observations in the quiet solar wind dataset are shown as triangles, and those from the January 1997 ICME are represented by circles.

fluctuations contain a component besides just an ensemble of parallel-propagating ("slab") Alfvén waves. What is needed, according to Figure 4.1, is a more nearly isotropic dissipation mechanism that is associated, at least in part, with cyclotron resonance.

The damping of kinetic Alfvén waves is one such possibility. The advantages of an explanation based upon kinetic Alfvén waves are that:

1. they possess wave vectors at large angles to the mean magnetic field, which is in general agreement with the conclusions of chapter 3;

2. they provide both cyclotron resonant dissipation and dissipation via the generation of parallel electric fields at comparable wavenumbers; and

3. the two distinct dissipation mechanisms provide separate, coincident mechanisms for heating both background ions and electrons.

In this chapter we shall pursue this suggestion with both a general examination of the damping of obliquely propagating kinetic Alfvén waves and an additional examination of the observations. We explore the damping rates of kinetic Alfvén waves under a wide range of interplanetary conditions using numerical solutions of the linearized Maxwell-Vlasov equations and demonstrate that these waves display the nearly isotropic dissipation properties inferred.

Using the results of this chapter, in the next chapter we present a simple model to predict the onset of the dissipation range, broadly following the method of section 3.3.2 using the numerical Maxwell-Vlasov solutions, and compare these predictions to the observations.

The kinetic Alfvén wave (KAW) can be viewed as a coupling of the ion-acoustic mode ($\omega = \pm c_s k$) and the Alfvén wave [see, *e.g.*, *Hasegawa*, 1976; *Lysak and Lotko*, 1996; *Hollweg*, 1999]. It was introduced by Hasegawa with the inclusion of finite Larmor radius effects in the MHD equations. It also experiences both electron

and ion Landau damping through its coupling to the electrostatic mode [*Hasegawa and Uberoi*, 1982]. It produces compressive (parallel) magnetic field fluctuations and has a parallel electric field component. Unlike the magnetosonic mode considered by *Barnes* [1966], the kinetic Alfvén wave experiences Landau damping only at scales comparable to the ion Larmor radius.

Kinetic Alfvén waves have been connected to a wide variety of geophysical processes from the ionosphere to the solar corona [for an exhaustive list, see *Hollweg*, 1999]. There are a number of reasons why kinetic Alfvén waves provide an interesting model for our problem of solar wind IMF fluctuations.

At low wavenumbers, for instance, they are mostly transverse, with a minimum variance direction close to $\mathbf{B}_0$ and are thus not inconsistent with the observations of *Belcher and Davis* [1971], even though they are not propagating parallel to $\mathbf{B}_0$.

The object of the rest of this chapter is to analyse in detail the properties of the KAW in association with the dissipation and damping of IMF fluctuations.

4.2 Analytic Approximations to the Kinetic Alfvén Wave Dispersion Relation

Even though numerical calculations are the most accurate method of determining the full KAW dispersion relation, we first consider its derivation, using analytic approximations, for the purposes of demonstrating the mode couplings. Here we follow the derivation of *Hasegawa and Sato* [1989].

The parallel electric field component, generated by the finite Larmor radius effect, requires use of the Vlasov equations to properly account for dissipation due to Landau damping. It also allows the Alfvén wave to couple with the ion acoustic wave. The compressional component of the magnetic field perturbation, B_z, can be assumed much smaller than the transverse components. This allows us to use a

scalar potential, ϕ, to represent the transverse components of the electric field, $\mathbf{E}_\perp$,

$$\mathbf{E}_\perp = -\boldsymbol{\nabla}_\perp \phi \tag{4.1}$$

because then B_z becomes zero. To represent the parallel component of the electric field, we must use a different potential, so that the transverse components of $\boldsymbol{\nabla} \times \mathbf{E}$ are not zero:

$$E_z = -\frac{\partial \psi}{\partial z} \tag{4.2}$$

The appropriate field equations are Poisson's equation,

$$\nabla_\perp^2 \phi + \frac{\partial^2 \psi}{\partial z^2} = 4\pi e \left[n^{(i)} - n^{(e)} \right] \approx 0 \tag{4.3}$$

and the z component of Ampère's law,

$$\frac{\partial}{\partial z} \nabla_\perp^2 (\phi - \psi) = 4\pi \frac{\partial}{\partial t} \left[J_z^{(i)} - J^{(e)_z} \right]. \tag{4.4}$$

The quantities $n^{(i)}$, $n^{(e)}$, $\mathbf{J}^{(i)}$ and $\mathbf{J}^{(e)}$ are obtained from the linearized Vlasov equation for each species. For electrons, the linearized distribution function $f_{\mathbf{k}}^{(e)}$ becomes, assuming $k_\perp \rho_e \simeq 0$ and $\omega \ll \Omega_e$, the electron cyclotron frequency,

$$f_{\mathbf{k}}^{(e)}(\mathbf{v}) = -\frac{e}{m_e} \frac{k_\parallel \psi_{\mathbf{k}}}{k_\parallel v_\parallel - \omega} \frac{\partial f_0^{(e)}}{\partial v_\parallel}. \tag{4.5}$$

For ions, by retaining the finite Larmor radius effect,

$$\begin{aligned} f_{\mathbf{k}}^{(i)}(\mathbf{v}) &= f_{\mathbf{k}}^{(i)}(v_\perp, \theta, v_\parallel) \\ &= -\frac{e}{m_e} \sum_{n=-\infty}^{\infty} \sum_{m=-\infty}^{\infty} \frac{e^{i(n-m)\theta}}{\omega - k_\parallel v_\parallel - n\Omega_p} J_n \left(\frac{k_\perp v_\perp}{\Omega_p} \right) J_m \left(\frac{k_\perp v_\perp}{\Omega_p} \right) \\ &\times \left\{ k_\perp \phi_{\mathbf{k}} \left[\left(1 - \frac{k_\parallel v_\parallel}{\omega} \right) \frac{n\Omega_p}{k_\perp v_\perp} \frac{\partial f_0^{(i)}}{\partial v_\perp} + \frac{k_\perp}{k_\parallel} \frac{n\Omega_p}{\omega} \frac{\partial f_0^{(i)}}{\partial v_\parallel} \right] \right. \\ &\left. + k_\parallel \psi_{\mathbf{k}} \left[\frac{v_\parallel}{v_\perp} \frac{n\Omega_p}{\omega} \frac{\partial f_0^{(i)}}{\partial v_\perp} + \left(1 - \frac{n\Omega_p}{\omega} \right) \frac{\partial f_0^{(i)}}{\partial v_\parallel} \right] \right\}, \end{aligned} \tag{4.6}$$

where θ is the phase angle of the Larmor motion, and the J's are Bessel functions of the first kind. The Fourier amplitudes of the charge density and the current density perturbation are obtained from

$$q^{(j)} n_{\mathbf{k}}^{(j)} = q^{(j)} n_0 \int f_{\mathbf{k}}^{(j)} d\mathbf{v} \tag{4.7}$$

$$\mathbf{J}_{\mathbf{k}}^{(j)} = q^{(j)} n_0 \int \mathbf{v} f_{\mathbf{k}}^{(j)} d\mathbf{v} \tag{4.8}$$

where j can be either i or e.

If $\beta > m_e/m_i$, the electron thermal speed will be larger than the Alfvén speed and the resultant charge and current density perturbations may be reduced to

$$4\pi e n_{\mathbf{k}}^{(i)} = -\frac{\omega_{pi}^2}{v_{th,i}^2}\left[1 - I_0(\lambda_i)e^{-\lambda_i}\right]\phi_{\mathbf{k}} + \frac{\omega_{pi}^2 k_\parallel^2}{\omega^2} I_0(\lambda_i)e^{-\lambda_i}(1 - i\delta_i)\psi_{\mathbf{k}} \tag{4.9}$$

$$4\pi e n_{\mathbf{k}}^{(e)} = \frac{\omega_{pe}^2}{v_{th,e}^2}(1 + i\delta_e)\psi_{\mathbf{k}} \tag{4.10}$$

$$4\pi J_{z\mathbf{k}}^{(i)} = \frac{\omega_{pi}^2}{c^2}\frac{k_\parallel}{\omega} I_0(\lambda_i)e^{-\lambda_i}(1 - i\delta_i)\psi_{\mathbf{k}} \tag{4.11}$$

$$4\pi J_{z\mathbf{k}}^{(e)} = -\frac{\omega_{pe}^2}{v_{th,e}^2}\frac{\omega}{c^2 k_\parallel}(1 + i\delta_e)\psi_{\mathbf{k}} \tag{4.12}$$

where $\lambda_i = k_\perp^2 \rho_i^2$, $I_0(\lambda_i)$ is the modified Bessel function of the first kind,[1] $v_{th,i}$ and $v_{th,e}$ are the ion and electron thermal speeds, respectively, and δ_i and δ_e are the fractional Landau damping rates,

$$\delta_i = 2\sqrt{\pi}\beta_i^{-3/2}\exp(-\beta_i^{-1}) \tag{4.13}$$

$$\delta_e = \sqrt{\pi}\beta_i^{-1/2}\left(\frac{T_i}{T_e}\right)^{1/2}\left(\frac{m_i}{m_e}\right)^{-1/2}. \tag{4.14}$$

[1] Modified Bessel functions are simply Bessel functions of pure imaginary argument. They are defined by $I_\nu(x) = i^{-\nu}J_\nu(ix)$, and are real functions for real x and ν. (All odd powers of x have vanishing coefficients in the power series expansion of $J_\nu(x)$.)

The dispersion relation can be obtained by substituting equations (4.10)–(4.12) into equations (4.3) and (4.4). If we ignore the damping,

$$\left(I_0(\lambda_i)e^{-\lambda_i} - \frac{\omega^2}{k_\parallel^2 c_s^2}\right)\left[1 - \frac{\omega^2}{k_\parallel^2 V_A^2}\frac{1}{\lambda_i}\left(1 - I_0(\lambda_i)e^{-\lambda_i}\right)\right] = \frac{\omega^2}{k_\parallel^2 v_{th,i}^2}\left(1 - I_0(\lambda_i)e^{-\lambda_i}\right), \tag{4.15}$$

where $c_s = (k_B T_e/m_i)^{1/2}$ is the ion sound speed with electron temperature, and V_A is the Alfvén speed. Subscript symbols $\perp$ and $\parallel$ refer to the directions perpendicular and parallel to the mean magnetic field, respectively.

Equation (4.15) neglects damping, *i.e.*, ω is only the real part of the frequency. It should be noted that for a high-β plasma like the solar wind ($\beta \sim \mathcal{O}(1)$), the correction to equation (4.15), due to the neglected damping and the other approximations used above, can be substantial [*H. K. Wong*, private communication, 1998]. Nevertheless, equation (4.15) clearly shows the coupling of the ion acoustic mode (zero of first parenthesis) and the Alfvén wave (zero of square brackets). For small values of λ_i, $I_0(\lambda_i)e^{-\lambda_i} \simeq 1$, so the right-hand side of equation (4.15) tends to zero, the first parenthesis tends to $(1 - \omega^2/k_\parallel^2 c_s^2)$, which is the ion acoustic dispersion relation. Similarly, the Alfvén bracket $[\ldots]$ tends to $1 - \omega^2/k_\parallel^2 V_A^2$.

In a low-β plasma, $c_s^2 \ll V_A^2$, the coupling is weak and the dispersion relation for the kinetic Alfvén wave becomes

$$\frac{\omega^2}{k_\parallel^2 V_A^2} = \frac{\lambda_i}{1 - I_0(\lambda_i)e^{-\lambda_i}} + \frac{T_e}{T_i}\lambda_i. \tag{4.16}$$

Furthermore, if $\lambda_i \ll 1$, the dispersion relation reduces to

$$\omega^2 = k_\parallel^2 V_A^2\left[1 + k_\perp^2 \rho_i^2\left(\frac{3}{4} + \frac{T_e}{T_i}\right)\right]. \tag{4.17}$$

Equations (4.15)–(4.17) are all from *Hasegawa and Sato* [1989].

4.3 Methods of Numerical Calculation of Wave Dispersion Relations

In cgs-Gaussian notation, Maxwell's equations are

$$\boldsymbol{\nabla} \cdot \mathbf{E} \;=\; 4\pi\rho \tag{4.18}$$

$$\boldsymbol{\nabla} \cdot \mathbf{B} = 0 \tag{4.19}$$

$$\boldsymbol{\nabla} \times \mathbf{E} = -\frac{1}{c}\frac{\partial \mathbf{B}}{\partial t} \tag{4.20}$$

$$\boldsymbol{\nabla} \times \mathbf{B} = \frac{4\pi}{c}\mathbf{j} + \frac{1}{c}\frac{\partial \mathbf{E}}{\partial t}. \tag{4.21}$$

In what follows, all first-order fluctuations are assumed to vary as $\exp[i(\mathbf{k}\cdot\mathbf{x} - \omega t)]$. It is assumed that the wave vector $\mathbf{k}$ is real; ω may be complex. After Fourier transforming equations (4.21) and (4.21) in both time and space, we obtain the homogeneous plasma wave equation

$$\frac{c^2}{\omega^2}\mathbf{k} \times (\mathbf{k} \times \delta\mathbf{E}) + \boldsymbol{\epsilon} \cdot \delta\mathbf{E} = 0, \tag{4.22}$$

which may be written

$$\mathbf{D} \cdot \delta\mathbf{E} = 0, \tag{4.23}$$

where $\mathbf{D}(\mathbf{k}, \omega)$ is the *dielectric* tensor.

The condition for a nontrivial solution of the vector wave equation (4.23) is that the determinant of the 3×3 matrix be zero (cf. equation (1.5)). This condition gives the dispersion relation that determines ω as a function of $\mathbf{k}$. As pointed out by *Stix* [1992], the dielectric tensor is *additive* in its components, whereas a dispersion relation is not. One cannot add a "dispersion relation for electrons" to a "dispersion relation for ions" to obtain the dispersion relation for a neutral plasma. But one can so add together the contributions to the dielectric tensor, not just from electrons and all ion species present, but, for example, just the high-energy tail of a velocity distribution and trace its identifiable effect on the waves. This is precisely what will be done in section 4.5, where the ion contributions to Landau damping are determined by lowering β_e to very small values, effectively removing all electron contributions.

Contained in the dielectric tensor are the magnetic susceptibility and conductivity of the plasma, which may be derived from the distribution functions $f_\alpha(\mathbf{x}, \mathbf{v}, t)$ and the equation of motion, or Vlasov equation

$$\frac{\partial f_\alpha}{\partial t} + \mathbf{v} \cdot \frac{\partial f_\alpha}{\partial \mathbf{x}} + \frac{q}{m}\left(\mathbf{E} + \frac{\mathbf{v} \times \mathbf{B}}{c}\right) \cdot \frac{\partial f_\alpha}{\partial \mathbf{v}}. \tag{4.24}$$

Goldstein et al. [1985] give the dielectric tensor as

$$\begin{aligned} D_{ij}(\mathbf{k}, \omega) &= \left(1 + \frac{k^2 c^2}{\omega^2}\right)\delta_{ij} + \frac{c^2}{\omega^2} k_i k_j \\ &+ 2\pi \sum_\alpha \frac{\omega_\alpha^2}{\omega^2} \int_{-\infty}^{\infty} dv_\parallel \int_0^\infty dv_\perp \, v_\parallel \left[v_\perp \frac{\partial f_\alpha}{\partial v_\parallel} - v_\parallel \frac{\partial f_\alpha}{\partial v_\perp} \right] \hat{\mathbf{z}}\hat{\mathbf{z}} \\ &- 2\pi \sum_\alpha \sum_{n=-\infty}^{\infty} \frac{\omega_\alpha^2}{\omega^2} \int_{-\infty}^{\infty} dv_\parallel \int_0^\infty dv_\perp \frac{(T_\alpha^{(n)})_{ij}}{k_\parallel v_\parallel + n\Omega_\alpha - \omega} \\ &\times \left\{ \omega \frac{\partial f_\alpha}{\partial v_\perp} + k_\parallel \left[v_\perp \frac{\partial f_\alpha}{\partial v_\parallel} - v_\parallel \frac{\partial f_\alpha}{\partial v_\perp} \right] \right\}, \end{aligned} \tag{4.25}$$

where the background field $\mathbf{B}_0$ is assumed to be in the $\hat{\mathbf{z}}$ direction, ω_α and Ω_α are the plasma frequency and cyclotron frequency, respectively, of the αth species, and $\mathbf{T}_\alpha^{(n)}$ is defined by

$$\mathbf{T}_\alpha^{(n)} = \begin{pmatrix} \frac{n^2\Omega_\alpha^2}{k_\perp^2} J_n^2 & \frac{in\Omega_\alpha}{k_\perp} v_\perp J_n J_n' & \frac{n\Omega_\alpha}{k_\perp} v_\parallel J_n^2 \\ \frac{-in\Omega_\alpha}{k_\perp} v_\perp J_n J_n' & v_\perp^2 (J_n')^2 & -iv_\parallel v_\perp J_n J_n' \\ \frac{n\Omega_\alpha}{k_\perp} v_\parallel J_n^2 & iv_\parallel v_\perp J_n J_n' & v_\parallel^2 J_n^2 \end{pmatrix}$$

where $J_n = J_n(k_\perp v_\perp / \Omega_\alpha)$ is the Bessel function of order n and J_n' is its derivative.

If f_α is a Maxwellian, then the integrals in equation (4.25) may be done analytically. We shall limit ourselves to a single Maxwellian,

$$f_\alpha = \frac{1}{\pi^{3/2} v_{th,\alpha}^3} \exp\left[-\left(\frac{v_\perp^2}{v_{th,\alpha}^2} + \frac{v_\parallel^2}{v_{th,\alpha}^2} \right) \right], \tag{4.26}$$

although each component may have a temperature anisotropy ($T_\parallel \neq T_\perp$), a streaming velocity parallel to the background magnetic field, or both, and still be analytically integrable.

The integration over $v_\perp$ is done first, using the following Bessel function identities:

$$\begin{aligned}
\int_0^\infty dx\, x J_n^2(x)\, \exp(-x^2/2\lambda) &= \lambda \Lambda_n(\lambda) \\
\int_0^\infty dx\, x^2 J_n(x) J_n'(x)\, \exp(-x^2/2\lambda) &= \lambda^2 \Lambda_n'(\lambda) \\
\int_0^\infty dx\, x^3 [J_n'(x)]^2\, \exp(-x^2/2\lambda) &= n^2 \lambda \Lambda_n(\lambda) - 2\lambda^3 \Lambda_n'(\lambda)
\end{aligned}$$

where $\Lambda_n(\lambda) = e^{-\lambda} I_n(\lambda)$ and $I_n(\lambda)$ is the modified Bessel function, as before. Λ_n' is the derivative with respect to λ, which may be written

$$\Lambda_n'(\lambda) = -\Lambda_n(\lambda) + \tfrac{1}{2}\left[\Lambda_{n-1}(\lambda) + \Lambda_{n+1}(\lambda)\right]. \tag{4.27}$$

The integrals over $v_\parallel$ can be written in terms of the Plasma Dispersion function, which satisfies the differential equation

$$Z'(\xi_\alpha) = -2\left[1 + \xi_\alpha Z(\xi_\alpha)\right]. \tag{4.28}$$

and is essentially the Hilbert Transform of a Gaussian

$$Z(\xi_\alpha) = \pi^{-1/2} \int_{-\infty}^{\infty} \frac{e^{-x^2}}{x - \xi_\alpha} dx, \tag{4.29}$$

where

$$\xi_\alpha = \frac{\omega - n\Omega_\alpha}{k_\parallel v_{th,\alpha}}. \tag{4.30}$$

As previously explained, the dispersion tensor can be written as the sum over each component's contribution. After some algebra, each component of the dispersion tensor can be written

$$D_{ij,\alpha}(\mathbf{k},\omega) = \begin{pmatrix} 1 - \dfrac{k_\parallel^2 c^2}{\omega^2} + Q_{xx,\alpha} & Q_{xy,\alpha} & \dfrac{k_\perp k_\parallel c^2}{\omega^2} + Q_{xz,\alpha} \\ Q_{yx,\alpha} & 1 - \dfrac{k^2 c^2}{\omega^2} + Q_{yy,\alpha} & Q_{yz,\alpha} \\ \dfrac{k_\perp k_\parallel c^2}{\omega^2} + Q_{zx,\alpha} & Q_{yz,\alpha} & 1 - \dfrac{k_\perp^2 c^2}{\omega^2} + Q_{zz,\alpha} \end{pmatrix}, \quad (4.31)$$

where the $Q_{ij,\alpha}$ are defined by

$$\begin{aligned}
Q_{xx,\alpha} &= 2\,\frac{\omega_\alpha^2}{\omega^2}\sum_n \Lambda_n \frac{n^2\Omega_\alpha^2}{k_\perp^2 v_{th,\alpha}^2}\frac{\omega}{k_\parallel v_{th,\alpha}} Z(\xi_\alpha) \\
Q_{xy,\alpha} &= 2i\,\frac{\omega_\alpha^2}{\omega^2}\sum_n \Lambda_n' \frac{\lambda}{2}\frac{\omega}{k_\parallel v_{th,\alpha}} Z(\xi_\alpha) \\
Q_{xz,\alpha} &= 2\,\frac{\omega_\alpha^2}{\omega^2}\sum_n \Lambda_n \frac{n\Omega_\alpha}{k_\perp v_{th,\alpha}}\frac{\omega}{k_\parallel v_{th,\alpha}} Z(\xi_\alpha) \\
Q_{yx,\alpha} &= -Q_{xy,\alpha} \\
Q_{yy,\alpha} &= 2\,\frac{\omega_\alpha^2}{\omega^2}\sum_n \frac{\Omega_\alpha^2}{k_\perp^2 v_{th,\alpha}^2}\left(n^2\Lambda_n - 2\lambda^2\Lambda_n'\right)\frac{\omega}{k_\parallel v_{th,\alpha}} Z(\xi_\alpha) \\
Q_{yz,\alpha} &= -2i\,\frac{\omega_\alpha^2}{\omega^2}\sum_n \frac{\lambda\Omega_\alpha}{k_\perp v_{th,\alpha}}\Lambda_n'\xi_\alpha\frac{\omega}{k_\parallel v_{th,\alpha}} Z(\xi_\alpha) \\
Q_{zx,\alpha} &= Q_{xz,\alpha} \\
Q_{zy,\alpha} &= -Q_{yz,\alpha} \\
Q_{zz,\alpha} &= 2\,\frac{\omega_\alpha^2}{\omega^2}\sum_n \Lambda_n \frac{\omega}{k_\parallel v_{th,\alpha}}\left[\frac{\omega}{k_\parallel v_{th,\alpha}} + \xi_\alpha^2 Z(\xi_\alpha)\right].
\end{aligned} \quad (4.32)$$

The final forms of **Q** and **D** above are not unique, since

$$\sum_{n=-\infty}^{\infty} nI_n = \sum_{n=-\infty}^{\infty} (I_n - I_n') = 0,$$

so certain terms can be added and subtracted if they do not depend on n. From this fact, and equation (4.28), some authors [*e.g.*, *Chen*, 1984; *Swanson*, 1989] prefer to recast Q_{xz}, Q_{yz} and Q_{zz}, and thus the corresponding elements of **D**, in terms of $Z'(\xi_\alpha)$.

4.4 Damping Mechanisms

Various types of damping are contained within the expressions for the susceptibility and dielectric tensors above: ion cyclotron, ion Landau and electron Landau damping, and transit-time magnetic damping. Landau damping and transit-time damping are both part of the contribution from the $n = 0$ term of the dielectric tensor [*Stix*, 1992]. The $n = 0$ contribution can be either resonant or nonresonant in nature, depending upon the underlying particle and field parameters.

4.4.1 Landau Damping

Landau damping occurs in the absence of particle collisions. It is the interaction between a distribution of particles and the electric field of a propagating wave. Calculating the damping rate analytically is tedious and demanding, involving contour integration in the complex plane. However, the following offers a general, nonmathematical, explanation of the effect.

We may write the condition for Landau resonance as $v_{\parallel} = \omega/k$. Particles which are close to resonance are the ones which can exchange energy with the wave most efficiently. First consider particles far from resonance, which are moving rapidly in the wave frame, and so experience a rapidly oscillating electric field. Thus they undergo alternate accelerations and decelerations, but the average effect is very small. However, particles close to resonance are almost at rest in this frame. They therefore experience a roughly constant electric field, and will undergo a large acceleration (if $qE > 0$) or deceleration (if $qE < 0$).

The fact that the particle undergoes a large acceleration or deceleration means that its velocity changes. It moves away from resonance, and the large acceleration or deceleration will cease. The magnitude of the effect on any individual particle will depend on how long it stays close to resonance.

Consider particles that are moving slightly faster than the wave. Those that are accelerated move away from resonance, but those that are decelerated move

closer to resonance. These particles therefore stay close to resonance for longer, and the effect on them is larger. Averaging over the whole wave, particles which are moving slightly faster than the wave are, on average, slowed down. Similarly, those particles which are moving slightly slower than the wave are, on average, speeded up.

The Maxwellian distribution function is a decreasing function of $\mathbf{v}$ for all v. So, no matter what phase velocity the wave has, there will always be more particles moving slightly slower than the wave than slightly faster. Overall, therefore, the particle kinetic energy increases. This energy comes from the electric field of the wave, which is therefore damped.

4.4.2 Cyclotron Damping

Landau damping exists even in the absence of a magnetic field permeating the plasma in question. A magnetic field changes particle trajectories into helices spiralling around the magnetic field lines. Resonances in the individual *perpendicular* particle motions now arise at all multiples of the cyclotron frequency, the strongest of which occurs at the fundamental cyclotron frequency. This set of resonances may be contrasted with the single resonance at zero frequency for parallel oscillation (*i.e.*, Landau damping). The cyclotron resonances give rise to damping which is akin to Landau damping.

When a particle moving along $\mathbf{B}_0$ in a wave with finite $k_\parallel$ has the right velocity, it "sees" a Doppler-shifted frequency $\omega - k_\parallel v_\parallel = \pm n\Omega_p$ and is therefore subject to continuous acceleration by the electric field of the wave. Those particles with the "correct" phase relative to $\mathbf{E}_\perp$ will gain energy; those with the "wrong" phase will lose energy. Since the energy change is force times distance, the faster accelerated particles will gain more energy per unit time than the slower decelerated particles lose. There is, therefore, a net gain of energy by the particles, on average, at the expense of wave energy and the wave is damped. This mechanism differs from

Landau damping because the energy gained is in the direction perpendicular to $\mathbf{B}_0$, and hence perpendicular to the velocity component that brought it into resonance.

Neglecting any motion parallel to $\mathbf{B}_0$, we may write the equation of motion as

$$\begin{aligned}\frac{dW_\perp}{dt} &= \frac{d}{dt}\frac{mv_\perp^2}{2} \\ &= m\mathbf{v}_\perp \cdot \frac{d\mathbf{v}_\perp}{dt} \\ &= q\mathbf{v}_\perp \cdot \left[\mathbf{E}_\perp + \frac{\mathbf{v}\times\mathbf{B}}{c}\right]. \end{aligned} \tag{4.33}$$

Further neglecting changes in the orbit due to the $\mathbf{E}$ field, we may write $\mathbf{E} = \hat{\mathbf{z}}\tilde{E}\cos(k_\perp z - \omega t)$, $z = \rho_L \sin(\Omega t + \phi)$. Then

$$\begin{aligned}\frac{dW_\perp}{dt} &= q\tilde{E}\Omega\rho_L \cos\left[k_\perp \rho_L \sin(\Omega t+\phi) - \omega t\right]\cos(\Omega t+\phi) \\ &= q\tilde{E}\Omega\rho_L \Re\left[\sum_{n=-\infty}^{\infty} J_n(k_\perp\rho_L) e^{in(\Omega t+\phi)-i\omega t}\right]\Re\left[e^{i(\Omega t+\phi)}\right], \end{aligned} \tag{4.34}$$

where we have used the identity [*Montgomery and Tidman*, 1964]

$$e^{-iz\sin(\Omega t+\phi)} = \sum_{m=-\infty}^{\infty} e^{-im(\Omega t+\phi)} J_m(z).$$

It is seen from equation (4.34) that increases in $W_\perp$ will occur at $\omega = (n \pm 1)\Omega$ for all n at rates proportional to $\rho_L J_n(k_\perp\rho_L)\cos[(n\pm 1)\phi]$.

4.4.3 Transit-Time Damping

Landau damping and transit-time magnetic damping are both wave-particle interactions that may be identified with the $n = 0$ terms in the susceptibility tensors. Nevertheless, they are two distinct physical processes. Transit-time damping comes from the interaction of the adiabatic magnetic moment of a charged particle, $\mu = mv_\perp^2/2B_0$, with the parallel gradient of the magnetic field. The equation of motion is

$$m\frac{dv_\parallel}{dt} = -\mu\hat{\mathbf{B}}\cdot\boldsymbol{\nabla}B. \tag{4.35}$$

The equation is identical to the electrostatic force equation (Coulomb's Law) with μ replacing the charge and $B = |\mathbf{B}|$ the electric potential. The damping that results from this magnetic interaction is thus the magnetic analogue of Landau damping. Landau damping is due to the interaction of the particles with the wave electric fields, and is mainly electrostatic, whereas transit-time damping is due to the interaction of the particles with the parallel magnetic field δB_z (the compressible perturbation) and is electromagnetic in nature.

Finally, it is worth noting that the terms involving parallel motion to $\hat{\mathbf{z}}$ and may be expressed in terms of $Z'(\xi_\alpha)$ (cf. page 84) are the terms that give rise to Landau and transit-time damping when $n = 0$.

Further, more mathematical discussions of all three damping mechanisms may be found in any good plasma physics textbook [*e.g.*, *Stix*, 1992; *Chen*, 1984; *Swanson*, 1989].

4.5 Calculated Properties of the Kinetic Alfvén Wave

Figure 4.2 shows the dispersion relations we compute for waves propagating at various angles to the mean magnetic field and for the specific value of $\beta_p = \beta_e = 0.5$. (As mentioned above, in writing equation (4.26), we assume single-temperature Maxwellian distributions for both protons and electrons. Furthermore, unless otherwise stated, we take $\beta_p = \beta_e$.) From the wave frequency (upper) panel, we can see that dispersion is fairly independent of propagation direction until $\theta_{kB} \gtrsim 60°$. This is due to the $k_\parallel$ $(\cos\theta_{kB})$ dependence in the zeroth-order approximation to the kinetic Alfvén wave dispersion relation (see, *e.g.*, equation (4.17)). The parallel-propagating wave has the greatest decay rate for a given k (lower panel). However, the decay rate for oblique propagation is of comparable magnitude until large oblique angles ($\theta_{kB} \gtrsim 60°$). This "quasi-isotropic" dissipation is in agreement with the implications of Figure 4.1.

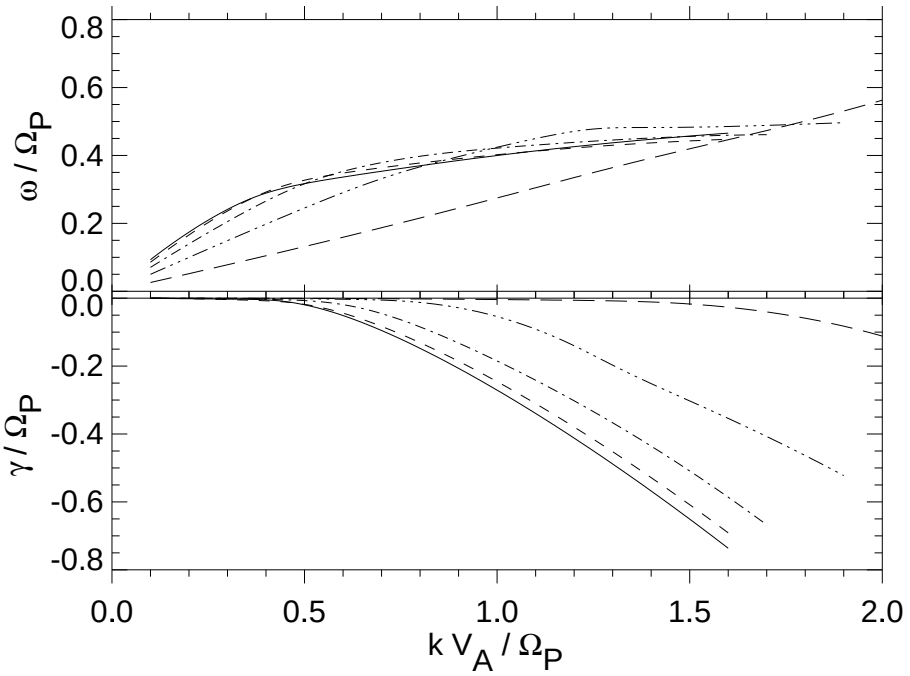

Figure 4.2: Dispersion relations for kinetic Alfvén waves propagating at various angles to the mean magnetic field. The wavenumber k, real frequency ω, and damping rate γ are all scaled to dimensionless units. The key to the lines is as follows: solid, 15°; dashed, 30°; dot-dashed, 45°; dot-dot-dot-dashed, 60°; long dashed, 75°. All solutions are for $\beta_p = \beta_e = 0.5$.

We calculate the ratios of the fluctuating electric field components $\delta\mathbf{E}$ of the wave via equation (4.23) and then the fluctuating magnetic field components $\delta\mathbf{B}$, via equation (4.20), Faraday's Law. Figure 4.3 shows the ratio of these fluctuating $\delta\mathbf{B}$ components, along with the dispersion relation.

Although the codes are capable of calculating the dispersion relation at arbitrarily large k, each panel in Figure 4.3 is truncated at the wavenumber at which γ/ω (the long dashed curve) $= -0.5$. At this wavenumber the wave is critically damped, and at even larger k, the wave can no longer be regarded as propagating.

From $\boldsymbol{\nabla} \cdot \mathbf{B} = 0$ we have $\delta B_x/\delta B_z = -\cot\theta_{kB}$ (the linearized Maxwell-Vlasov codes assume that the mean field is in the $\hat{\mathbf{z}}$ direction and that the wave propagates in the x–z plane), which is a constant for a given propagation direction. At low values of k, $|\delta B_y/\delta B_z|$ is large, demonstrating the transverse nature of the KAW. As k increases, the KAW becomes more compressive, and the ratio $|\delta B_y/\delta B_z|$ decreases towards unity. Rather than showing ratios of the components of $\delta\mathbf{E}$, we show in Figure 4.3 the quantity $|\mathbf{k}\cdot\delta\mathbf{E}|/|\mathbf{k}\times\delta\mathbf{E}|$, which may be viewed as a proxy to the ratio of Landau to cyclotron damping. We see that $|\mathbf{k}\cdot\delta\mathbf{E}|/|\mathbf{k}\times\delta\mathbf{E}|$ increases for increasingly off-axis propagation directions, implying that cyclotron damping becomes less important for increasing θ_{kB}.

In general, it is extremely difficult to separate the contributions from various damping processes (since both the $n = 0$ and ± 1 terms contribute significantly to the dispersive properties of the KAW). However, Figure 4.3 does indicate that $\delta B_z \ll \delta B_y$ for all angles at low-to-moderate wavenumber, which suggests that transit-time magnetic damping might not be as important as other damping processes in this parameter regime. (The magnetosonic wave, by its more compressive nature, therefore, is much more susceptible to transit-time damping than the KAW. However, as mentioned on page 74, the magnetosonic wave damps too quickly to be capable of an adequate explanation of the observed data.)

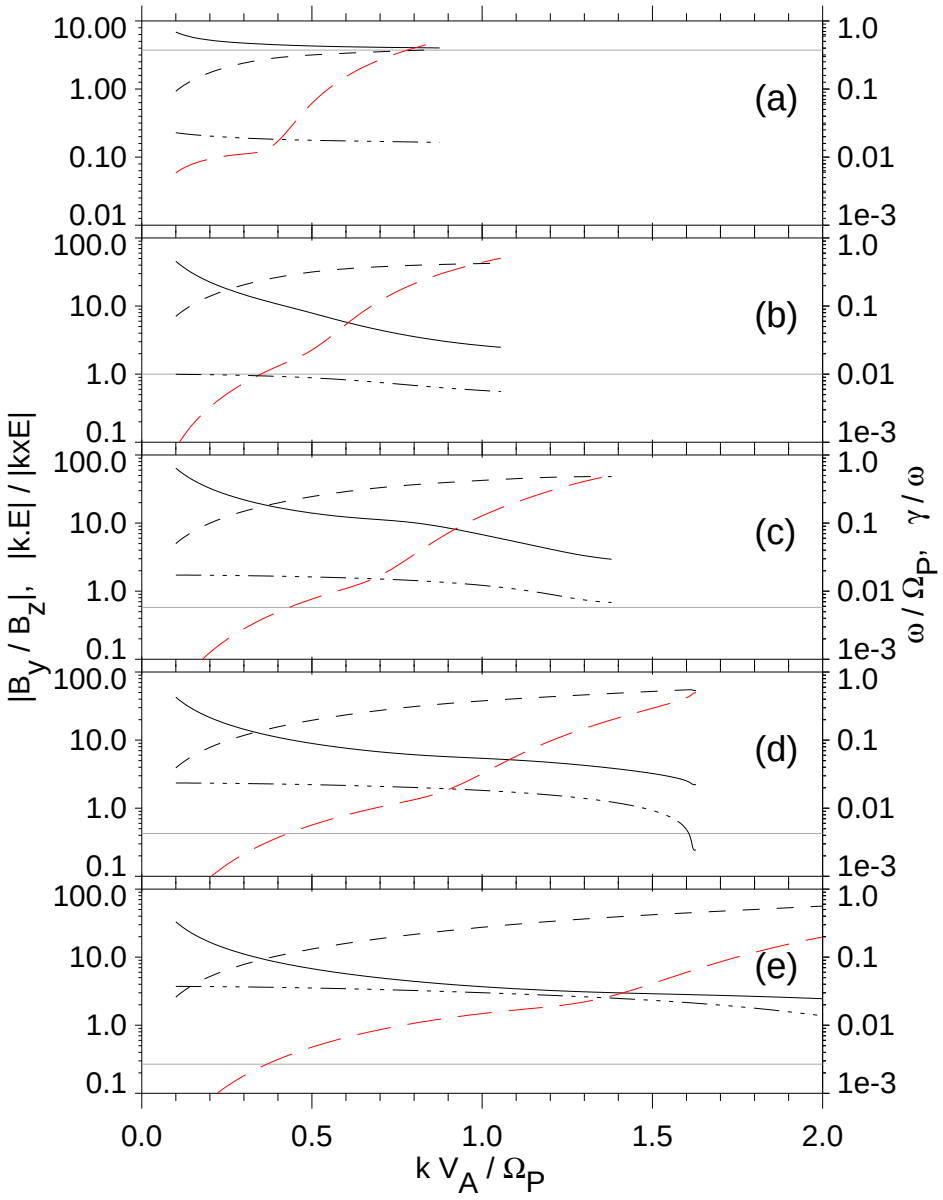

Figure 4.3: A refinement of Figure 4.2 showing the polarization properties of the wave mode. (a–e) The angle $\theta_{kB} = 15°$, $45°$, $60°$, $67°$ and $75°$. The solid curve corresponds to $|\delta B_y/\delta B_z|$; the dot-dot-dot-dashed curve, $|\mathbf{k}\cdot\delta\mathbf{E}|/|\mathbf{k}\times\delta\mathbf{E}|$; the dashed curve, ω/Ω_p; and the long dashed curve, γ/ω. The horizontal trace in each panel corresponds to $|\delta B_x/\delta B_z|$, which is a constant for given θ_{kB}.

We can isolate the electron and ion contributions to Landau damping by lowering β_e to very small values. Whatever damping remains is due to the protons. We cannot, however, separate and quantify the two contributions of the two ion damping mechanisms. Using solutions such as those shown in Figure 4.2, we can compute contours of constant γ/Ω_p for a range of β. Figure 4.4 shows the changes in the contour $\gamma/\Omega_p = -3 \times 10^{-3}$ with changing β_e. For negligible β_e (solid curve), as we move further off-axis we need to go to higher k to find the the same damping rate, as we would expect for cyclotron damping. The minimum value of k actually occurs at $\theta \sim 15°$, where the two damping mechanisms combine. We can infer from the very shallow nature of the minimum that the cyclotron contribution is greater than that of Landau damping but that some Landau damping occurs. A 4-order of magnitude increase of β_e from 10^{-6} to 10^{-2} produces no clear change in γ, so we conclude that the Landau damping observed in these cases is due to ion Landau damping. As β_e increases further, electron Landau damping increases. Damping is strongest at $\theta \sim 15°$–$30°$, where ion cyclotron damping also contributes, but continues to large angles.

The other feature to note in Figure 4.4 is that as $\theta_{kB} \to 90°$, $\gamma/\Omega_p \to 0$, and the contours become parallel to the k-axis. The KAW, or, at least, our linear codes, cannot address damping of rigorously 2-D turbulence. However, contours of constant γ/ω are finite as $\theta_{kB} \to 90°$ for 3 of the 4 values of β_e that appear in Figure 4.4.

It is typical to examine contours of constant γ/ω to compare the two halves of the solution to the dispersion equation. Such contours are shown in Figure 4.5 as a $k_\parallel$–$k_\perp$ plot. Figures 4.4 and 4.5 show that ion-cyclotron resonance dominates dissipation for small angles, but electron-Landau damping dominates above the cusp.

We can attempt to identify the origins of the various features of Figures 4.3

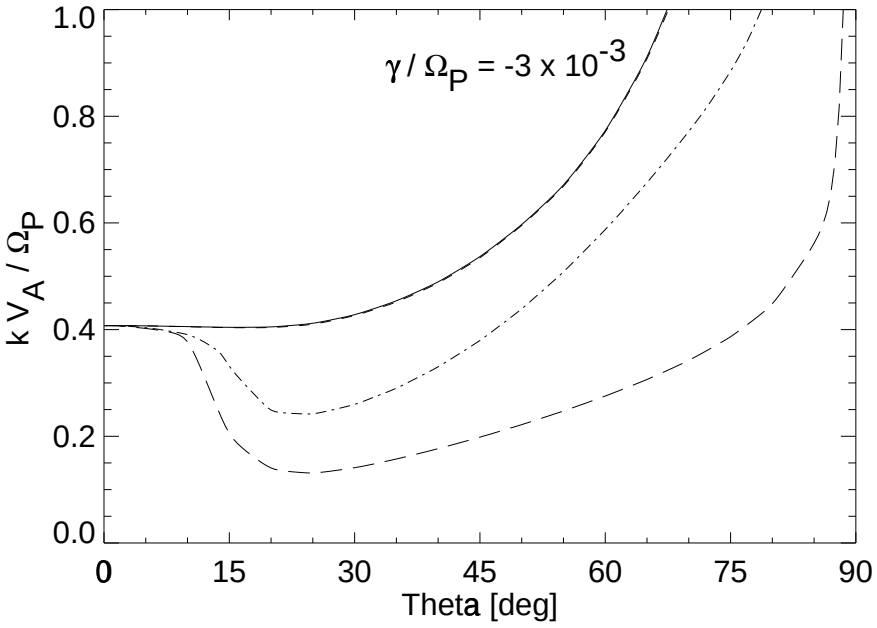

Figure 4.4: Contours of constant γ/Ω_p as a function of increasing β_e. All three contours have $\beta_p = 0.5$, the solid curve is $\beta_e = 10^{-6}$ (so as to virtually remove electron effects from the contour), the dot-dashed curve is $\beta_e = 0.5$, and the long-dashed curve is $\beta_e = 2.5$. Electron effects have very little effect when $\beta_e = 0.01$, and the corresponding contour is indistinguishable from the solid curve.

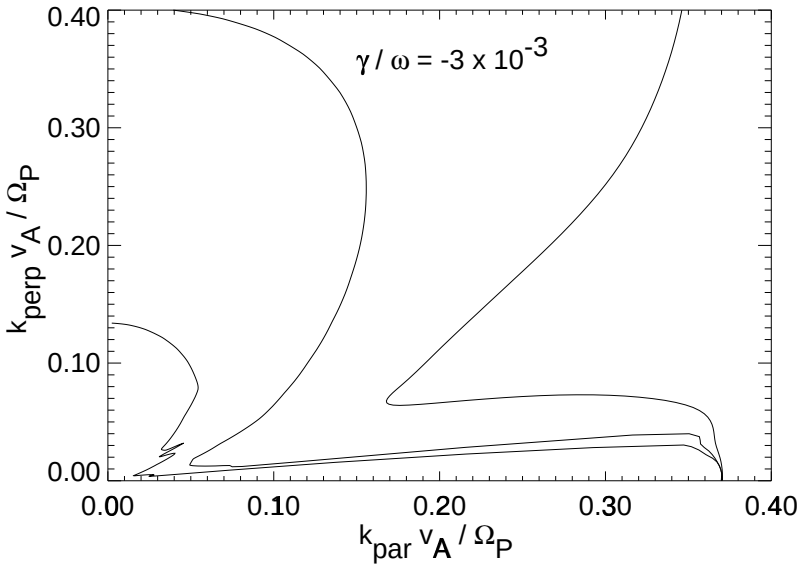

Figure 4.5: Electron resonance effects control the shape of the $\gamma/\omega = -3 \times 10^{-3}$ contour. All three contours have $\beta_p = 0.5$; from the outside in, the values of β_e for the three contours are 10^{-6}, 0.5, and 2.5. The "spikes" seen in the innermost contour at intermediate angles are real; we attribute them to cyclotron effects ($n = 2,\ 3,\ 4$), and the rest of the contour is dominated by electron-Landau damping.

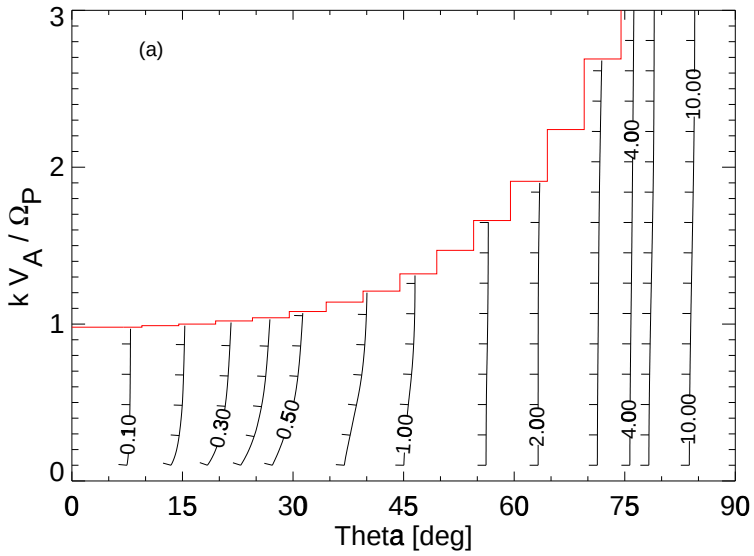

Figure 4.6: Three contour plots of $|\mathbf{k}\cdot\delta\mathbf{E}|/|\mathbf{k}\times\delta\mathbf{E}|$ for three different values of β_e. All three panels have $\beta_p = 0.5$, and the same set of contour values. The tick-marks represent the local direction of greatest (downhill) slope. The stair-stepping lines correspond to where $\gamma/\omega = -0.5$, at which point the wave may no longer be viewed as propagating (see text). (a) $\beta_e = 10^{-6}$

and 4.4 by looking at contour plots of $|\mathbf{k}\cdot\delta\mathbf{E}|/|\mathbf{k}\times\delta\mathbf{E}|$, as shown in Figure 4.6. To first order, as θ increases, so does $|\mathbf{k}\cdot\delta\mathbf{E}|/|\mathbf{k}\times\delta\mathbf{E}|$ and Landau damping becomes more important. This suggests that the cusp in Figures 4.4 and 4.5 is due to the combined effects of cyclotron and Landau resonance which are both efficient when $\theta_{kB} \sim 15°$.

Note also, in Figure 4.6, that for small values of k in the range $\theta_{kB} = 15°$–$30°$ there is a local increase in $|\mathbf{k}\cdot\delta\mathbf{E}|/|\mathbf{k}\times\delta\mathbf{E}|$ that persists for all values of β_e. We might infer from this a localized enhancement of ion Landau damping, but we cannot verify this, for reasons explained in the following paragraph.

Notice that for almost all points in $\mathbf{k}$ space, $|\mathbf{k}\cdot\delta\mathbf{E}|/|\mathbf{k}\times\delta\mathbf{E}|$ decreases with increasing β_e. This is somewhat counterintuitive, as we would expect the electron

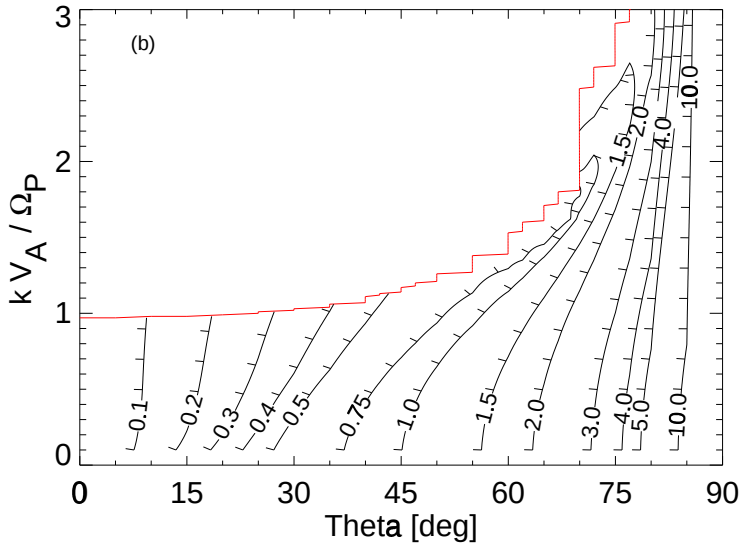

Figure 4.6: (b) $\beta_e = 0.5$

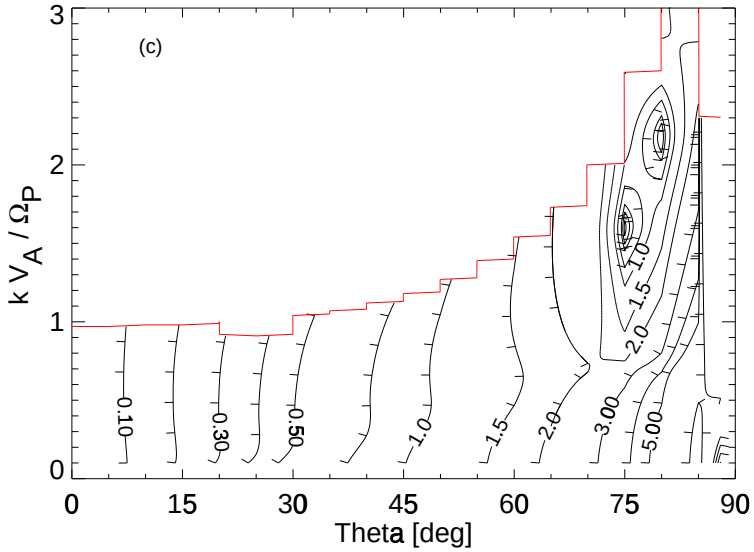

Figure 4.6: (c) $\beta_e = 2.5$.

damping strength (all due to Landau resonance) to increase with increasing β_e. This effect is especially pronounced in the two "wells" at $\theta \sim 75°$ in Figure 4.6c ($\beta_e = 2.5$). We may be able to explain this behavior as follows: as β_e increases (relative to fixed β_p) the enhanced damping affects the dispersion relation $\omega(\mathbf{k})$, as suggested by equations (4.16) and (4.17), which in turn causes $|\mathbf{k} \cdot \delta\mathbf{E}|/|\mathbf{k} \times \delta\mathbf{E}|$ to decrease. For this reason, we are not able to separate the contributions of ion Landau and ion cyclotron damping by considering $|\mathbf{k} \cdot \delta\mathbf{E}|/|\mathbf{k} \times \delta\mathbf{E}|$ alone. Pursuing this goal by other methods (*e.g.*, Taylor expansion of the dispersion tensor $\mathbf{D}(\mathbf{k}, \omega)$) is beyond the scope of the present effort.

Consideration of the simple turbulence model of section 3.4, which balances cascade rate with dissipation for left- and right-hand polarized structures, suggests that, as a global average, cyclotron-resonant damping rates are approximately twice the sum of Landau-damping and other, nonresonant damping rates. However, since $\gamma(\mathbf{k})$ varies greatly with increasing k and θ, as we have shown, we cannot say what the relative contributions of ion Landau and ion cyclotron damping are at any particular point in $\mathbf{k}$ space.

To conclude this section, we show in Figure 4.7 contours of γ/Ω_p for a range of β, and in Figure 4.8 contours of γ/ω. Figure 4.7 demonstrates concisely the effect on $\gamma(\mathbf{k})$ of k, θ and β. Throughout the range of β, contours of large (negative) γ/Ω_p (the upper contours) follow a nearly positive-definite rise to larger k with increasing θ_{kB}. For the lower contours, where dissipation is less, a greater degree of structure can be seen as the Landau resonances display their variability. If one envisions an established 3-D spectrum that is convected at varying values of θ_{kB}, the variability of the lower contours will lead to changes in the dissipation range onset frequency in a possibly fairly complex manner. Prediction of that onset in the measured reduced spectrum is therefore sensitive to both β and θ_{kB}. We shall show in section 5.2 that the onset prediction also depends on Θ_{BV}.

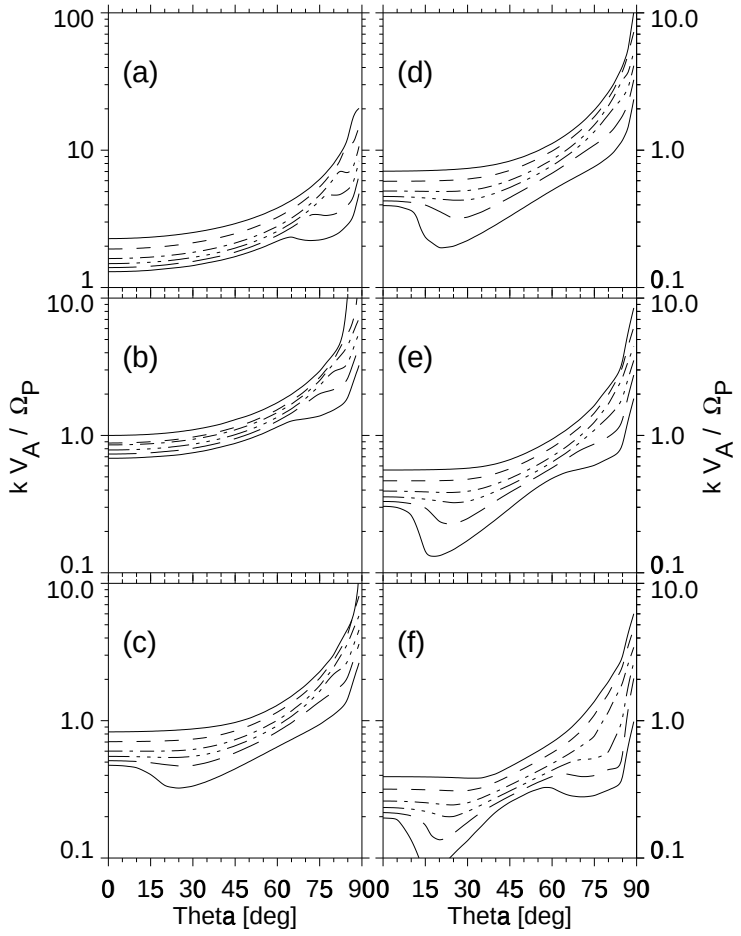

Figure 4.7: Contour plots of constant γ/Ω_p as a function of θ_{kB} for six different values of β: (a–f) $\beta = 0.01$, 0.1, 0.3, 0.5, 1.0 and 3.0. The six contours are the same for all six panels; from the outside, $\gamma/\Omega_p = -0.1$ (solid), -0.05 (dashed), -0.02 (dot-dashed), -0.01 (dot-dot-dot-dashed), -5×10^{-3} (long-dashed) and -2×10^{-3} (solid). In all cases, both the wave frequency ω and the growth (damping) rate γ approach zero as the wave propagation direction becomes perpendicular to the mean field.

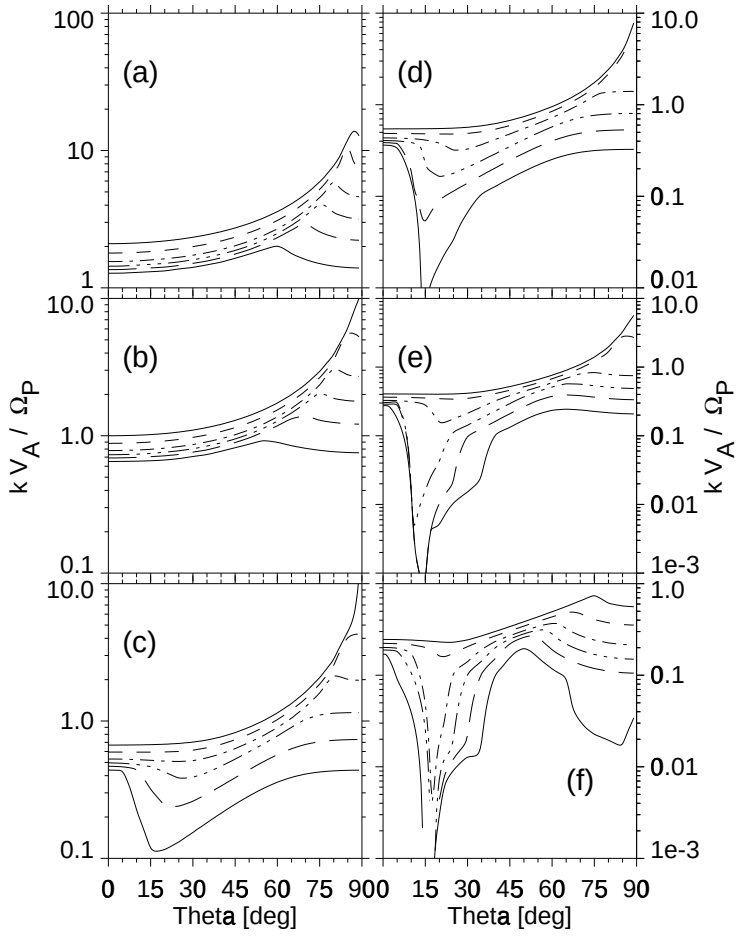

Figure 4.8: Same as Figure 4.7, but contours of constant γ/ω. The numerical values of the contours are the same as Figure 4.7.

Note that in both Figures 4.7 and 4.8, the contours at low θ_{kB} change very little with increasing β. The contours of higher γ/ω are noticeably more independent of θ_{kB} over the whole range of β in Figure 4.8, *i.e.*, more isotropic, than the contours of γ/Ω_p. At the same time, a much higher degree of variability is seen in the lower contours. We argue in the next section that the onset of the dissipation range is determined by these lower, highly variable contours for surprisingly small values of γ/ω.

4.6 Chapter Summary

We have examined the damping properties of kinetic Alfvén waves and tested if an ensemble of these waves can account for the observed features of the power spectrum of IMF fluctuations at 1 AU.

For values of β typically found in the solar wind at 1 AU, contours of constant γ/ω on a $k_\parallel$–$k_\perp$ plot have a double-lobed form. The parallel lobe, for angles $\lesssim 15°$, is dominated by proton cyclotron resonance; and the second lobe $\gtrsim 30°$ is controlled by electron Landau resonance.

Chapter 5

KINETIC ALFVÉN WAVES AND THE DISSIPATION RANGE

5.1 Synthesized 3-D Spectrum

The purpose of the present section is to test how well the observed properties of IMF fluctuation power spectra can be explained by the damping of kinetic Alfvén waves. On the basis of the previous chapters, we have (i) a collection of observed reduced power spectra $F(f)$ exemplified by Figure 2.1; and (ii) solutions of the linear KAW dispersion relation. On the basis of these solutions, we shall construct a sample 3-D spectrum $E(\mathbf{k})$, and test if the power law and abrupt break can be preserved when it is reduced to $F(f)$. In this way, we may test whether our KAW-based model is consistent with the observations.

5.1.1 Assumptions

We should like to reproduce the spectrum shown in Figure 2.1. Our synthetic $E(\mathbf{k})$ is azimuthally symmetric about $\mathbf{B}_0$. We make the critical assumption that all magnetic fluctuation energy is contained in KAWs. We do this since, as previously mentioned, the fast magnetosonic wave and the slow-mode wave are heavily damped in a high-β plasma, regardless of wavelength and thus are incompatible with the observations.

This heavy damping discounts the presence of solar-generated fast magnetosonic waves. However, *in situ* generation by secondary processes is not ruled out

[see *Sari and Valley*, 1976, and references therein], and some authors still include fast magnetosonic waves in their models [*e.g.*, *Gary*, 1999].

Taking the whole set of KAW solutions for $\beta = 0.5$ (recall that the observed $\beta_p = 0.48$ for that interval), we assume that dissipation sets in at some contour of constant γ/ω. We choose contours of constant γ/ω rather than constant γ (or, more precisely, γ/Ω_p) for two reasons: (*i*) contours of γ/ω remain finite as $\theta \to 90°$; and (*ii*) γ/ω is more relevant than γ alone for determining the time taken for a wave to decay [*Barnes*, 1966]. Thus

$$\begin{aligned} E(\mathbf{k}) &= E(k,\theta) \\ &= \begin{cases} A_0 k^{-11/3} & k < k_* \\ A_0 k_*^{-11/3} \left(k/k_*\right)^{-5} & k \geq k_* \end{cases} , \end{aligned} \tag{5.1}$$

where $k_*(\theta)$ defines the contour of γ/ω. A_0 is a global scaling factor, and is not a function of θ. The only anisotropy present in the assumed spectrum is that which arises from the $k_*(\theta)$ contour. $E(\mathbf{k})$ is set up as a 200×181 array, with 200 logarithmically spaced k values between $kV_A/\Omega_p = 5 \times 10^{-4}$ and 21.0, and 181 angles in half-degree steps from zero (parallel) to 90°. The exponents are set at $-11/3$ and -5, so that the reduced one-dimensional power spectrum will have inertial- and dissipation range spectral indices of $-5/3$ and -3 if the spectrum reduces correctly.[1]

The values of $k_*(90°)$ and $k_*(89.5°)$ are set equal to $k_*(89°)$. Linearized Maxwell-Vlasov codes cannot determine a dispersion relation for $\theta = 90°$ (perpendicular fluctuations do not propagate). We can see from the flat nature of the contours at large angles in Figure 4.8 that this is a reasonable approximation. Since waves cannot propagate at $\theta = 90°$, our model cannot address rigorously 2-D fluctuations,

[1] Recall that reduction to frequency spectrum involves integration over the two directions in $\mathbf{k}$ space perpendicular to the (radial) sampling direction. Dimensionally, then, for a reduced spectrum to have a k^{-q} dependence, the generating 3-D spectrum must fall off as $k^{-(q+2)}$.

but may be able to damp waves propagating nearly, but not exactly, perpendicular to $\langle \mathbf{B} \rangle$. We do obtain propagating solutions for θ as high as 89°.

Evidently, the assumption that $k_*(\theta)$ is defined by the contour $\gamma/\omega =$ constant is *ad hoc*. This reflects the underlying nature of turbulence which predicts the onset of a dissipation range spectrum when dissipation becomes competitive with the cascade of energy from larger spatial scales [*Batchelor*, 1970]. We neglect the issue of self-consistently identifying the onset of the dissipation range spectrum according to dissipation dynamics alone.

There are several reasons that partially justify our assumption. Firstly, the linear decay rates, γ, computed in the previous section increase more rapidly after the initial onset of dissipation than the νk^2 form of hydrodynamics. In hydrodynamics, dissipation responds to increases in the energy cascade rate by moving the spectral breakpoint to larger k until the balance between energy cascade and dissipation is reestablished. Such a response in this system is unlikely to result in a significant shift in k_{diss} due to the rapidly increasing functional form of γ.

Secondly, recall from section 1.3 that *Kolmogoroff* [1941a] and *Kraichnan* [1965] took the triple correlation time, τ_3, on which the shape of the power spectrum depends, to be τ_{NL} and τ_{NL}^2/τ_A respectively. Suppose instead that the timescale governing the cascade of energy in the MHD inertial range is $\tau_A \sim 1/kV_A = 1/\omega$, and that this range ends when the dissipation timescale $1/\gamma$ is some (significant) fraction of the cascade timescale. If we balance dissipation timescales against cascade timescales, $\gamma\tau = \gamma/\omega$ becomes a natural, if not unique, measure for the increased importance of dissipation. Admittedly, most of the inertial range spectra in our set of observations are closely comparable to the $k^{-5/3}$ prediction of *Kolmogoroff*, and, to a lesser extent, the $k^{-3/2}$ prediction of *Kraichnan*. Furthermore, by excluding the nonlinear timescale from τ_3 it is not clear how one would obtain such a power law power spectrum at all.

However, we note that the comparisons in the rest of this chapter are intended only to illustrate the likely role of kinetic Alfvén waves in the evolution of the dissipation spectrum. We recognize the extreme complexity of building a turbulence model that accounts for anisotropic spectral transfer, the dissipation of 2-D fluctuations and the dependence of both upon ambient plasma parameters. This simple analysis is offered as a reasonable beginning.

5.1.2 Reduction to Frequency Spectrum

Having constructed our synthetic 3-D spectrum $E(\mathbf{k})$, we now reduce it to a Doppler-shifted frequency spectrum according to

$$F(f) = \int E(\mathbf{k})\, \delta\left(\frac{1}{2\pi}\left(\mathbf{k}\cdot\mathbf{V}_{SW} + \omega(\mathbf{k})\right) - f\right) d\mathbf{k} \tag{5.2}$$

where $\omega(\mathbf{k})$ is the real part of the wave frequency determined from the linear Vlasov-Maxwell solutions, $\delta(\dots)$ is the Dirac delta function,[2] f is the spacecraft-frame frequency, and for $\mathbf{V}_{SW}$ we take the observed solar wind velocity for the interval in question. At this point the constant A_0 in equation (5.1) is set by trial-and-error so as to match the observed inertial range amplitude of the interval shown in Figure 2.1. The results of this reduction are shown on the left-hand scale of Figure 5.1. It is seen that the spectrum does indeed reduce correctly to $-5/3$ and -3 power laws, and that the break in the spectrum is almost exactly reproduced. The two vertical lines in Figure 5.1 correspond to the observed spectral break at 0.235 Hz and the lowest frequency in Figure 2.1, 2.7×10^{-3} Hz. The break contour used in computing Figure 5.1 is $\gamma/\omega = -3 \times 10^{-3}$.

[2] The dimensions of a Dirac delta function are the inverse of its argument, frequency in this case, so $F(f)$ does indeed have dimensions as the observed spectra of the type shown in Figure 2.1, namely $\mathrm{nT}^2\ \mathrm{Hz}^{-1}$.

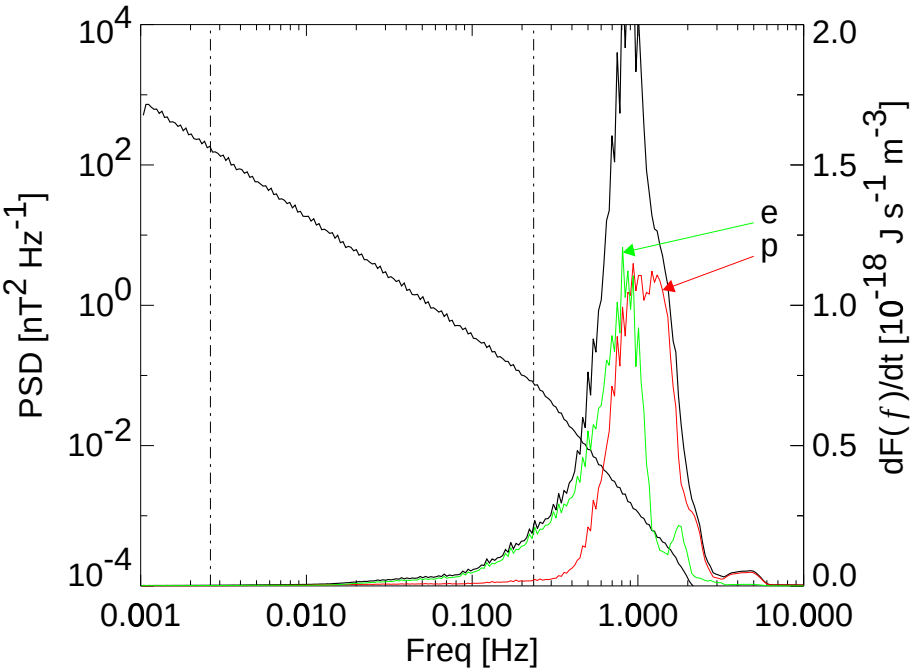

Figure 5.1: Synthetic power spectrum of kinetic Alfvén waves (left-hand scale) and heating rate $dF(f)/dt$ as a function of frequency. The total heating rate, which is the sum over all the 250 logarithmically spaced frequency bins used, is 6.36×10^{-17} J s^{-1} m^{-3}. Under the heating rate curve are the electron and proton contributions, at slightly lower and higher frequencies, respectively.

5.1.3 Heating

Having successfully tested our synthetic 3-D spectrum's ability to reproduce the break in the reduced frequency spectrum, we can now calculate the rate at which damping of kinetic Alfvén waves with this spectral form heats the background plasma.

The heating rate (in SI units) is given by

$$\dot{Q} = \frac{1}{2\mu_0} \int 2E(\mathbf{k})\gamma(\mathbf{k}) d\mathbf{k} \tag{5.3}$$

where $\gamma(\mathbf{k})$ is the imaginary part of the wave frequency. Evaluating this integral for the $E(\mathbf{k})$ computed above gives $\dot{Q} = 6.36 \times 10^{-17}$ J s^{-1} m^{-3}.

By including a Dirac delta function similar to that in equation (5.2), we can determine the frequency distribution of heating. This is shown in the second curve and right-hand scale of Figure 5.1. Some heating occurs in the inertial range of the spectrum, but the bulk of the heating is at dissipation range frequencies, peaking at $\simeq 1$ Hz.

In view of our earlier discussion on how electrons and protons affect the contours of constant γ/ω, it is of interest to see how much of the dissipated energy goes into heating electrons and how much heats protons. To do so, we take our solutions of $\gamma(\mathbf{k})$ for $\beta_e = 10^{-6}$, thereby effectively removing all electron-resonant damping. Using the same $E(\mathbf{k})$, we recompute the heating rate of protons only, which is 3.66×10^{-17} J s^{-1} m^{-3} or 58% of the total. The electron contribution is never determined by itself, but is taken to be the difference of total and proton heating. The two heating distributions as functions of frequency are also shown in Figure 5.1. The proton contribution is broader, peaks at a higher frequency, and the electrons alone contribute to inertial range heating.

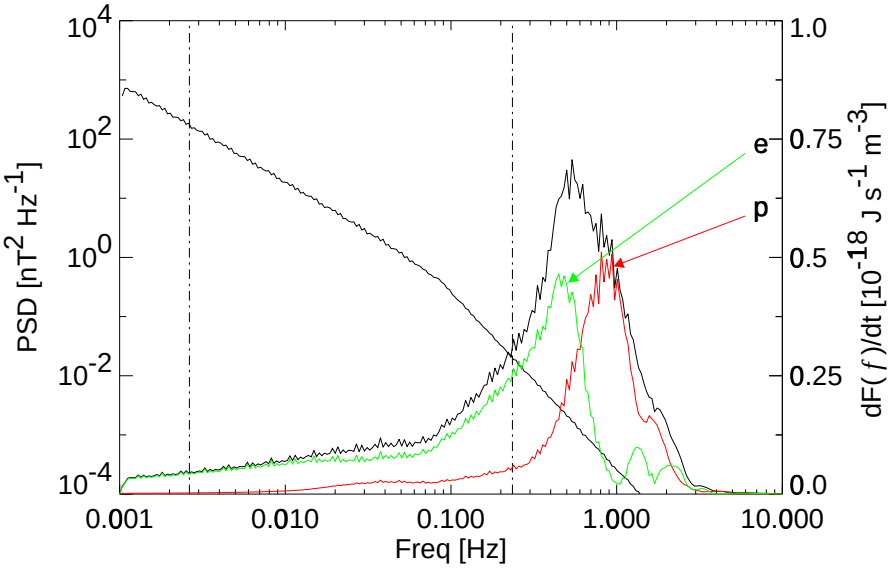

Figure 5.2: The same as Figure 5.1 but with $\beta_e = 2.5$, $\beta_p = 0.5$. The spectral break frequency is underestimated by a factor of about 3. The total heating rate is now 4.09×10^{-17} J s^{-1} m^{-3}, of which the protons contribute only 40%. Note the large amount of heating at inertial range frequencies due to the electrons.

5.1.3.1 Differing electron and proton temperatures

As a demonstration of electron effects, we have also investigated increasing β_e and with it the damping rates for oblique propagation. Again, keeping $\beta_p = 0.5$, we increased β_e to 2.5. A new $E(\mathbf{k})$ was determined using newly computed KAW dispersion solutions, but keeping the same critical value of γ/ω for the spectral break contour; *i.e.*, using the innermost contour of Figure 4.5. Figure 5.2 shows the frequency spectrum $F(f)$ and heating rate $\dot{Q}$ based on this elevated β_e.

The break in the new $F(f)$ is now at about 0.09 Hz, despite the fact that the proton-dominated parallel lobe of Figure 4.5 is virtually unchanged with increased β_e. We might reasonably expect therefore that the parallel lobe plays little role in determining the location of the spectral break in this example, which is controlled mostly by: (*i*) electron, rather than proton effects; and (*ii*) dissipation at moderate

to large angles of propagation. This is at variance with the commonly held intuition that proton cyclotron resonant effects alone determine the location of the spectral break.

5.1.3.2 Solar wind temperature profile

The observed radial solar wind proton temperature profile would be expected to fall as $T_p \sim R^{-4/3}$ if the solar wind were to cool adiabatically as it expands out into the heliosphere. Instead, the observed Voyager 1 and 2 profile from 1–43 AU falls as $T_p = T_0 R^{-1/2}$ [*Richardson et al.*, 1995, shown here in Figure 1.6]. *Gazis and Lazarus* [1982] fitted the data from 1–10 AU and found a $T_p \sim R^{-0.7}$ dependence. In either case, there must be, therefore, *in situ* heating of the solar wind. The equation of solar wind temperature evolution [*Williams et al.*, 1995, their equation (2)], is

$$\frac{dT_p}{dr} + \frac{4}{3}\frac{T_p}{r} = \frac{2}{3}\frac{\dot{Q}}{V_{SW} n k_B}, \tag{5.4}$$

where n is the local solar wind number density and k_B the Boltzmann constant. When no *in situ* heating occurs, $\dot{Q} = 0$, and an adiabatic temperature profile results. We can compare our KAW-calculated ion heating rate (58% of $\dot{Q}$), to the value required to balance the two sides of equation (5.4).

If we take the observed data to fall as $T_p \sim R^{-a}$, then the excess heating (left-hand side of equation (5.4)) at 1 AU is $\left[\frac{4}{3} - a\right] T_0$ K AU^{-1}. *Richardson et al.* [1995] took T_0, the temperature at 1 AU, to be 3.8×10^4 K. For our exemplary period, we find the proton temperature gradient excess at 1 AU, derived from $\dot{Q}$ via the right-hand side of equation (5.4), to be 1.10×10^5 K AU^{-1}, which is 3.5 times greater than required if we take the Richardson *et al.* values for a and T_0, or only 1.1 times greater than required if we take the corresponding observed local temperature for the 1-hour interval, $T_0 = 1.2 \times 10^5$ K. The overestimates become worse if we take the *Gazis and Lazarus* [1982] profile, or any other profile that falls faster with distance than $R^{-1/2}$.

One might argue that those measurements further from the sun have more weight in determining the power law indices for the Voyager radial temperature profile, and as such, the observed $T_p = T_0 R^{-1/2}$ profile is less applicable at 1 AU. *Freeman* [1988] uses Helios data from 0.3 to 1 AU and finds good power-law temperature dependence inside 1 AU. Freeman separates his data according to solar wind speed and finds that the power law index decreases with increasing solar wind speed, while the temperature at 1 AU increases. At very low wind speeds, $V_{SW} < 300$ km s^{-1}, there is almost no implied heating excess. For solar wind speeds in the range $500 < V_{SW} < 600$ km s^{-1}, such as is the case in our exemplary period, Freeman fits a $T_p = 1.3 \times 10^5 R^{-0.83}$ K power law, which implies that the calculated KAW heating is 1.7 times greater than is required to match Freeman's power law.

We believe that these results, within a factor of 3 of observation, represent acceptable agreement, given the simple nature of our theory and the inherent variability of the solar wind. Indeed, the assumption, as made by *Richardson et al.* [1995], of a single power law temperature profile for all heliocentric distances is by no means certain. A power law is scale invariant, and as such will not be a reasonable approximation if new physics becomes important at a specific scale, as is the case for pickup ions beyond about 10 AU. At large heliocentric distances, pickup ions are believed to contribute, if not dominate, the heating through the cascade of ion-excited wave energy [*Williams et al.*, 1995; *Zank et al.*, 1996; *Matthaeus et al.*, 1999b], which causes the radial temperature profile to be flatter than it otherwise would. At the inner extremes of Helios' orbit the temperature profile may deviate from adiabatic for another reason, such as the (fast) damping of initial-condition waves [*Tu*, 1988; *Marsch*, 1991] and the slow spectral transfer of energy due to high cross helicity [*e.g.*, *Dobrowolny et al.*, 1980b; *Grappin et al.*, 1982, 1983; *Roberts et al.*, 1987b].

5.1.3.3 Comparison with turbulent cascade rate

The final test we can do with our calculated dissipation rate is to compare it to the turbulent cascade rate ε inferred from the observed inertial range power spectrum (Figure 2.1). We would expect approximate equality between the two. In the turbulence picture of fluctuations, the rate at which energy enters the dissipation range is balanced by the rate at which it is dissipated and heats the background plasma. To ease comparison with previous work in this field, where ε is expresses in cgs units (ergs g^{-1} s^{-1}), we will scale our calculated dissipation rate ε in cgs units (ergs g^{-1} s^{-1}). The total heating rate (both proton and electron contributions from our synthetic KAW spectrum), is found to be $\dot{Q} = 8.38 \times 10^7$ ergs g^{-1} s^{-1}.

To infer ε from the observed power spectrum, we follow the approach of *Coleman* [1968], although we shall correct a slight and subtle error that he introduced. Coleman used the magnetohydrodynamic formulation of *Kraichnan* [1965] to calculate ε: the omnidirectional inertial-range spectrum of turbulent kinetic energy (per unit mass) is

$$E(k) = A(\varepsilon V_A)^{1/2} k^{-3/2}, \tag{5.5}$$

where V_A is the Alfvén velocity and A is a numerical constant. From the (hydrodynamic) formulation of *Kolmogoroff* [1941a]:

$$E(k) = C\varepsilon^{2/3} k^{-5/3}. \tag{5.6}$$

The two numerical constants A and C can be linked by the relation $A = C^{3/4}$ [*Matthaeus and Zhou*, 1989]. Taking $C = 1.6$ [*Batchelor*, 1970] gives $A = 1.42$.

The $E(k)$ term in equations (5.5) and (5.6) is an omni-directional spectrum, whereas Figure 2.1 depicts a reduced spectrum. From Batchelor's equation (3.4.17) and after some algebra, the reduced and omni-directional spectra can be related by

$$E^r(k) = \int_k^\infty \frac{E(k')}{k'} dk'. \tag{5.7}$$

The derivation of equation (5.7) is included in Appendix D, where it is equation (D.5). For a power law form $E(k) \sim k^{-\alpha}$, we have $E^r(k) = \alpha^{-1} E(k)$.

In the Kraichnan formulation we have

$$E^r(k) = \tfrac{2}{3} E(k) = \tfrac{2}{3} A \left(\varepsilon V_A\right)^{1/2} k^{-3/2},$$

which upon rearranging gives

$$\varepsilon = \left(\tfrac{2}{3} A\right)^{-2} V_A^{-1} \left[E^r(k)\right]^2 k^3.$$

The frequency spectrum in Figure 2.1, denoted as $F(f)$, must contain the same spectral power in range df as $E^r(k)$ contains in range dk. Therefore $fF(f) = kE^r(k)$. By substituting $k = 2\pi f / V_{SW}$, we obtain

$$\varepsilon = \frac{2\pi}{V_A V_{SW}} \left(\tfrac{2}{3} A\right)^{-2} \left[F(f)\right]^2 f^3. \tag{5.8}$$

Since $F(f)$ must be scaled to velocity (Alfvén) units, and taking the geometric mean over the 370 spectral estimates in the range 0.003–0.1 Hz, we find that $\varepsilon = 5.15 \times 10^6$ ergs g^{-1} s^{-1}, which is 16 times smaller than the KAW dissipation rate (for proton and electron heating combined).

Repeating the same procedure for the Kolmogoroff ($k^{-5/3}$) formulation gives

$$\begin{aligned} \varepsilon &= \frac{2\pi}{V_{SW}} \left(\tfrac{3}{5} C\right)^{-3/2} \left[F(f)\right]^{3/2} f^{5/2} \\ &= 1.47 \times 10^8 \text{ ergs g}^{-1} \text{ s}^{-1}, \end{aligned} \tag{5.9}$$

which is only 1.75 times larger than the KAW dissipation rate. Given that the observed spectral slope of the interval in Figure 2.1 is -1.67, we feel that the Kolmogoroff-derived result has greater validity than the Kraichnan result.

For completeness, we could also try to compare our dissipation rate with the simple hydrodynamic expression $\varepsilon = u^3/\ell$ [*Batchelor*, 1970], where u is the rms fluctuation speed and ℓ is the correlation scale. However, the correlation scale at 1 AU is typically longer than can accurately be determined from 1 hour of data, implying that the resulting value of ε might not be reliable.

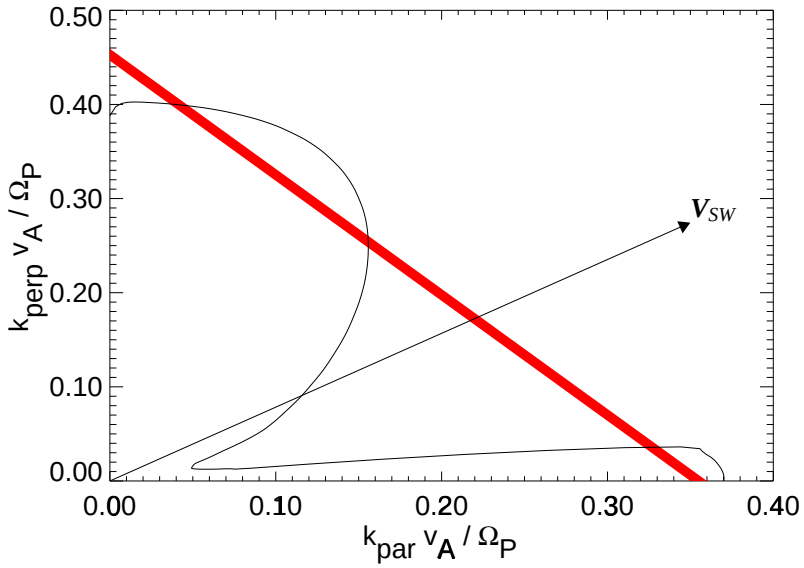

Figure 5.3: Adaptation of Figure 4.5 showing the band of wave vectors $\mathbf{k}$ with the same radial projection $\mathbf{k} \cdot \mathbf{V}_{SW}$. The shaded band *is* perpendicular to $\mathbf{V}_{SW}$; it is the scale that is not square.

5.2 Prediction of Spectral Break Frequency

From Figure 5.1, our model of a 3-D spectrum of kinetic Alfvén waves does well at predicting the spectral break frequency, given a judicious choice of γ/ω. What remains to be seen is how well the model works for all the intervals we have studied. The method used to produce Figure 5.1, *i.e.*, first calculating a k–θ contour for each interval (with the observed β) and each value of γ/ω, and constructing a fully 3-D $E(\mathbf{k})$ which is then reduced to a frequency spectrum, is rather labor-intensive. Instead, we take an array of values of k lying on contours of constant γ/ω indexed by β and θ and interpolate between them for the precise value of β for the interval of interest. For the purposes of demonstration, we assume that $\beta_e = \beta_p$ and compare the observed break frequency with the prediction derived from the observed β_p.

We adopt a simplified method of performing the frequency reduction shown in Figures 5.1 and 5.2. For each of the intervals in our dataset, we determine the

wave vector lying on the spectral break contour of constant γ/ω for which $\mathbf{k} \cdot \mathbf{V}_{SW}$ is maximum and Doppler shift the frequency corresponding to this $\mathbf{k}$ (read off the appropriate dispersion relation) into the spacecraft frame to be the KAW-predicted break frequency marking the onset of dissipation. The "maximum projection" argument may be justified as follows. There exist a range of wave vectors $\mathbf{k}$ that Doppler shift to the same spacecraft frame frequency f, as shown by the top-left to bottom-right stripe perpendicular to $\mathbf{V}_{SW}$ in Figure 5.3. Some of the wave vectors in this stripe are "outside" the contour, and as such have very little energy (since the dissipation spectrum falls steeply outside the break contour). However, other wave vectors are still "inside" the contour, and have energy-containing inertial range spectra. Those wave vectors whose spectra are already dissipative are hidden by those that are not yet dissipative. Only when a spacecraft-frame frequency is chosen for which no more inertial range energy is left in any 3-D wave vector can the reduced spectrum demonstrate the dissipative form. This occurs when $\mathbf{k} \cdot \mathbf{V}_{SW}$ is maximum along the contour of constant γ/ω. This simple shortcut has been tested against the more detailed analyses of the previous section and verified.

We choose a single value of γ/ω to define the spectral break contour for all intervals in our dataset. The value chosen to define the γ/ω contours is varied by trial-and-error until the best-fit straight line through the data has unit slope. Figure 5.4a shows the observed break frequency versus the predicted value using the best-fit value $\gamma/\omega = -0.01$. Each point is calculated from the observed β_p for the corresponding interval in the dataset.

Although the best-fit straight line, $y = (-0.043 \pm 0.079) + (1.025 \pm 0.108)x$, is plotted, we do not believe that this line truly represents the data. The January 1997 magnetic cloud data (open circles) clearly form a separate population from the undisturbed solar wind data, and these points affect the slope and intercept of the best-fit straight line. The best-fit line through all the data is clearly not the best fit

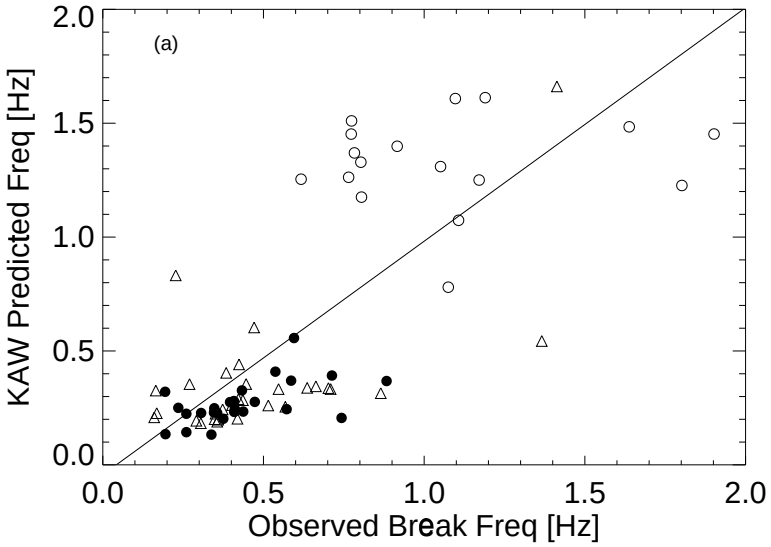

Figure 5.4: Plots of KAW-predicted spectral break frequency against observed break frequency. As in Figure 4.1, quiet solar wind observations are shown as triangles, and January 1997 observations are circles. Open circles correspond to observations inside the magnetic cloud and filled circles correspond to solar wind observations before and after the CME. (a) Best-fit value of $\gamma/\omega = -0.01$, derived from the observed β_p.

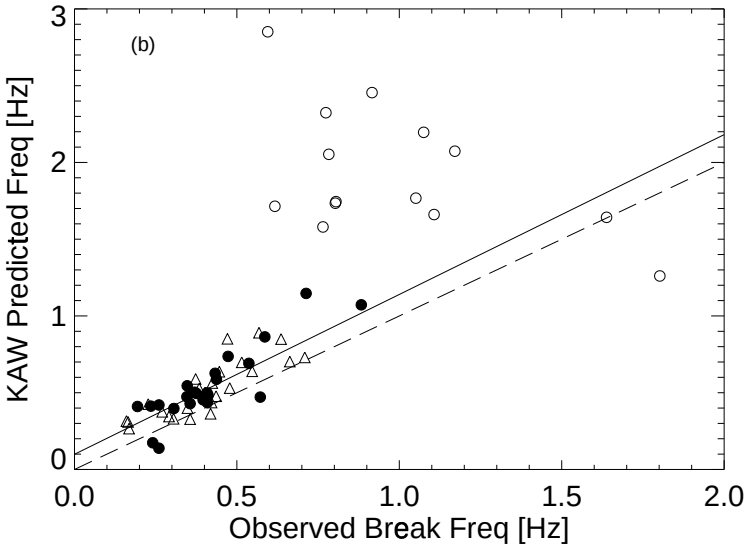

Figure 5.4: (b) Using β_e instead of β_p to characterize the observations produces much tighter results. The solid line is the best-fit straight line through the data, excluding the magnetic cloud observations, also corresponding to the contour $\gamma/\omega = -0.01$, and the dashed line is $y = x$.

to the solar wind data points.

According to *Leamon et al.* [1998c, recapped in section 3.6.2] , the geometry of magnetic fluctuations is much more two-dimensional in a magnetic cloud than in the quiescent solar wind, so we must question the validity of our model of obliquely propagating kinetic Alfvén waves on the grounds that a highly collapsed 2-D geometry may exhibit behaviour that lies beyond the linear KAW dispersion relations. A second reason for rejecting Figure 5.4a is that the angle between the mean field and the wave vector $\mathbf{k}$ for which $\mathbf{k} \cdot \mathbf{V}_{SW}$ is maximum is consistently in the range 60°–80°. (There are only four events which are best modelled by "slab" waves determined by ion cyclotron damping, *i.e.*, $\theta_{kB} \lesssim 10°$.) As we have shown in section 4.5, at these angles electron Landau damping and thus β_e dominates the shape of the contour. It would make sense then if we use β_e rather than β_p to predict the onset of the dissipation range. This is precisely what is done to produce Figure 5.4b. The procedure described above is repeated, but the observed β_e is used instead of β_p in interpolating between the different contours of γ/ω derived from the numerical solutions of the dispersion relation. There is far less scatter of the points around the best-fit straight line of $y = (0.099 \pm 0.047) + (1.041 \pm 0.104)x$, which also corresponds to the contour $\gamma/\omega = -0.01$. (There are fewer data points in Figure 5.4b because electron plasma data are not available for all the the intervals studied.) Again, the angle θ_{kB} for which $\mathbf{k} \cdot \mathbf{V}_{SW}$ is maximum is consistently in the range 60°–80°.

We recognize that the data violate the assumption that $\beta_e/\beta_p = 1$, which was used in producing both panels of Figure 5.4 and that $\beta_e/\beta_p \neq 1$ affects the damping rate. However, we have shown in section 4.5 (Figure 4.5) that β_e-dependent resonances control the shape of the γ/ω contour at angles above $\sim 30°$, and proton effects dominate at less oblique angles. Given, therefore, the further observation that the last wave vectors to damp are in the electron-dominated region, we can ignore proton effects and $\beta_e/\beta_p \neq 1$ in calculating the spectral break frequency.

We note in the regular solar wind intervals used to generate Figure 5.4, β_e was, on average, higher than β_p: $\langle\beta_e\rangle = 0.94 \pm 0.56$, $\langle\beta_p\rangle = 0.66 \pm 0.41$, and $\langle\beta_e/\beta_p\rangle = 1.83 \pm 1.41$. The distribution of $\langle\beta_e/\beta_p\rangle$ is decidedly not normal, with large skewness and kurtosis moments.

5.3 Chapter Summary

We have examined the damping properties of kinetic Alfvén waves and tested if an ensemble of these waves can account for the observed features of the power spectrum of IMF fluctuations at 1 AU.

For values of β typically found in the solar wind at 1 AU, contours of constant γ/ω on a $k_\parallel$–$k_\perp$ plot have a double-lobed form. The parallel lobe, for angles $\lesssim 15°$, is dominated by proton cyclotron resonance; and the second lobe $\gtrsim 30°$ is controlled by electron Landau resonance.

We constructed candidate spectra (that were consistent with the observed reduced frequency spectra $F(f)$) to represent the unmeasurable 3-D spectrum $E(\mathbf{k})$. $E(\mathbf{k})$ was defined with a spectral break along a contour of constant γ/ω. For the appropriate contour, $\gamma/\omega = -3 \times 10^{-3}$, the reduced frequency spectrum $F(f)$ has a spectral break at the same frequency as in the observed power spectrum. This is a surprisingly low damping rate. For the dispersion relation of $\beta = 0.5$, $\gamma/\omega = -3 \times 10^{-3}$ occurs at $kV_A/\Omega_p = 0.2$ when $\omega/\Omega_p = 0.14$. The dispersion relation here is still close to that of the MHD counterpart, yet we observe dissipation due to the compressive nature of the kinetic Alfvén wave.

Using the same $E(\mathbf{k})$ we find that the dissipation rate $\dot{Q}$, as defined by equation (5.3), is comparable (to within a factor of ~ 2) to: (*i*) the observed inertial range turbulent cascade rate; and (*ii*) the necessary *in situ* heating required for the non-adiabatic radial temperature profile of the solar wind protons at 1 AU.

The overall conclusion of this chapter is that β_e and electron Landau damping control the onset of the IMF dissipation range at spatial scales comparable to the

ion gyroradius. At the same time, the waves become more compressive and have greater fluctuations in $|\mathbf{B}|$, as is seen in the observations (see Figures 2.4 and 3.1). These characteristics are consistent with the onset of electron Landau damping and the compressible nature of the KAW at the scale of the ion gyroradius. Also, paradoxically, β_e influences the heating rate of protons, as shown in section 5.1.3.1. We also find that about half the energy dissipated from the damping of kinetic Alfvén waves goes to heating electrons.

5.3.1 Caveats

In closing, care should be exercised in interpreting the close agreement between our results and observations, given the assumptions made in producing $E(\mathbf{k})$.

1. The use of contours of constant γ/ω might appear to lead to fortuitously good agreement with observations. γ/ω is the damping strength per unit frequency; the wave amplitude will decrease by a factor e in $(2\pi|\gamma/\omega|)^{-1}$ cycles [*Barnes*, 1966]. As discussed at the start of section 5.1.1, γ/ω is a more relevant parameter than γ alone [*Barnes*, 1966]. Thus, we may further justify our assumption by claiming that waves that damp slower than this rate can easily be replenished by a spectral cascade, whereas those waves that decay faster than they can be re-excited by spectral cascade cannot remain in the inertial range. Note that putting the appropriate numerical values for the interval shown in Figure 5.1, namely $|\gamma/\omega| = 3 \times 10^{-3}$ and $\omega/\Omega_p = 0.14$, into the above expression yields an e-folding time of a little over 1 hour.

2. The assumption of an isotropic distribution of power in the synthetic spectrum (A_0 not a function of θ) is almost certainly incorrect, although we cannot say to what extent. An exact heating average could always be calculated by a more limited geometry, where not all wave vectors $\mathbf{k}$ are energetically populated: *e.g.*, a two-component model in which either only strictly parallel

and strictly perpendicular modes, or modes within a $\lesssim 30°$ cone of parallel and perpendicular (whose contours therefore resemble the "Maltese Cross" of *Matthaeus et al.* [1990]) are energetically populated. Observations [*Bieber et al.*, 1996; *Leamon et al.*, 1998a, recapped in Section 3.5] suggest that 80–90% of the inertial range energy is contained in fluctuations with 2-D or quasi-2-D symmetry.

Even so, we find in section 5.2 that the wave vectors that have the most effect in determining the spectral break frequency are at highly oblique (60°–80°) angles to the mean magnetic field.

3. We also do not consider the related possibilities of anisotropic spectral cascade; *i.e.*, ε is a function of θ and transfer of energy in the perpendicular direction of $\mathbf{k}$ space but not in the parallel direction [*Shebalin et al.*, 1983], or wave refraction away from parallel propagation by interaction with pressure-balanced structures of velocity shears [*Ghosh et al.*, 1998a]. We do this to avoid biasing our results with detailed assumptions of the spectral anisotropy that may not be consistently supported by all events. Some degree of anisotropy seems unavoidable, but more observational work is needed for it to be more thoroughly characterized. A higher degree of spectral anisotropy may not significantly alter the computed heating rates given here as the total energy of any candidate $E(\mathbf{k})$ must be the same.

At first glance, kinetic Alfvén waves might seem an inappropriate means of dissipating waves with $\theta_{kB} \simeq 90°$. Our assumption, which we have attempted to justify, that dissipation is controlled by γ/ω provides a fortuitous patch to this difficulty. The class of observations that seems most poorly described by this theory are the magnetic cloud events which as we have demonstrated [*Leamon et al.*, 1998c] are low-β and highly two-dimensional and thus the most poorly addressed by this mechanism.

Chapter 6

DISCUSSION AND SUMMARY

6.1 Discussion

Here we discuss the implications of the results presented here, and where future efforts might be best directed to further understanding of this particular branch of physics.

This dissertation analyzed the magnetic fluctuations in over 80 one-hour intervals of solar wind data from the WIND spacecraft. Of these intervals, 33 were from quiet, undisturbed solar wind, while the rest were a contiguous sample through a magnetic cloud. Admittedly, these data are exclusively from 1 AU, but they do span a wide range of plasma parameters.

The results of chapter 3, if not offering decisive proof against, cast grave doubt on the applicability of the parallel-propagating paradigm of IMF fluctuations. We also showed that a large fraction ($\sim 85\%$) of the energy must be carried by highly transverse wave vectors.

In chapter 5 we tested to see if a dynamical model based on an ensemble of kinetic Alfvén waves could describe the highly transverse, nonslab fluctuations and account for the features of the power spectrum of IMF fluctuations at 1 AU that the parallel waves failed to do. We found that such a model could accurately predict the onset of the dissipation range, and furthermore the energy dissipated was within a factor of $\lesssim 3$ of that required to match the required *in situ* heating rate.

However, there are limitations to our model. For instance, it fails to accurately explain the onset of the dissipation range inside magnetic clouds. The

extremely low values of β inside magnetic clouds cause our model to flounder for two reasons: (*i*) the fluctuations are of a highly transverse and two-dimensional nature (our model, as it is based on propagating waves, cannot handle rigidly two-dimensional fluctuations, be they in magnetic clouds or elsewhere); and (*ii*) low values of β inhibit (electron) Landau damping that, according to the results of sections 4.5 and 5.2, strongly influence the start of the dissipation range.

To test the global validity of the theory we have developed, within the limitations discussed, we must ask the question: is KAW theory applicable to parts or regions of the heliosphere other than at 1 AU?

In section 1.6 we discussed In the acceleration region of the solar corona, β is again extremely low; the much stronger magnetic field strength more than compensates for the increased density and temperature. Recent efforts in this field have focused on cyclotron damping [*e.g.*, *Cranmer et al.*, 1999], and even the gravitational damping [*Khabibrakhmanov and Mullan*, 1999, and references therein] of slab Alfvén waves. Scaling with magnetic field strength, the proton cyclotron frequency is 4–5 orders of magnitude higher in the corona than at 1 AU. The generation and maintenance of a high-frequency Alfvén wave spectrum in the corona remains a major unresolved issue. Motivated by the pitfalls of wave heating models that rely on such high frequency waves, *Matthaeus et al.* [1999a] have developed a model based on heating by 2-D MHD turbulence driven and maintained by lower-frequency waves. Is a kinetic Alfvén wave model applicable here? Landau damping would be limited, for the reasons mentioned immediately above. However, our model predicts the heating of electrons, although probably not to the approximate equipartion level found at 1 AU (see Figure 5.1). Present resonant models do not address electron heating; nevertheless, electron temperatures reach several million Kelvin.

We know that the slope of the dissipation range gets shallower as we move out in the heliosphere [*Smith et al.*, 1990b]. This probably represents no more than

a detail to be fine-tuned in the model; we do not know how to predict the dissipation range spectral index, so it is currently entered, somewhat arbitrarily, into the model as the average of all the intervals studied. To test the heating rate at 3 AU, say, we compute the 3-D spectrum of waves based on the observed local spectral slopes, the 3-D damping rate based on the observed local β_e and β_p and thus the heating excess based on the local temperature profile.

Beyond about 10–20 AU pickup ions generate waves; the damping of these waves is the major source of energy for heating the background ions in this region of space. Although all current models involving pickup ion-generated heating involve cyclotron damping of parallel-propagating Alfvén waves, it is almost certain that waves other than slab Alfvén waves are generated. Can the damping of pickup ion-generated *kinetic* Alfvén waves by means similar to those discussed in chapter 4 provide better agreement with observations? We have reason to believe that an oblique wave model would be even more effective in the outer heliosphere. The pickup ions generate waves, mostly parallel, but with a small spread in obliquity. *Shebalin et al.* [1983] and much of the recent work of *Matthaeus* [*e.g.*, *Matthaeus et al.*, 1995b] suggest that the preferred direction of energy transfer is the perpendicular direction. As the pickup ion-generated waves evolve to larger $k_\perp$ (perpendicular to the magnetic field $\mathbf{B}$), their initial finite $k_\parallel$ remains unchanged [cf. *Ghosh et al.*, 1998a]. Eventually, the now highly oblique waves will become resonant and be prime candidates to provide heating. Furthermore, this far out in the heliosphere, the magnetic field winding angle approaches 90°, such that maximum $\mathbf{k} \cdot \mathbf{V}_{SW}$ will occur very close to $\mathbf{k} \| \mathbf{V}_{SW}$.

Finally, kinetic Alfvén waves have been successfully used to model the heating of magnetospheric plasma and the formation of aurorae. The introduction of *Hollweg* [1999] again provides an extensive list of references.

6.2 Two-Dimensional MHD Turbulence

Despite the successes of the kinetic Alfvén wave model, we must not immediately decree that it is the only explanation for IMF fluctuations.

Consider, instead, and as noted and discussed in *Leamon et al.* [1998a], an alternative dynamical model for dissipation range fluctuations whereby the model of *Bieber et al.* [1996] and section 3.5 is exact, *i.e.*, the fluctuations consist of two components: (1) slab waves with wave vectors along (or nearly along) the mean field and (2) 2-D MHD turbulence, having wave vectors (nearly) perpendicular to the mean field. Unlike the kinetic wave description, this dynamical model does not lend itself to a compact representation based upon eigenmodes and dispersion relations. However, the dynamics of 2-D turbulence has been widely studied using statistical theories and simulations [*e.g.*, *Kraichnan and Montgomery*, 1980; *Matthaeus and Montgomery*, 1980; *Matthaeus and Lamkin*, 1986]. The slab/2-D composite model also emerges as a natural description of anisotropic plasma turbulence in the reduced MHD regime [*Montgomery*, 1982] and can be seen to emerge as a consequence of a formal treatment of nearly incompressible MHD at low and order-one β_p [*Zank and Matthaeus*, 1993]. The two component model also has found use in various solar wind applications (see review by *Matthaeus et al.* [1995b]), including transport of turbulence [*Tu and Marsch*, 1993] and cosmic ray scattering [*Bieber et al.*, 1994].

As far as we are aware, most previous studies that employ a two component turbulence representation (or, its close relatives, quasi-2-D or reduced MHD models) have not attempted to characterize magnetofluid or kinetic plasma dynamics in the dissipation range in any detail. However, it is clear that such a model presents interesting possibilities for influencing the dissipation range. For example, in a reduced MHD or two-component model [*Montgomery*, 1982; *Zank and Matthaeus*, 1992a; *Kinney and McWilliams*, 1997] the 2-D fluctuations are expected to engage most vigorously in the cascade phenomena that transfer excitations through the inertial

range and into the smaller dissipation scales. Thus established MHD effects are capable of supplying the dissipation range with a flux of energy from the substantial reservoirs typically found at the large scales. This dissipation, in models with simplified transport coefficients [*e.g.*, *Matthaeus and Lamkin*, 1986], is expected to occur near X-type neutral points in the poloidal field through processes related to magnetic reconnection.

A second relevant feature of models with a significant admixture of 2-D turbulence relates directly to the potential for dynamical couplings with kinetic processes. In particular, it has been established through studies of test particle orbits in dynamical MHD fields [*Ambrosiano et al.*, 1988; *Gray and Matthaeus*, 1992] that 2-D turbulence can account for substantial amounts of charged particle acceleration. Typically, a broad spectrum of energetic particles is formed, and for turbulence with energy-containing scale L, test particle energies can range up to values of $\Omega_p L/V_A$ times their initial low values (*e.g.*, initial particle speed V_A). The process by which this occurs is complex [*Ambrosiano et al.*, 1988] and appears to involve temporary trapping of test particles in or near small scale fluctuations that form near reconnection zones near magnetic X-points. A full analytical theory of this acceleration process has not yet been developed, but it seems plausible that MHD structures with transverse scales of the order of the thermal particle gyroradius might be involved. The matching conditions associated with efficient acceleration of this type are most likely temporal resonance conditions, but in any case cannot involve the usual spatial resonance condition, equation (3.3), since such couplings are absent for 2-D MHD fluctuations having $k_{\|} = 0$. The scenario in which MHD energy flows into particle energy can only be suggested by test particle studies. A full kinetic treatment is required to demonstrate the feasibility of the above process as a means of coupling MHD scales to kinetic scales and thereby forming a dissipation range. However, the existing test particle studies provide ample motivation to further examine this

possibility.

6.2.1 Comparison with Kinetic Alfvén Waves

The dynamical perspectives associated with the 2-D turbulence and kinetic Alfvén waves are quite different, but the two paradigms are not inconsistent either. Kinetic Alfvén wave theory takes into account couplings to the kinetic degrees of freedom of the plasma and ignores "wave-wave" couplings among the waves. The 2-D turbulence perspective takes full account of the couplings between the various MHD scale Fourier modes (analogous to wave-wave couplings) but discards the kinetic couplings. In this light, the two models are not contradictory but, rather, are complementary. In fact, from a geometrical or kinematic point of view the two models are nearly indistinguishable, and the nonslab, transverse magnetic fluctuations identified in section 3.5 might equally well display the dynamical features of either model.

An additional feature that is common in the two models and that is of particular interest from the point of view of dissipation mechanisms is the parallel electric field. For kinetic Alfvén waves the parallel electric field is an integral feature of the eigenmodes at cyclotron scales and, as we have shown in chapter 4, provides a significant amount of electron Landau damping. For 2-D turbulence a parallel induced electric field is associated with $\delta\mathbf{V} \times \delta\mathbf{B}$ (where $\delta\mathbf{V}$ and $\delta\mathbf{B}$ are the plasma velocity and magnetic field fluctuations, respectively). The parallel electric field would be expected to couple to kinetic processes, for example, in the manner described by *Wong et al.* [1997], presumably leading to heating of the plasma and dissipation of MHD scale energy.

One would expect the characteristic length scale of a perpendicular current sheet to be the ion inertial scale $\rho_i = v_A/\Omega_p$. We see from Figure 4.1 the good correlation between the related quantity the Larmor radius and the onset of dissipation. Preliminary investigations correlating the spectral break frequency with a

quasi-perpendicular wave vector of ion inertial scale size and Doppler-shifted to a frequency (via $\mathbf{k} \cdot \mathbf{V}_{SW}$) are promising. However, we have as yet made no attempt to assess the heating implied by a purely 2-D turbulence model.

An obvious extension to the kinetic Alfvén wave model is to incorporate rigidly 2-D turbulence to 'plug the hole' at 90° left by the linear Vlasov codes. We also need to incorporate transfer of energy in $\mathbf{k}$ space and an evolving spectrum where cascade and dissipation balance. Such an effort should also go a long way to explaining the observed dissipation range spectral index.

6.3 In Closing

In closing, as a brief summary of all the results presented in this dissertation, I repeat from the summary of chapter 3: The conclusion of this study is that a significant fraction of the magnetic wave energy must necessarily reside in highly oblique waves or quasi-2-D structures. Furthermore, the onset of dissipation cannot be governed by the dynamics of ion cyclotron damping of parallel-propagating waves.

Appendix A

POWER SPECTRAL TECHNIQUES

A.1 Fast Fourier Transform

The (fast) Fourier transform (FFT) is the standard tool for the time- and frequency-domain representation of a function. The "fast" modifier refers to tricks in the algorithm used to compute the transform, which we shall not concern ourselves with here.

Mathematically, the Fourier transform of a time series $X(t)$ may be expressed as:

$$\begin{aligned} x(f) &= \mathcal{F}[X(t)] \\ &= \int_{-\infty}^{\infty} X(t) e^{-2\pi i f t} dt, \end{aligned} \tag{A.1}$$

with its reverse transform being

$$\begin{aligned} X(t) &= \mathcal{F}^{-1}[x(f)] \\ &= \int_{-\infty}^{\infty} x(f) e^{2\pi i f t} df. \end{aligned} \tag{A.2}$$

Following from the definition of $\mathcal{F}[X(t)]$ is the important *Shift* theorem, which we shall employ presently:

$$\mathcal{F}[X(t-\tau)] = e^{-2\pi i \tau f} \mathcal{F}[X(t)] \tag{A.3}$$

In terms of space and wavenumber rather than time and frequency, we may also imagine the transform pair $X(r) \rightleftharpoons x(k)$, with the exponential factor $\mp 2\pi i k r$.

In this work $X(t)$ is one of the components $B_j(t)$ of the interplanetary magnetic field. The energy spectrum tensor $\mathbf{S}$ is then computed by

$$S_{ij}(f) = \langle B_i^*(-f) B_j(f) \rangle. \tag{A.4}$$

The power spectrum $F(f)$, as shown in Figures 2.1 and 5.1, is the trace of $\mathbf{S}$.

The ensemble average denoted by the angle brackets in equation (A.4) is accomplished by performing a sliding P point average of $\mathbf{S}$. Small data gaps and bad data points, or "flyers" should be removed and linearly interpolated over, so that the Fourier transform is supplied with contiguous data.

The drawback of the FFT technique is that aliasing and "leakage" may distort the high-frequency end of the spectrum.

Aliasing results from the power in fluctuations above the Nyquist frequency appearing in the spectrum. Unless the original time-series data were collected properly, and low-pass filtered to remove all power above the Nyquist frequency, aliasing will be present and may be a problem. Each frequency, no matter how high, is indistinguishable from one (its *alias*) in the frequency band below the Nyquist frequency. (The stroboscope uses a particular expression of this fact in apparently "slowing down" rapidly rotating or oscillating objects.) The aliased spectrum is "folded" about the Nyquist frequency. For a powerlaw true spectrum, this folding results in a flat(ter) observed spectrum at the highest frequencies. As such, it is more a problem for shallow spectra than for steeply falling ones.

Leakage is more of a problem for steeply falling dissipation range spectra. Since we are computing a spectrum for a finite interval of time, we cannot calculate the transform in equation (A.1) for all time. The resulting power spectrum is the convolution of the "true" spectrum and the Fourier Transform of the data window. The Fourier Transform of a (rectangular) data window is the sinc^2 function, which has the first side lobe on each side of the main lobe about 1/5 the height of the

main lobe (and negative). Power leaks, via these side lobes, from lower frequencies to higher ones with less power.

Filtering the data by applying other window functions that have wider main lobes and smaller side lobes can reduce the effects of leakage, but more reliable estimates of the power spectrum can be obtained by the other methods. Leakage effects can be minimized by applying a prewhitening filter to the data prior to computing the spectrum via the Blackman-Tukey method.

A.2 Blackman-Tukey Method

The *Blackman and Tukey* [1958] method calculates $\mathbf{S}$ from the Fourier transform of the correlation function $\mathbf{R}$ of the observations. This two-step technique is obviously slower than the FFT technique, especially for large datasets, but it is perhaps the most reliable method for calculating spectra.

A.2.1 Correlation Functions

Dynamical magnetic turbulence is most conveniently characterized by its two-point, two-time correlation function and related transforms of this function. If $\langle \ldots \rangle$ represents an appropriately defined ensemble average, the two-point, two-time correlation function is

$$\mathbf{R}(\mathbf{r}, \tau) = \langle \mathbf{B}(\mathbf{x}, t)\mathbf{B}(\mathbf{x} + \mathbf{r}, t + \tau) \rangle \tag{A.5}$$

In a homogeneous medium the correlation $\mathbf{R}(\mathbf{r}, \tau)$ is a function only of the relative coordinates and will contain most of the accessible statistical information about the medium [*Matthaeus et al.*, 1990].

Since the solar wind is super-Alfvénic throughout most of the heliosphere (and definitely in the region we are studying at 1 AU), it satisfies the "frozen-in flow" hypothesis of *Taylor* [1938]. Therefore, the time and space lags are related ($\mathbf{r} = \tau \mathbf{V}_{SW} = \tau V_{SW} \hat{\mathbf{R}}$), and may be used interchangeably: $R_{ij}(\tau V_{SW} \hat{\mathbf{R}}, 0) = R_{ij}(0, -\tau)$.

In this case, the relation $2\pi f = \omega = V_{SW}k$ can be used to relate frequency and wavenumber spectra.

Once $R_{ij}(r)$ is computed, the energy spectrum tensor is evaluated according to

$$S_{ij}(\mathbf{k}) = \left(\frac{1}{2\pi}\right)^3 \int R_{ij}(\mathbf{r}) e^{-i\mathbf{k}\cdot\mathbf{r}} d^3r. \tag{A.6}$$

A.2.2 Computation of the Correlation Function

The correlation function $R_{ij}(r)$ is computed by the formula

$$R_{ij}(n) = \frac{1}{M-n} \sum_{P=1}^{M-n} B_i(P) B_j(P+n), \tag{A.7}$$

where $n = 0, 1, 2, \ldots, N$, M is the number of data points in the record, and N is the maximum lag for which R_{ij} is evaluated. It is implicit that $R_{ij}(n) = R_{ij}(n\Delta x)$, where Δx is the spacing of data points in the record.

A.3 Structure Function

This spectral method was developed and applied by *Smith et al.* [1990b]. The correlation function **R** is approximated from the structure function **D** of the data and then Fourier transformed as in the Blackman-Tukey method.[1]

The diagonal elements of the structure function

$$D_{ii}(\tau) = \langle [B_i(t) - B_i(t+\tau)]^2 \rangle \tag{A.8}$$

are related to those of the correlation function, $R_{ii}(\tau) = \langle B_i(t) B_i(t+\tau) \rangle$, by

$$D_{ii}(\tau) = 2\langle B_i^2 \rangle - 2R_{ii}(\tau), \tag{A.9}$$

[1] It is unfortunate that the structure function and the dispersion tensor of sections 1.2.1 and 4.5 both are represented by **D**. We shall not consider the dispersion tensor here, nor shall we consider the structure function outside of this appendix.

thus $D_{ii}(0) = 0$ and $R_{ii}(0) = 2\langle B_i^2 \rangle > 0$. The averaging period will affect $\langle B_i^2 \rangle$, and thus the low-end of the spectrum computed from the correlation function. Ergodic theory [*e.g.*, *Panchev*, 1971] suggests that measurements of $R_{ii}(\tau)$ are susceptible to error from unresolved low-frequency power, while $D_{ii}(\tau)$ is less sensitive to errors resulting from finite maximum lags. The spread of estimates of the correlation time should be narrower for the structure function analysis, because $D_{ii}(0) = 0$.

The field variance may be estimated according to $\langle B_i^2 \rangle \simeq D_{ii}(\tau_{\max})/2$ (letting $R_{ii}(\tau_{\max}) \to 0$ in equation (A.9), as one would expect for large lags), and the resulting approximation to the correlation function is $R_{ii}(\tau) \simeq D_{ii}(\tau_{\max})/2 - D_{ii}(\tau)/2$. This may then be transformed into the energy spectrum tensor according to equation (A.6). The approximation to the correlation function contains the same level of accuracy in the computed small scale structure as was obtained in the structure function. As such, it is a better tool for dealing with steeply falling spectra.

The structure function method was used to confirm the results of the power spectra computed from the Blackman-Tukey method. The two methods agreed well. However, a method of calculating the magnetic helicity from the off-diagonal elements of **R** has yet to be included in the structure function analysis, and despite its potential merits, all the spectra of the data intervals and their secondary properties shown in this dissertation were computed by the Blackman-Tukey method.

A.4 Treatment of data

As outlined in section 2.2, several operations were performed on the downloaded WIND magnetic field data prior to computation of spectra. For convenience, all processing was done in fully automated Fortran 'batch' jobs that I wrote and ran overnight on the Bartol Research Institute's VAX/VMS cluster. The only parameters I needed to provide to the programs were the start and end times of each interval of data, and the mean solar wind speed of that interval (to convert between frequency f and wavenumber k).

A.4.1 Automated Badpoint Removal

As mentioned in section 2.2, one outlying spike in the time series data contributes energy across a large range of frequencies in the resulting spectrum. To this end, the data are twice run through an automated bad point editor. On the first, global, pass the variance of each of the four input time series (three components and the magnitude) is computed. Any point that is more than $3.5\times$ the variance σ from the mean in any component is flagged bad and its value changed to -99.9. The second, local, pass splits the data into 2000-point blocks. The mean and variance are computed for each block, and any point that is $2.5\times$ the variance is flagged. A more aggressive 2.5σ limit is used as the variance is typically less for 2000 points than it is for the full series. Typically, 1% of the dataset (~ 400 points out of 40 000) are removed in this way.

The Fortran codes that calculate the Blackman-Tukey correlation function (*i.e.*, the computation of equation (A.7)) are smart enough to ignore any bad points in the data. The bad value (-99.9) is not a numerical value, but rather just a flag or code number. In this case the average over the $(M - n)$ points is replaced with a sum over $(M - n - n_{\mathrm{bad}})$ points.

This is another reason why the Blackman-Tukey method is chosen over the simple Fourier transform, which requires that data gaps be linearly interpolated over.

A.4.2 Prewhitening and Postdarkening

A prewhitening filter is a first-order difference operator applied to the data before the spectra are computed. If $x[n]$ is the input time series data, then

$$y[n] = x[n+1] - x[n] \tag{A.10}$$

is the prewhitened output times series. The output series is evidently one point shorter than the input. This operation is known as 'whitening' because the spectrum of differences approaches that of white noise (*i.e.*, flat). Postdarkening is the subsequent inverse operation and corrects the spectrum produced from whitened data to its true shape.

Bieber et al. [1993a] developed the technique as an extension to the Blackman-Tukey correlation function method that is particularly effective at suppressing unresolved low-frequency power.

The $x[n]$ that we are concerned with here are the components of the interplanetary magnetic field $\mathbf{B}$. Define, then, the vector difference time series:

$$\Delta\mathbf{B}(t) = \mathbf{B}(t + \Delta\tau) - \mathbf{B}(t) \tag{A.11}$$

from which is formed the correlation function of the differences (cf. equation (A.5)),

$$R_{ij}^{\text{white}}(\tau) = \langle \Delta B_i(t) \Delta B_j(t + \tau) \rangle \,. \tag{A.12}$$

Using the definition of the difference series it then follows that the correlation of the differences, equation (A.12), is related to the ordinary correlation, equation (A.5), by

$$R_{ij}^{\text{white}}(\tau) = 2R_{ij}(\tau) - R_{ij}(\tau - \Delta\tau) - R_{ij}(\tau + \Delta\tau). \tag{A.13}$$

Taking the Fourier transform of equation (A.13) and employing the shift theorem, equation (A.3), we obtain $S_{ij}^{\text{white}}(f)$, the whitened spectral density matrix:

$$\begin{aligned} S_{ij}^{\text{white}}(f) &= 2S_{ij}(f) - e^{-2\pi i \Delta\tau f} S_{ij}(f) - e^{+2\pi i \Delta\tau f} S_{ij}(f) \\ &= 2S_{ij}(f) \left[1 - \cos(2\pi\Delta\tau f)\right] . \end{aligned}$$

Therefore,

$$S_{ij}(f) = \frac{S_{ij}^{\text{white}}(f)}{4\sin^2(\pi\Delta\tau f)}, \tag{A.14}$$

where we have used the identity $\cos 2\theta \equiv 1 - 2\sin^2\theta$.

A.5 Computation of Magnetic Helicity

The method used to compute the spectrum of magnetic helicity in the solar wind from the correlation function $\mathbf{R}$ was developed by *Matthaeus et al.* [1982].

Magnetic helicity can be defined by $H_m = \langle \mathbf{A} \cdot \mathbf{B} \rangle$, where $\mathbf{A}$ is the magnetic vector potential of $\mathbf{B}$. Frequently, $\mathbf{A}$ and $\mathbf{B}$ are taken to be the fluctuating fields, and as such, H_m is the helicity of the fluctuations.

In terms of a frequency or wavenumber spectrum, let H_{ij} be the ijth component of the Fourier transform of the $\langle \mathbf{A} \cdot \mathbf{B} \rangle$ correlation (cf. equation (A.5)):

$$\begin{aligned} H_{ij}(\mathbf{k}) &= \langle A_i(\mathbf{k}) \cdot B_j(\mathbf{k}) \rangle \\ &= \langle A_i(\mathbf{k}) \cdot (\boldsymbol{\nabla} \times \mathbf{A}(\mathbf{k}))_j \rangle \\ &= \langle A_i(\mathbf{k}) \cdot (i\mathbf{k} \times \mathbf{A}(\mathbf{k}))_j \rangle. \end{aligned}$$

In terms of the Levi-Civita symbol, the ith component of $\boldsymbol{\nabla} \times \mathbf{A}$ is $\varepsilon_{ijl} \partial_j A_l = \varepsilon_{ijl} (ik)_j A_l$. Thus,

$$\begin{aligned} H_{ij}(\mathbf{k}) &= A_i \varepsilon_{jrs} (ik)_r A_s \\ &= i \varepsilon_{jrs} k_r \frac{S_{is}}{k^2}, \end{aligned} \tag{A.15}$$

where we have used the fact that $A_i A_s \rightleftharpoons S_{is}/k^2$, since $B_i B_s \rightleftharpoons S_{is}$ and $\mathbf{B} = \boldsymbol{\nabla} \times \mathbf{A}$.

Using only a single spacecraft, we cannot fully determine $\mathbf{R}(\mathbf{r})$ and hence $\mathbf{S}(\mathbf{k})$. Instead, we have only correlations along a set of collinear separations $\mathbf{r} = (r_1, 0, 0)$. A full Fourier decomposition is not possible in this situation, but reduced, (one-dimensional) spectra may be computed. The reduced spectrum tensor $\mathbf{S}^r$ is

$$\begin{aligned} S^r_{ij}(k_1) &= \int S_{ij}(k_1, k_2, k_3) dk_2 dk_3 \\ &= \frac{1}{2\pi} \int dr_1 e^{-ik_1 r_1} R_{ij}(r_1, 0, 0) \end{aligned} \tag{A.16}$$

The reduced magnetic helicity spectrum then becomes

$$\begin{aligned} H_m{}^r(k_1) = (H_m)_{jj}(k_1) &= i\int \varepsilon_{j1s}\frac{k_1}{k^2}S_{js}(k_1,k_2,k_3)dk_2dk_3 \\ &= i\int \frac{k_1}{k^2}\left[\varepsilon_{312}S_{32}(k_1,k_2,k_3)+\varepsilon_{213}S_{23}(k_1,k_2,k_3)\right]dk_2dk_3 \\ &= i\frac{1}{k_1}\left(S^r_{32}(k_1)-S^r_{23}(k_1)\right) \\ &= i\frac{1}{k_1}\left(-2i\Im S^r_{23}(k_1)\right) \\ H_m{}^r(k_1) &= 2\Im S^r_{23}(k_1)/k_1, \end{aligned} \tag{A.17}$$

where $\Im S^r_{23}$ refers to the imaginary part of S^r_{23}. It is via equation (A.17) that the magnetic helicity spectrum is calculated from the data in our Blackman-Tukey computer codes.

As a final note, since we only have correlations along a set of collinear separations in the radial direction, the 'RTN' coordinate system is a natural one to use in the computation of magnetic helicity.

Appendix B

COORDINATE SYSTEMS AND THEIR TRANSFORMATION

B.1 Solar-Derived Coordinate Systems

The most commonly used solar-oriented coordinate system is the 'RTN' system, standing for Radial, Tangential and Normal. In a right-handed system, the x-axis points radially away from the sun, the z-axis is in the plane defined by the sun's axis of rotation and the x-axis, and the y-axis completes the right-handed triad. RTN coordinates are what *Parker* [1958] used to originally define the IMF.

B.2 Earth-Derived Coordinate Systems

The 'GSE' (Geocentric Solar Ecliptic) coordinate system has its x-axis pointing from the earth towards the sun, its y-axis is in the ecliptic plane pointing towards dusk (*i.e.*, opposing planetary motion), and its z-axis, completing the right-handed triad, is parallel to the ecliptic pole. Relative to an inertial system, this system has a yearly rotation.

To within about 7° (the inclination of the sun's equator to the ecliptic plane), $\hat{\mathbf{X}} \simeq -\hat{\mathbf{R}}$, $\hat{\mathbf{Y}} \simeq -\hat{\mathbf{T}}$ and $\hat{\mathbf{Z}} \simeq \hat{\mathbf{N}}$.

WIND magnetic field data is routinely provided in GSE coordinates, and must be rotated into RTN coordinates in order to compute magnetic helicity. Recall that from section A.5 we need one axis must be aligned with the (radial) flow direction.

B.3 Transformation to Mean-Field Coordinates

We want to rotate vector data from an original coordinate system to a new 'primed' coordinate system through the transformation $\mathbf{A}' = \mathbf{R}\mathbf{A}$, where $\mathbf{R}$ is some rotation matrix.

In chapter 3 the primed coordinates are those of *Belcher and Davis* [1971], namely, $(\hat{\mathbf{B}} \times \hat{\mathbf{R}}, \hat{\mathbf{B}} \times (\hat{\mathbf{B}} \times \hat{\mathbf{R}}), \hat{\mathbf{B}})$. The required rotation matrix may be written as

$$\mathbf{R} = \begin{pmatrix} \hat{\mathbf{e}}_1 \cdot \hat{\mathbf{R}} & \hat{\mathbf{e}}_1 \cdot \hat{\mathbf{T}} & \hat{\mathbf{e}}_1 \cdot \hat{\mathbf{N}} \\ \hat{\mathbf{e}}_2 \cdot \hat{\mathbf{R}} & \hat{\mathbf{e}}_2 \cdot \hat{\mathbf{T}} & \hat{\mathbf{e}}_2 \cdot \hat{\mathbf{N}} \\ \hat{\mathbf{e}}_3 \cdot \hat{\mathbf{R}} & \hat{\mathbf{e}}_3 \cdot \hat{\mathbf{T}} & \hat{\mathbf{e}}_3 \cdot \hat{\mathbf{N}} \end{pmatrix}, \tag{B.1}$$

where the $\hat{\mathbf{e}}$'s are unit vectors in the new coordinate system. The simplest of these to write down is $\hat{\mathbf{e}}_3$, which is simply the unit vector $\hat{\mathbf{B}}$:

$$\hat{\mathbf{e}}_3 = \frac{B_R\hat{\mathbf{R}} + B_T\hat{\mathbf{T}} + B_N\hat{\mathbf{N}}}{\sqrt{B_R^2 + B_T^2 + B_N^2}} \tag{B.2}$$

The other two unit vectors require a little more work:

$$\begin{aligned} \hat{\mathbf{e}}_1 &= \frac{\hat{\mathbf{B}} \times \hat{\mathbf{R}}}{|\hat{\mathbf{B}} \times \hat{\mathbf{R}}|} \\ &= \frac{(B_R\hat{\mathbf{R}} + B_T\hat{\mathbf{T}} + B_N\hat{\mathbf{N}}) \times \hat{\mathbf{R}}}{N_1} \\ &= \frac{B_N\hat{\mathbf{T}} - B_T\hat{\mathbf{N}}}{N_1} \end{aligned}$$

obviously, then, $N_1^2 = B_T^2 + B_N^2$, and so

$$\hat{\mathbf{e}}_1 = \frac{B_N\hat{\mathbf{T}} - B_T\hat{\mathbf{N}}}{\sqrt{B_T^2 + B_N^2}}. \tag{B.3}$$

And for $\hat{\mathbf{B}} \times (\hat{\mathbf{B}} \times \hat{\mathbf{R}})$,

$$\begin{aligned} \hat{\mathbf{e}}_1 &= \frac{\hat{\mathbf{B}} \times (\hat{\mathbf{B}} \times \hat{\mathbf{R}})}{|\hat{\mathbf{B}} \times (\hat{\mathbf{B}} \times \hat{\mathbf{R}})|} \\ &= \frac{(B_R\hat{\mathbf{R}} + B_T\hat{\mathbf{T}} + B_N\hat{\mathbf{N}}) \times (B_N\hat{\mathbf{T}} - B_T\hat{\mathbf{N}})}{N_2} \\ &= \frac{-(B^2 - B_R^2)\hat{\mathbf{R}} + B_RB_T\hat{\mathbf{T}} + B_RB_N\hat{\mathbf{N}}}{N_2} \end{aligned}$$

with

$$\begin{aligned} N_2^2 &= (B^2 - B_R^2)^2 + (B_R B_T)^2 + (B_R B_N)^2 \\ &= (B^2 - B_R^2)^2 + B_R^2(B^2 - B_R^2) \\ &= (B^2 - B_R^2)[(B^2 - B_R^2) + B_R^2] \\ &= B^2(B^2 - B_R^2) \end{aligned}$$

so

$$\hat{\mathbf{e}}_2 = \frac{-(B^2 - B_R^2)\hat{\mathbf{R}} + B_R B_T \hat{\mathbf{T}} + B_R B_N \hat{\mathbf{N}}}{\sqrt{B^2(B^2 - B_R^2)}}. \tag{B.4}$$

Finally, then, the coordinate rotation matrix is

$$\mathsf{R} = \begin{pmatrix} 0 & \frac{B_N}{\sqrt{B_T^2 + B_N^2}} & \frac{-B_T}{\sqrt{B_T^2 + B_N^2}} \\ \frac{-(B^2 - B_R^2)}{\sqrt{B^2(B^2 - B_R^2)}} & \frac{B_R B_T}{\sqrt{B^2(B^2 - B_R^2)}} & \frac{B_R B_N}{\sqrt{B^2(B^2 - B_R^2)}} \\ \frac{B_R}{B} & \frac{B_T}{B} & \frac{B_N}{B} \end{pmatrix}. \tag{B.5}$$

For rotation into the coordinate system of *Bieber et al.* [1996], we let $-\hat{\mathbf{e}}_2 \rightarrow \hat{\mathbf{e}}_1$ and $\hat{\mathbf{e}}_1 \rightarrow \hat{\mathbf{e}}_2$.

Appendix C

WAVE DISPERSION RELATIONS

In this appendix, we provide an explanation of the workings of H. Kit Wong's linearized Maxwell-Vlasov codes used to generate Alfvén wave dispersion relations numerically.

C.1 Application

The codes used to calculate dispersion relations via perturbation analysis of the Vlasov equation are capable of calculating linear instabilities for much more complicated situations than we consider here in calculating Alfvén wave dispersion relations. As such, many of the input options are turned off or set to zero.

There are three contributions α that need to be summed to solve equation (4.31), namely ions, electrons and a third "beam" component of electrons. The "beam" component may be an actual beam drifting through the other two components, or simply a second, electron/ ion population with a different temperature or temperature anisotropy.

The input parameters to the code are as follows:

1. n_p, n_e, n_b. Strictly, the sum over n in equations (4.31) and (4.31) should be from $-\infty$ to ∞. We only consider the range $\pm n_\alpha$, to limit computations. All the calculations used in this work took $n_e = 3$ and $n_p = 10$.

2. ω_b, ω_e. The plasma frequencies (and hence densities) for the electron and beam components, scaled to dimensionless units (by dividing by the cyclotron

frequency). The ion plasma frequency is determined by charge neutrality, $\omega_p^2 = (m_p/m_e)(\omega_e^2 + \omega_b^2)$. We never considered a beam component, and always took $\omega_b = 0$. We chose $\omega_e = 116.69$, a typical value for the solar wind, which gives $\omega_p = 5000$.

3. $\beta_{\parallel,\alpha}$, $\beta_{\perp,\alpha}$. Since we only ever considered a single temperature Maxwellian distribution (equation (4.26)), $\beta_\parallel = \beta_\perp$ for each component.

4. $v_{o,\alpha}$. The components are allowed to drift down the magnetic field at this velocity (scaled to dimensionless units by the Alfvén speed). All drifts are zero.

5. k_{initial}, Δk, N_k. The wavenumber, scaled to dimensionless units by V_A/Ω_p (see page 49). At wavenumbers smaller than $\simeq 0.1$, the frequencies of the Alfvén wave and fast magnetosonic wave are similar, and the root-finding code might start following the wrong branch. Care must be taken to ensure that the code is following the Alfvén branch. k_{initial} was always set at 0.1, and for smaller wavenumbers stepped backwards, keeping all other parameters the same. The two parts of the resulting output were then combined.

6. θ_{kB}, $\Delta\theta$, N_θ. The angle to the mean field at which the wave propagates. The other two parameters are looped over, if present after looping over the N_k wavenumbers. Typically, this is done for N_k small, since for multiple angles, the initial guess of an angle is the last returned frequency for the previous angle.

7. ω_r, γ. An initial guess for the real and imaginary parts of the frequency at $k = k_{\text{initial}}$. This needs to be fairly accurate, so that the root-finding subroutine can follow the intended branch. For the Alfvén mode, $\omega_r \simeq k_\parallel V_A$. Equation (4.31) simplified dramatically for parallel propagation, enabling the imaginary part

of the frequency to be estimated. *Gary* [1993] gives the following formula for the damping rate:

$$\gamma \simeq -\frac{\pi}{2k_\parallel}\sum_\alpha \frac{\omega_\alpha^2}{(2\pi)^{1/2}v_{th,\alpha}}\exp\left[\frac{(\omega_r \pm \Omega_\alpha)^2}{2k_\parallel^2 v_{th,\alpha}^2}\right]. \qquad \text{(C.1)}$$

By taking small steps in θ, initial estimates of γ for oblique propagation may be obtained.

C.2 The plasma dispersion function

The plasma dispersion function $Z(\xi)$ is calculated either by its power series expansion for $|\xi| < 4$, or by its asymptotic expansion.

The power series expansion [*Fried and Conte*, 1961] is

$$\begin{aligned} Z(\xi) &= i\pi^{1/2}e^{-\xi^2} - 2\xi\left[1 - \frac{2\xi^2}{3} + \frac{4\xi^4}{15} - \ldots\right] \\ &= ie^{-\xi^2} - \xi\sum_{n=0}^{\infty}(-\xi^2)^n\frac{\pi^{1/2}}{\left(n+\frac{1}{2}\right)!}. \end{aligned}$$

In practice, we take the upper limit of summation in the codes to be 100.

The asymptotic expansion [*Fried and Conte*, 1961] is

$$\begin{aligned} Z(\xi) &= i\pi^{1/2}\sigma e^{-\xi^2} - \frac{1}{\xi}\left[1 + \frac{1}{2\xi^2} + \frac{3}{4\xi^4} + \ldots\right] \\ &= i\pi^{1/2}\sigma e^{-\xi^2} - \sum_{n=0}^{\infty}\xi^{-(2n+1)}\frac{\left(n-\frac{1}{2}\right)!}{\pi^{1/2}}, \end{aligned}$$

where

$$\sigma = \begin{cases} 0 & \Im\xi > 0 \\ 1 & \Im\xi = 0 \\ 2 & \Im\xi < 0 \end{cases}.$$

Again, in the program, rather than an infinite sum, only the first 25 terms are calculated.

C.3 Bessel Functions

Calculation of the modified Bessel functions $I_n(\lambda)$ is done following the algorithm outlined in *Numerical Recipes* [*Press et al.*, 1992, section 6.6]. The derivatives of $\Lambda_n(\lambda) = I_n(\lambda)e^{-\lambda}$ present in equations (4.32) are obtained by their recursion relation, equation (4.27).

C.4 Root Finding

The calculation of $\omega(k,\theta)$ follows the Muller method of root-finding. It is an extension of the secant method [*Press et al.*, 1992, section 9.1] that uses a parabola to interpolate between guesses rather than a straight line. Solving the zeroes of the quadratic allows the method to find roots in the complex plane, where the roots $\omega = \omega_r + i\gamma$ are.

If $f(\omega) = \det \mathbf{D}(\mathbf{k},\omega)$ is the function we are trying to find roots for (recall that $\mathbf{k} = (k,\theta)$ is fixed), and given three previous guesses for the root ω_{j-2}, ω_{j-1}, ω_j, then the next approximation ω_{j+1} is produced by the following formulae

$$\begin{aligned}
\Delta f_1 &= \frac{f(\omega_{j-1}) - f(\omega_{j-2})}{\omega_{j-1} - \omega_{j-2}} \\
\Delta f_2 &= \frac{f(\omega_j) - f(\omega_{j-1})}{\omega_j - \omega_{j-1}} \\
A &= \frac{\Delta f_2 - \Delta f_1}{\omega_j - \omega_{j-2}} \\
B &= \Delta f_2 - A(\omega_j + \omega_{j-1}) \\
C &= f(\omega_j) - A\omega_j^2 - B\omega_j
\end{aligned} \tag{C.2}$$

followed by

$$\omega_{j+1} = \frac{-2C}{B \pm \sqrt{B^2 - 4AC}} \tag{C.3}$$

where the sign in the denominator is chosen to make the absolute value $|\omega_{j+1} - \omega_j|$ as large as possible. Although the algorithm will converge (albeit slowly) for any

three initial guesses, we take

$$\begin{aligned}
\omega_j &= \omega(k-\Delta k) - (0.01+0.01i)[\omega(k-\Delta k) + (0.001+0.001i)] \\
\omega_{j-1} &= \omega(k-\Delta k) \\
\omega_{j-2} &= \omega(k-\Delta k) + (0.01+0.01i)[\omega(k-\Delta k) - (0.001+0.001i)],
\end{aligned}$$

where $\omega(k-\Delta k)$ is the calculated root for the previous wavenumber k.

Appendix D

REDUCTION OF SPECTRAL TENSORS

D.1 Introduction

It is not at all obvious how equation (3.4.19) of *Batchelor*'s [1970] book *The Theory of Homogeneous Turbulence* follows from the lines of algebra above it.

The purpose of this Appendix is to derive that equation. In doing so, we shall derive equation (eqn:batch3417) of section 5.1.3.3, showing how the reduced and omni-directional spectra may be related.

Batchelor's equation (3.4.19) relates the lateral (perpendicular) and longitudinal (parallel) reduced spectra. He refers to these two quantities as $\Theta_{22}(\kappa_1, 0, 0)$ and $\phi(\kappa_1) \equiv \Theta_{11}(\kappa_1, 0, 0)$ respectively. We shall refer to them as $S^r_{yy}(k_x)$ and $S^r_{xx}(k_x)$ respectively. In the three-dimensional case we shall consider $S^r_{zz}(k_x)$ as well. As in equation (A.16), we take the x direction to be the axis along which the spectra are reduced. In the heliosphere, of course, this corresponds to the direction of solar wind flow, which is effectively the radial direction $\hat{\mathbf{R}}$.

The full energy spectrum is denoted by $E(\mathbf{k})$, and it may be viewed as a single scalar function defining $\mathbf{S}^r$.

D.2 Two-Dimensional Turbulence

First, let us consider only two-dimensional turbulence, with only one independent coordinate perpendicular to the direction in which the spectra are reduced. In this instance, the spectral tensor has the following form and properties:

$$
\begin{aligned}
S_{ij}(\mathbf{k}) &= \left(\delta_{ij} - \frac{k_i k_j}{k^2}\right) E(\mathbf{k}) \\
\text{Trace } S_{ij} &= S_{ii} = E(\mathbf{k}),
\end{aligned}
$$

since $\delta_{ii} = 2$ in two dimensions. The two reduced spectra are

$$
\begin{aligned}
S^r_{xx}(k_x) &= \int_{-\infty}^{\infty} dk_y \left(1 - \frac{k_x^2}{k^2}\right) E(\mathbf{k}) \\
S^r_{yy}(k_x) &= \int_{-\infty}^{\infty} dk_y \left(1 - \frac{k_y^2}{k^2}\right) E(\mathbf{k}) \\
&= \int_{-\infty}^{\infty} dk_y \left(\frac{k_x^2}{k^2}\right) E(\mathbf{k}),
\end{aligned}
$$

since $k^2 = k_x^2 + k_y^2$. Now let $w = \sqrt{k_x^2 + k_y^2}$, so that $k_y = \sqrt{w^2 - k_x^2}$, $dk_y = w dw/\sqrt{w^2 - k_x^2}$, and it is assumed that $E(w)$ has the same dimensions as $E(\mathbf{k})$, *i.e.*, $E(\mathbf{k})$ depends on $|\mathbf{k}|$.

Therefore,

$$
\begin{aligned}
S^r_{yy}(k_x) &= k_x^2 \int_{k_x}^{\infty} \frac{w dw}{\sqrt{w^2 - k_x^2}} \frac{E(w)}{w^2} \\
&= k_x^2 \int_{k_x}^{\infty} \frac{dw}{\sqrt{w^2 - k_x^2}} \frac{E(w)}{w}.
\end{aligned}
$$

Now consider

$$
\begin{aligned}
S^r_{xx}(k_x) &= \int_{-\infty}^{\infty} dk_y \frac{k^2 - k_x^2}{k^2} E(\mathbf{k}) \\
&= \int_{k_x}^{\infty} \frac{w dw}{\sqrt{w^2 - k_x^2}} (w^2 - k_x^2) \frac{E(w)}{w^2} \\
&= \int_{k_x}^{\infty} dw \frac{(w^2 - k_x^2)^{1/2}}{w} E(w)
\end{aligned}
$$

and

$$\begin{aligned}\frac{d}{dk_x}S^r_{xx}(k_x) &= -\frac{(w^2-k_x^2)^{1/2}}{w}E(w)\Big|_{w=k_x} \\ &\quad + \frac{(w^2-k_x^2)^{1/2}}{w}E(w)\Big|_{w=\infty} \\ &\quad + \int_{k_x}^{\infty} dw \frac{\partial}{\partial k_x}\frac{(w^2-k_x^2)^{1/2}}{w}E(w).\end{aligned}$$

The first two terms are zero, so that

$$\frac{d}{dk_x}S^r_{xx}(k_x) = -k_x \int_{k_x}^{\infty} \frac{dw}{\sqrt{w^2-k_x^2}}\frac{E(w)}{w}$$

and, by inspection,

$$S^r_{yy}(k_x) = -k_x \frac{d}{dk_x}S^r_{xx}(k_x). \tag{D.1}$$

D.3 Three-Dimensional Turbulence

In this instance,

$$S_{ij}(\mathbf{k}) = \left(\delta_{ij} - \frac{k_i k_j}{k^2}\right)\frac{E(\mathbf{k})}{2},$$

where the factor of 2 in the denominator again ensures $S_{ii}(\mathbf{k}) = E(\mathbf{k})$.

The parallel component is

$$S^r_{xx}(k_x) = \int dk_y dk_z \left(1 - \frac{k_x^2}{k^2}\right)\frac{E(\mathbf{k})}{2},$$

and the two perpendicular spectra are

$$\begin{aligned}S^r_{yy}(k_x) &= \int dk_y dk_z \left(1 - \frac{k_y^2}{k^2}\right)\frac{E(\mathbf{k})}{2}, \\ S^r_{zz}(k_x) &= \int dk_y dk_z \left(1 - \frac{k_z^2}{k^2}\right)\frac{E(\mathbf{k})}{2}.\end{aligned}$$

$S^r_{yy}(k_x) = S^r_{zz}(k_x)$ since $E(\mathbf{k})$ depends only on k.

Adding S_{yy} and S_{zz} gives

$$\begin{aligned}2S^r_{yy}(k_x) &= \int dk_y dk_z \left(1 + 1 - \frac{k_y^2 + k_z^2}{k^2}\right)\frac{E(\mathbf{k})}{2} \\ &= \int dk_y dk_z \left(1 + \frac{k_x^2}{k^2}\right)\frac{E(\mathbf{k})}{2}.\end{aligned}$$

Thus,

$$2S^r_{yy} - S^r_{xx} = 2\int dk_y dk_z \frac{k_x^2}{k^2}\frac{E(\mathbf{k})}{2}. \tag{D.2}$$

Now consider the integral on the RHS of equation D.2 in cylindrical polar coordinates. Let $w = \sqrt{k_\perp^2 + k_x^2}$, so that $w\,dw = k_\perp\,dk_\perp$ and, as before, $E(w)$ has the same dimensions as $E(\mathbf{k})$. So,

$$\begin{aligned} k_x^2 \int dk_y dk_z \frac{E(\mathbf{k})}{k^2} &= 2\pi k_x^2 \int \frac{k_\perp\,dk_\perp}{k_\perp^2 + k_x^2} \\ &= 2\pi k_x^2 \int_{k_x}^{\infty} w\,dw \frac{E(w)}{w^2}. \end{aligned} \tag{D.3}$$

Now notice that

$$\begin{aligned} S^r_{xx}(k_x) &= 2\pi \int \frac{dk_\perp^2}{2}\frac{k_\perp^2}{k_\perp^2 + k_x^2}E(\mathbf{k}) \\ &= 2\pi \int_{k_x}^{\infty} w\,dw \frac{w^2 - k_x^2}{w^2}E(w) \\ \frac{d}{dk_x}S^r_{xx}(k_x) &= -2\pi k_x \int_{k_x}^{\infty} \frac{dw}{w}E(w), \end{aligned}$$

since

$$\left.\frac{w^2 - k_x^2}{w^2}E(w)\right|_{w=k_x} \equiv 0.$$

So,

$$k_x \frac{d}{dk_x}S^r_{xx}(k_x) = -2\pi k_x^2 \int_{k_x}^{\infty} \frac{dw}{w}E(w)$$

(compare with equation (D.3), above).

Therefore,

$$2S^r_{yy}(k_x) - S^r_{xx}(k_x) = -k_x \frac{d}{dk_x}S^r_{xx}(k_x)$$

or

$$S^r_{yy}(k_x) = \frac{1}{2}\left(S^r_{xx}(k_x) - k_x \frac{d}{dk_x}S^r_{xx}(k_x)\right). \tag{D.4}$$

This is, in our notation, Batchelor's equation (3.4.19).

D.3.1 Trace

Note that the sum of the three components is

$$\begin{aligned} S^r_{xx} + 2S^r_{yy} = \mathcal{S}^r(k_x) &= 2\int dk_y dk_z E(\mathbf{k}) \\ &= 2 \cdot 2\pi \int k_\perp dk_\perp E(\mathbf{k}) \\ &= 2 \cdot 2\pi \int_{k_x}^{\infty} dw\, w E(\mathbf{k}), \end{aligned}$$

where we have again used $w\,dw = k_\perp\, dk_\perp$. However, $E^{omni} \equiv \mathcal{E}(k) = 4\pi k^2 E(\mathbf{k})$, so

$$\mathcal{S}^r(k_x) = \int_{k_x}^{\infty} dw \frac{\mathcal{E}(w)}{w}. \tag{D.5}$$

Equation (D.5) is equation (5.7), albeit in a slightly different notation.

Expressed in a differential, rather than integral form, and since omnidirectional turbulence is isotropic, equation (D.5) becomes

$$\frac{d}{dk_x}\mathcal{S}^r(k_x) = -\frac{1}{k_x}\mathcal{E}(k_x),$$

or

$$\mathcal{E}(k) = -k\frac{d}{dk}\mathcal{S}^r_{trace}(k). \tag{D.6}$$

D.3.2 Check

Finally, as Batchelor says, the explicit expression for $\mathcal{E}(k)$ in terms of the measurable function $S_{xx}(k)$ (his equation (3.4.18)) is

$$\begin{aligned} \mathcal{E}(k) &= k^3 \frac{d}{dk}\left[\frac{1}{k}\frac{dS_{xx}}{dk}\right] \\ &= k^3\left[-\frac{1}{k^2}\frac{dS_{xx}}{dk} + \frac{1}{k}\frac{d^2S_{xx}}{dk^2}\right] \\ &= -k\frac{dS_{xx}}{dk} + k^2\frac{d^2S_{xx}}{dk^2}. \end{aligned}$$

As a check, our results, equations (D.6) and (D.4) give

$$\begin{aligned}
\mathcal{E}(k) &= -k\frac{d}{dk}\mathcal{S}_{trace} \\
&= -k\frac{d}{dk}\left[S_{xx} + 2S_{yy}\right] \\
&= -k\frac{d}{dk}\left[2S_{xx} - -k\frac{d}{dk}S_{xx}\right] \\
&= -k\left[2\frac{dS_{xx}}{dk} - \frac{dS_{xx}}{dk} - k\frac{d^2S_{xx}}{dk^2}\right] \\
&= -k\frac{dS_{xx}}{dk} + k^2\frac{d^2S_{xx}}{dk^2}. \\
&\quad \surd
\end{aligned}$$

Bibliography

Ambrosiano, J., W. H. Matthaeus, M. L. Goldstein, and D. Plante, Test particle acceleration in turbulent reconnecting magnetic fields, *J. Geophys. Res.*, **93**, 14 383, 1988.

Barnes, A., Collisionless damping of hydromagnetic waves, *Phys. Fluids*, **9**, 1483, 1966.

Barnes, A., Hydromagnetic waves and turbulence in the solar wind, in *Solar System Plasma Physics, vol. I*, edited by E. N. Parker, C. F. Kennel, and L. J. Lanzerotti, p. 251. North-Holland, Amsterdam, 1979.

Batchelor, G. K., *The Theory of Homogeneous Turbulence*. Cambridge University Press, Cambridge, 1970.

Behannon, K. W., Observations of the interplanetary magnetic field between 0.46 and 1 AU by the Mariner 10 spacecraft, Ph.D. thesis, Catholic Univ. of Am., Washington, DC, 1975.

Belcher, J. W., and R. Burchsted, Energy densities of Alfvén waves between 0.7 and 1.6 AU, *J. Geophys. Res.*, **79**, 4765, 1974.

Belcher, J. W., and L. Davis, Jr., Large-amplitude Alfvén waves in the interplanetary medium, 2, *J. Geophys. Res.*, **76**, 3534, 1971.

Bevington, P. R., *Data Reduction and Error Analysis for the Physical Sciences*. McGraw-Hill, New York, 1969.

Bieber, J. W., C. W. Smith, and W. H. Matthaeus, Cosmic ray pitch-angle scattering in isotropic turbulence, *Astrophys. J.*, **334**, 470, 1988.

Bieber, J. W., J. Chen, W. H. Matthaeus, C. W. Smith, and M. A. Pomerantz, Long-term variations of interplanetary magnetic field spectra with implications for cosmic ray modulation, *J. Geophys. Res.*, **98**, 3585, 1993a.

Bieber, J. W., W. H. Matthaeus, C. W. Smith, W. Wanner, M. Kallenrode, and G. Wibberenz, Proton and electron mean free paths: The Palmer consensus revisited, *Astrophys. J.*, **420**, 294, 1994.

Bieber, J. W., W. Wanner, and W. H. Matthaeus, Dominant two-dimensional solar wind turbulence with implications for cosmic ray transport, *J. Geophys. Res.*, **101**, 2511, 1996.

Biermann, L., Kometschwerfe und solar Korpuskularstrahlung, *Z. Astrophys.*, **29**, 274, 1951.

Blackman, R. B., and J. W. Tukey, *The Measurement of Power Spectra*. Dover, Mineola, New York, 1958.

Bonetti, A., H. S. Bridge, A. J. Lazarus, B. Rossi, and F. Scherb, Explorer X plasma measurements, *J. Geophys. Res.*, **68**, 4017, 1963.

Born, M., and E. Wolf, *Principles of Optics*. Pergamon, New York, 4th edn., 1970.

Bridge, H. S., C. Dilworth, A. J. Lazarus, E. F. Lyon, B. Rossi, and F. Scherb, *J. Phys. Soc. Japan*, **17**, Suppl. A–II, 1961.

Brillouin, L., La mécanique ondulatoire de Schrödinger; une méthode générale de résolution par approximations successives, *Comptes Rendus*, **183**, 24, 1926.

Burlaga, L. F., et al., A magnetic cloud containing prominence material: January 1997, *J. Geophys. Res.*, **103**, 277, 1998.

Burlaga, L. F., E. C. Sittler, F. Mariani, and R. Schwenn, Magnetic loop behind an interplanetary shock: Voyager, Helios and IMP8 observations, *J. Geophys. Res.*, **86**, 6673, 1981.

Canton, J., An attempt to account for the regular diurnal variation of the horizontal magnetic needle; and also for its irregular variation at the time of an Aurora Borealis, *Phil. Trans. Roy. Soc. Lond.*, **51**, 398, 1759.

Carrington, R. C., Description of a singular appearance seen in the Sun on September 1, 1859, *Mon. Not. R. Astr. Soc.*, **20**, 13, 1859.

Chamberlain, J. W., Interplanetary gas. II. Expansion of a model corona, *Astrophys. J.*, **131**, 47, 1960.

Chamberlain, J. W., Interplanetary gas. III. A hydrodynamical model of the corona, *Astrophys. J.*, **133**, 675, 1961.

Chen, F. F., *Introduction to Plasma Physics*. Plenum, New York, 2nd edn., 1984.

Chen, J., Long-term modulation of cosmic rays in interplanetary magnetic turbulence, Ph.D. thesis, University of Delaware, Newark, 1989.

Chen, J., J. W. Bieber, and M. A. Pomerantz, Cosmic ray unidirectional latitude gradient: Evidence for north-south asymmetric solar modulation, *J. Geophys. Res.*, **96**, 11 569, 1991.

Coleman, P. J., Hydromagnetic waves in the interplanetary plasma, *Phys. Rev. Lett.*, **17**, 207, 1966.

Coleman, P. J., Turbulence, viscosity, and dissipation in the solar wind plasma, *Astrophys. J.*, **153**, 371, 1968.

Cranmer, S. R., G. B. Field, and J. L. Kohl, Models of ion cyclotron resonant heating, *Astrophys. J.*, **518**, 937, 1999.

Daily, W. D., Alfvén wave refraction by interplanetary inhomogeneities, *J. Geophys. Res.*, **78**, 2043, 1973.

de Mairan, J. J. d'Or, *Suite de Mémoires*. Académie Royale des Sciences, Paris, 2nd edn., 1754.

Denskat, K. U., H. J. Beinroth, and F. M. Neubauer, Interplanetary magnetic-field power spectra with frequencies from 2.4×10^{-5} Hz to 470 Hz from Helios-observations during solar minimum conditions, *Journal of Geophysics-Zeitschrift für Geophysik*, **54**, 60, 1983.

Dobrowolny, M., A. Mangeney, and P. Veltri, Fully developed anisotropic hydromagnetic turbulence in interplanetary space, *Phys. Rev. Lett.*, **45**, 144, 1980b.

Elsässer, W. M., The hydromagnetic equations, *Phys. Rev.*, **79**, 183, 1950.

Foukal, P., *Solar Astrophysics*. Wiley Interscience, New York, 1990.

Freeman, J., Estimates of solar wind heating inside 0.3 AU, *Geophys. Rev. Lett.*, **15**, 88, 1988.

Fried, B. D., and S. D. Conte, *The plasma dispersion function*. Academic Press, New York, 1961.

Gary, S. P., *Theory of space plasma microinstabilities*. Cambridge Univ. Press, New York, 1993.

Gary, S. P., Collisionless dissipation wavenumber: Linear theory, *J. Geophys. Res.*, **104**, 6759, 1999.

Gazis, P. R., and A. J. Lazarus, Voyager observations of solar wind proton temperature: 1–10 AU, *Geophys. Rev. Lett.*, **9**, 431, 1982.

Ghosh, S., W. H. Matthaeus, D. A. Roberts, and M. L. Goldstein, The evolution of slab fluctuations in the presence of pressure balanced structures and velocity shears, *J. Geophys. Res.*, **103**, 23 691, 1998a.

Gold, T., *Gas Dynamics of Cosmic Clouds*. North-Holland, Amsterdam, 1955.

Goldstein, M. L., H. K. Wong, and C. W. Smith, Large amplitude MHD waves upstream of the Jovian bowshock: Reinterpretation, *J. Geophys. Res.*, **90**, 302, 1985.

Goldstein, M. L., D. A. Roberts, and C. A. Fitch, Properties of the fluctuating magnetic helicity in the inertial and dissipation ranges of solar wind turbulence, *J. Geophys. Res.*, **99**, 11 519, 1994.

Goldstein, M. L., D. A. Roberts, and W. H. Matthaeus, Magnetohydrodynamic turbulence in the solar wind, *Ann. Rev. Astron. Astrophys.*, **33**, 283, 1995.

Grappin, R., U. Frisch, J. Léorat, and A. Pouquet, Alfvénic fluctuations as asymptotic states of MHD turbulence, *Astron. Astrophys.*, **105**, 6, 1982.

Grappin, R., A. Pouquet, and J. Léorat, Dependence of MHD turbulence spectra on the velocity field-magnetic field correlation, *Astron. Astrophys.*, **126**, 51, 1983.

Gray, P., and W. H. Matthaeus, MHD turbulence, reconnection, and test-particle acceleration, in *Particle Acceleration in Cosmic Plasmas*, edited by G. P. Zank, and T. K. Gaisser, p. 261. AIP, New York, AIP Conference Proceedings 264, 1992.

Gringauz, K. I., V. V. Bezruvkikh, V. D. Ozerov, and R. E. Rybchinskii, A study of the interplanetary ionized gas, high-energy electrons and corpuscular radiation from the sun by means of the 3-electrode trap for charged particles on the second Soviet cosmic rocket, *Soviet Phys. Doklady (translation)*, **5**, 361, 1960.

Hasegawa, A., Particle acceleration by MHD surface waves and formation of aurora, *J. Geophys. Res.*, **81**, 5083, 1976.

Hasegawa, A., and T. Sato, *Space Plasma Physics 1. Stationary Processes*. Springer-Verlag, New York, 1989.

Hasegawa, A., and C. Uberoi, The Alfvén wave, Tech. Rep. DOE/TIC No. 11197, Tech. Information Center, U.S. Dept. of Energy, Washington, DC, 1982.

Hollweg, J. V., Transverse Alfvén waves in the solar wind: Arbitrary $\mathbf{k}$, $\mathbf{v}_0$, $\mathbf{b}_0$ and $\delta\mathbf{b}$, *J. Geophys. Res.*, **79**, 1539, 1974.

Hollweg, J. V., On WKB expansions for Alfvén waves in the solar wind, *J. Geophys. Res.*, **95**, 14 873, 1990.

Hollweg, J. V., The Kinetic Alfvén wave revisited, *J. Geophys. Res.*, **104**, 14 811, 1999.

Jackson, J. D., *Classical Electrodynamics*. Wiley, New York, 2nd edn., 1975.

Jeffreys, H., On certain approximate solutions of linear differential equations of the 2nd order, *Proc. London Math. Soc.*, **23**, 428, 1923.

Jokipii, J. R., Cosmic-ray propagation. I. Charged particles in a random magnetic field, *Astrophys. J.*, **146**, 480, 1966.

Kennel, C. F., J. P. Edmiston, and T. Hada, A quarter-century of collisionless shock research, in *Collisionless shocks in the heliosphere: A tutorial review*, edited by R. G. Stone, and B. T. Tsurutani, no. **34** in Geophysical Monographs. American Geophysical Union, Washington, DC, 1985.

Khabibrakhmanov, I. K., and D. J. Mullan, Gravitational damping of Alfvén waves: Theory and numerical modelling, in *Solar Wind Nine*, edited by S. R. Habbal, R. Esser, J. V. Hollweg, and P. A. Isenberg, p. 349. AIP, New York, 1999.

Kinney, R., and J. C. McWilliams, Magnetohydrodynamic equations under anisotropic conditions, *J. Plasma Phys.*, **57**, 73, 1997.

Klein, L. W., D. A. Roberts, and M. L. Goldstein, Anisotropy and minimum variance directions of solar wind fluctuations in the outer heliosphere, *J. Geophys. Res.*, **96**, 3779, 1991.

Kolmogoroff, A. N., Local structure of turbulence in an incompressible viscous fluid at very high Reynolds numbers, *C.R. Acad. Sci. U.R.S.S.*, **30**, 301, 1941a.

Kraichnan, R. H., Inertial-range spectrum of hydromagnetic turbulence, *Phys. Fluids*, **8**, 1385, 1965.

Kraichnan, R. H., and D. C. Montgomery, Two-dimensional turbulence, *Rept. Prog. Phys.*, **43**, 547, 1980.

Kremers, H. A., Wellenmechanik und halbzahlige Quantisierung, *Z. Physik*, **39**, 828, 1926.

Leamon, R. J., C. W. Smith, N. F. Ness, W. H. Matthaeus, and H. K. Wong, Observational constraints on the dynamics of the interplanetary magnetic field dissipation range, *J. Geophys. Res.*, **103**, 4775, 1998a.

Leamon, R. J., W. H. Matthaeus, C. W. Smith, and H. K. Wong, Contribution of cyclotron-resonant damping to kinetic dissipation of interplanetary turbulence, *Astrophys. J.*, **507**, L181, 1998b.

Leamon, R. J., C. W. Smith, and N. F. Ness, Characteristics of magnetic fluctuations within coronal mass ejections: The January 1997 event, *Geophys. Rev. Lett.*, **25**, 2505, 1998c.

Leamon, R. J., C. W. Smith, N. F. Ness, and H. K. Wong, Dissipation range dynamics: Kinetic Alfvén waves and the importance of β_e, *J. Geophys. Res.*, **104**, 22 331, 1999a.

Leamon, R. J., W. H. Matthaeus, C. W. Smith, and H. K. Wong, Considerations limiting cyclotron-resonant damping of cascading interplanetary turbulence and why the 'slab' approximation fails, in *Solar Wind Nine*, edited by S. R. Habbal, R. Esser, J. V. Hollweg, and P. A. Isenberg, p. 465. AIP, New York, 1999b.

Leamon, R. J., N. F. Ness, C. W. Smith, and H. K. Wong, Dynamics of the dissipation range for solar wind magnetic fluctuations, in *Solar Wind Nine*, edited by S. R. Habbal, R. Esser, J. V. Hollweg, and P. A. Isenberg, p. 469. AIP, New York, 1999c.

Lepping, R. P., et al., The WIND magnetic field investigation, *Space Sci. Rev.*, **71**, 207, 1995.

Lotova, N. A., The solar wind transsonic region, *Solar Phys.*, **117**, 399, 1988.

Lysak, R. L., and W. Lotko, On the kinetic dispersion relation for shear Alfvén waves, *J. Geophys. Res.*, **101**, 5085, 1996.

Mackin, R. J., and M. Neubegauer (eds.), *The Solar Wind*. Pergamon, New York, 1966.

Marsch, E., MHD turbulence in the solar wind, in *Physics of the Inner Heliosphere, vol. 2*, edited by R. Schwenn, and E. Marsch, p. 159. Springer-Verlag, New York, 1991.

Marsch, E., and A. Mangeney, Ideal MHD equations in terms of compressive Elsässer variables, *J. Geophys. Res.*, **92**, 7363, 1987.

Matthaeus, W. H., and M. L. Goldstein, Measurement of the rugged invariants of magnetohydrodynamic turbulence in the solar wind, *J. Geophys. Res.*, **87**, 6011, 1982a.

Matthaeus, W. H., and M. L. Goldstein, Low-frequency $1/f$ noise in the interplanetary magnetic field, *Phys. Rev. Lett.*, **57**, 495, 1986.

Matthaeus, W. H., and S. L. Lamkin, Turbulent magnetic reconnection, *Phys. Fluids*, **29**, 2513, 1986.

Matthaeus, W. H., and D. Montgomery, Selective decay hypothesis at high mechanical and magnetic Reynolds numbers, *Annals of the New York Academy of Sciences*, **357**, 203, 1980.

Matthaeus, W. H., and Y. Zhou, Extended inertial range phenomenology of magnetohydrodynamic turbulence, *Phys. Fluids B*, **1**, 1929, 1989.

Matthaeus, W. H., M. L. Goldstein, and C. W. Smith, Evaluation of magnetic helicity in homogeneous turbulence, *Phys. Rev. Lett.*, **48**, 1256, 1982.

Matthaeus, W. H., M. L. Goldstein, and D. A. Roberts, Evidence for the presence of quasi-two-dimensional nearly incompressible fluctuations in the solar wind, *J. Geophys. Res.*, **95**, 20 673, 1990.

Matthaeus, W. H., J. W. Bieber, and G. P. Zank, Unquiet on any front: Anisotropic turbulence in the solar wind, *Rev. Geophys. Supp.*, **33**, 609, 1995b.

Matthaeus, W. H., G. P. Zank, and S. Oughton, Coronal heating by quasi-2D MHD turbulence driven by non-WKB wave reflection, in *Solar Wind Nine*, edited by S. R. Habbal, R. Esser, J. V. Hollweg, and P. A. Isenberg, p. 361. AIP, New York, 1999a.

Matthaeus, W. H., G. P. Zank, C. W. Smith, and S. Oughton, Turbulence, spatial transport, and heating of the solar wind, *Phys. Rev. Lett.*, **82**, 3444, 1999b.

Moffatt, H. K., *Magnetic Field Generation in Electrically Conducting Fluids*. Cambridge University Press, New York, 1978.

Montgomery, D. C., Major disruption, inverse cascades, and the Strauss equations, *Physica Scripta*, **T2/1**, 83, 1982.

Montgomery, D. C., and D. A. Tidman, *Plasma Kinetic Theory*. McGraw-Hill, New York, 1964.

Montgomery, D. C., M. R. Brown, and W. H. Matthaeus, Density fluctuation spectra in MHD turbulence, *J. Geophys. Res.*, **92**, 282, 1987.

Ness, N. F., and J. M. Wilcox, Sector structure of the quiet interplanetary magnetic field, *Science*, **48**, 1592, 1965.

Ogilvie, K. W., et al., SWE, a comprehensive plasma instrument for the WIND spacecraft, *Space Sci. Rev.*, **71**, 55, 1995.

Oughton, S., Transport of solar wind fluctuations: A turbulence approach, Ph.D. thesis, University of Delaware, Newark, Delaware, 19716, 1993.

Palmer, I. D., Transport coefficients of low-energy cosmic rays in interplanetary space, *Rev. Geophys. Space Phys.*, **20**, 335, 1982.

Panchev, S., *Random fluctuations and turbulence*. Pergamon, New York, 1971.

Parker, E. N., Dynamics of the interplanetary gas and magnetic fields, *Astrophys. J.*, **123**, 644, 1958.

Parker, E. N., *Interplanetary Dynamical Processes*. Wiley-Interscience, New York, 1963.

Parker, E. N., Space physics before the space age, in *Solar Wind Nine*, edited by S. R. Habbal, R. Esser, J. V. Hollweg, and P. A. Isenberg, p. 3. AIP, New York, 1999.

Phillips, J. L., et al., Ulysses solar wind plasma observations from pole to pole, *Geophys. Rev. Lett.*, **22**, 3301, 1995.

Press, W. H., S. A. Teukolsky, W. T. Vetterling, and B. P. Flannery, *Numerical Recipes in FORTRAN 77*. Cambridge Univ. Press, New York, 2nd edn., 1992.

Richardson, J. D., K. I. Paularena, A. J. Lazarus, and J. W. Belcher, Radial evolution of the solar wind from IMP 8 to Voyager 2, *Geophys. Rev. Lett.*, **22**, 325, 1995.

Richter, A. K., K. C. Hsieh, A. H. Luttrell, E. Marsch, and R. Schwenn, Review of interplanetary shock phenomena near and within 1 AU, in *Collisionless shocks in the heliosphere: Reviews of modern research*, edited by B. T. Tsurutani, and R. G. Stone, no. **35** in Geophysical Monographs. American Geophysical Union, Washington, DC, 1985.

Roberts, D. A., L. W. Klein, M. L. Goldstein, and W. H. Matthaeus, The nature and evolution of magnetohydrodynamic fluctuations in the solar wind: Voyager observations, *J. Geophys. Res.*, **92**, 11 021, 1987a.

Roberts, D. A., M. L. Goldstein, L. W. Klein, and W. H. Matthaeus, Origin and evolution of fluctuations in the solar wind: Helios observations and Helios-Voyager comparisons, *J. Geophys. Res.*, **92**, 12 023, 1987b.

Roberts, D. A., M. L. Goldstein, and L. W. Klein, The amplitudes of interplanetary fluctuations: Stream structure, heliocentric distance, and frequency dependence, *J. Geophys. Res.*, **95**, 4203, 1990.

Sari, J. W., and G. C. Valley, Interplanetary magnetic field power spectra: Mean field radial or perpendicular to radial, *J. Geophys. Res.*, **81**, 5489, 1976.

Schwartz, S. J., W. C. Feldman, and S. P. Gary, The source of proton anisotropy in the high-speed solar wind, *J. Geophys. Res.*, **86**, 541, 1981.

Shebalin, J. V., W. H. Matthaeus, and D. Montgomery, Anisotropy in MHD turbulence due to a mean magnetic field, *J. Plasma Phys.*, **29**, 525, 1983.

Smith, C. W., and J. W. Bieber, Solar cycle variation of the interplanetary magnetic field spiral, *Astrophys. J.*, **370**, 435, 1991.

Smith, C. W., M. L. Goldstein, and W. H. Matthaeus, Turbulence analysis of the Jovian upstream 'wave' phenomenon, *J. Geophys. Res.*, **88**, 5581, 1983.

Smith, C. W., M. L. Goldstein, W. H. Matthaeus, and A. F. Viñas, Correction to "Turbulence analysis of the Jovian upstream 'wave' phenomenon", *J. Geophys. Res.*, **89**, 9159, 1984.

Smith, C. W., J. W. Bieber, and W. H. Matthaeus, Cosmic ray pitch-angle scattering in isotropic turbulence. II. Sensitive dependence on the dissipation range spectrum, *Astrophys. J.*, **363**, 283, 1990.

Smith, C. W., W. H. Matthaeus, and N. F. Ness, Measurement of the dissipation range spectrum of magnetic fluctuations in the solar wind with applications to the diffusion of cosmic rays, *Proc. 21st Internat. Cosmic Ray Conf. (Adelaide)*, **5**, 280, 1990b.

Snyder, C. W., and M. Neugebauer, Interplanetary solar wind measurements by Mariner 2, *Space. Res.*, **4**, 89, 1964.

Stix, T. H., *Waves in Plasmas*. AIP, College Park, MD, 1992.

Svalgaard, L., Interplanetary magnetic sector structure, 1926–1971, *J. Geophys. Res.*, **77**, 4027, 1972.

Swanson, D. G., *Plasma Waves*. Academic Press, Boston, 1989.

Taylor, G. I., The spectrum of turbulence, *Proc. Roy. Soc. Lond. A*, **164**, 476, 1938.

Tu, C.-Y., The damping of interplanetary Alfvenic fluctuations and the heating of the solar wind, *J. Geophys. Res.*, **93**, 7, 1988.

Tu, C.-Y., and E. Marsch, A model of solar wind fluctuations with two components: Alfvén waves and convective structures, *J. Geophys. Res.*, **98**, 1257, 1993.

Tu, C.-Y., and E. Marsch, MHD structures, waves and turbulence in the solar wind, *Space Sci. Rev.*, **73**, 1, 1995.

Wentzel, G., Eine Verallgemeinerung der Quantenbedingungen für die Zwecke der Wellenmechanik, *Z. Physik*, **38**, 518, 1926.

Wilcox, J. M., and N. F. Ness, Quasi-stationary corotating structure in the interplanetary medium, *J. Geophys. Res.*, **70**, 5793, 1965.

Williams, L. L., G. P. Zank, and W. H. Matthaeus, Dissipation of pickup-induced waves: A solar wind temperature increase in the outer heliosphere?, *J. Geophys. Res.*, **100**, 17 059, 1995.

Wong, H. K., A. F. Viñas, and A. J. Klimas, Generation of high and low frequency waves by long-wavelength electric field fluctuations, *Eos, Trans. AGU*, **78(17)**, *Spring Meet. Suppl.*, S251, 1997.

Zank, G. P., Interaction of the solar wind with the local interstellar medium: A theoretical perspective, *Space Sci. Rev.*, **89(3–4)**, 413, 1999.

Zank, G. P., and W. H. Matthaeus, The equations of reduced magnetohydrodynamics, *J. Plasma Phys.*, **48**, 85, 1992a.

Zank, G. P., and W. H. Matthaeus, Waves and turbulence in the solar wind, *J. Geophys. Res.*, **97**, 17 189, 1992b.

Zank, G. P., and W. H. Matthaeus, Nearly incompressible fluids. II: Magnetohydrodynamics, turbulence, and waves, *Phys. Fluids A*, **5**, 257, 1993.

Zank, G. P., W. H. Matthaeus, and C. W. Smith, Evolution of turbulent magnetic fluctuation power with heliocentric distance, *J. Geophys. Res.*, **101**, 17 093, 1996.